Geosciences and engineering : a publication of the University of Miskolc

7. évf. 10. sz. / 2019

Antrekowitsch, Jürgen - Steinlechner, Stefan - Hanke, Gustav Efficient utilization of zinc, lead, copper by-products	5–13
Hegedűs B. - Kékesi Tamás Purification of aluminium salt slag by leaching with acid or alkali solutions for alternative utilization	14–27
Korniejenko, K. - Miklula, J. - Lach, M. - Moure Alassio, F. - Moreira Garmendia, L. - Duarte Guigou, M. Geopolymer composites reinforced with plastic wastes	28–38
Jáger, D. - Kupka, D. - Václavíková, M. - Gallios, G. Electrochemical oxidation of reactive black 5 azo dye in chloride media	39–47
Mandryk, Oleg - Arkhypova, Liudmyla - Pobigun, Olena - Latsyk, Nataliia Opportunities and limitations of solar energy projects for territorial communities of the Carpathian region of Ukraine	48–59
Csák Csilla - Marinkás György The legal categorization of fly ash in EU and the Hungarian law - analysis of related CJEU case-law	60–73
Mütze, T. - Peuker, U. A. High-performance geopolymers by wet milling of blast furnace slags	74–82
Romenda Roland Róbert Theorethical models for airflow separators to process municipial solid wastes	83–93
Juhász Eleonóra - Munkácsi Adrienn - Lénárt László - Papp Ágnes - Kiss-Tóth Emőke - Lukács Andrea Medical assessment of patients for cave therapy in Lillafüred in the Bükk mountains	94–104
Nagy Zsolt - Baracza Mátyás Krisztián - Szabó Norbert Péter Pore pressure prediction in Pannonian hydrocarbon reservoir systems using an integrated interpretation approach	105–115
Lengyel Tamás - Jobbik Anita Combined analysis system for proppant selection in aspect of fracture conductivity	116–135
Lanzerstorfer, C. Size dependence of the composition of cement kiln dust	136–143
Kolencsik Tóth Andrea Differences between steady-state and transient simulations of mass transport in a river-influenced shallow aquifer	144–157
Romenda Roland Róbert - Burinda Zsófia Behaviour of regular-shape single particles while falling in normal air conditions	158–168

Geosciences and Engineering, Vol. 7, No. 10 (2019), pp. 5–13.

EFFICIENT UTILIZATION OF ZINC, LEAD, AND COPPER CONTAINING BY-PRODUCTS

JÜRGEN ANTREKOWITSCH – STEFAN STEINLECHNER – GUSTAV HANKE

Chair of Nonferrous Metallurgy, Montanuniversität Leoben, Austria

Abstract: The importance of metal by-products and residues for the sake of metal supply is discussed. Some of the residues are already recycled, however, the worldwide recycling rates are still below 50% because of a lack of optimized processes, as well as missing information and data about the materials. The assessment of metal-bearing by-products and economic considerations are of high importance to allow an efficient utilization of these secondary resources in future.

Keywords: *metal by-products and residues, optimized technology, assessment of metal-bearing by-products*

1. PRIMARY AND SECONDARY RAW MATERIALS

Investigating the development of primary metal resources nowadays, a tendency becomes obvious that can be summarized by two trends: the decrease of metal grades and the increase of unwanted impurities. The statistics in *Figure 1* illustrate the metal grade decrease with two examples, one for the base metals zinc and lead and one for the special or minor metal gold.

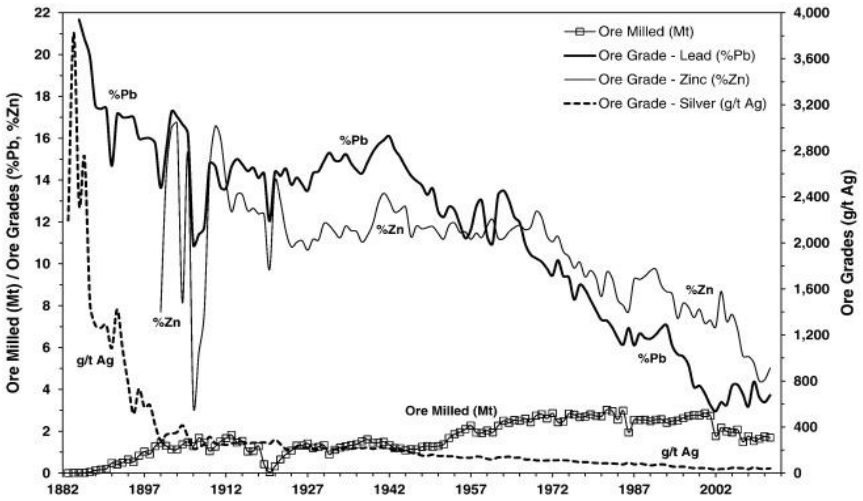

Figure 1

Decrease of metal grades in lead, zinc and gold ores [1]

The development of zinc and lead *(Figure 1*, left*)* clearly shows a decrease from about 10% in the 1970s to about 4 to 6% in 2016. This must be seen as a relevant change, especially considering that only a moderate development of smelting technologies took place within this time span. The same is true for gold resources, which dropped from the well-known 10 ppm content in the past to 2–4 ppm within the same period [1, 2].

In parallel, increasing iron values in zinc ores have become apparent, leading to much higher amounts of residues. These currently have to be landfilled due to a lack of reprocessing methods, thus causing an environmental problem due to residues which will have to be solved in the future. In case of gold, the multi-metal containing resources make economical gold extraction difficult, which is often caused by a lack of efficient recovery methods for the associated valuable metals. Additionally, more and more refractory type gold ores, often associated with arsenic, show reduced gold recovery due to a shortage of suitable liberation technologies.

Alternative metal supply by recycling might offer a certain compensation for declining ore qualities. However, as can be seen from *Figure 2*, the recycling rates of most of the metals are still relatively low. The illustration highlights the fact that the recycling rates of most of the important metals are far below 50%, raising the question of why there seems to be a certain limit in secondary metal production, even though recycling – especially of metallic scrap – is highly developed and applied in most regions of the world.

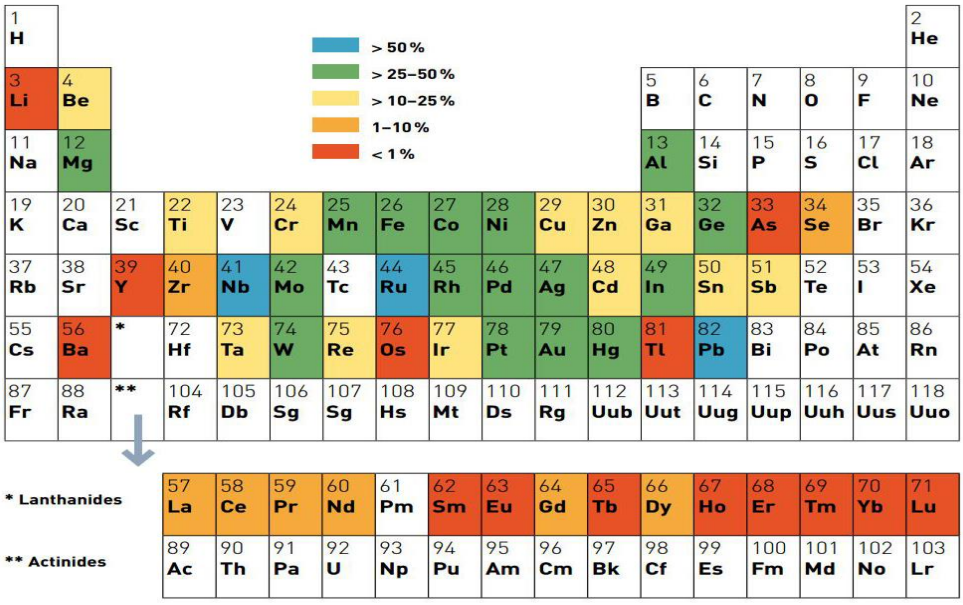

Figure 2
Recycling rates of various metals [3]

When having a closer look into metal processing circuits, it becomes obvious that several circumstances prevent higher recycling rates and make the dream of a circular economy, which is quite popular at the present time, unrealistic for this field of industry:

- The process used for metal production always produces a not so small amount of residues, often called by-products, which are often landfilled, even though they contain interesting amounts of valuable elements.
- Collection of the materials is difficult. Especially in Europe, many scraps and other secondary raw materials leave the continent via legal and illegal ways and cannot be seriously implemented into recycling circuits.
- Also, during recycling processes wastes are generated that contain valuable metals.
- In course of processing, part of the targeted metal is transferred into a form (e.g. low metal containing slag) out of which no recovery is possible due to energetic and thus economic reasons.

2. RAW MATERIALS LEAVING EUROPE

Europe nowadays faces the difficulty that even when raw materials are present, no matter if primary or secondary ones, they often leave Europe and are not available any more for metal production. Typical examples are automobile scrap, electronic scrap, and residues from the lead and zinc industry, but also copper and gold concentrates, to name just a few. This means that Europe has difficulties producing its own raw materials to become more independent, while available raw materials cannot be kept in Europe and are treated elsewhere.

The reasons for this strange situation can be listed as follows:

- high costs for energy
- high costs for labor
- strict environmental legislations
- strict safety regulations
- complicated approval and permission procedures
- lack of new or improved processing concepts that might be able to compensate for the above difficulties.

Of course, European citizens must be happy to live in a region of the world with highest safety and environment standards, but we must realize that this contributes to a lack of competitiveness with countries in Africa or Asia. Therefore, many European raw materials are treated outside Europe, which cannot be the beneficial strategy for the future.

In this context, a relatively new metal source, industrial by-products, have to be discussed, asking the question of whether they could represent an interesting raw material for Europe.

3. BY-PRODUCTS

For many decades, residues from metal production, such as slag, dust and sludge have often been qualified as waste that was simply dumped. This fact was – at least at that time – accepted by industry and involved authorities. Except for metal producing companies, no market participant really recognized that metal-bearing wastes were often landfilled to an amount that was more or less as high as the metal production itself. In the 1980s and 90s, the first environmental concerns called more attention to such dumps and residues. Nevertheless, due to inadequate technologies and low metal prices the interest in processing residues to recover valuables was still very low.

During the past few years, multi-metal recovery from concentrates has developed for both primary ores and secondary materials. In addition, minor metals contained in such residues have become important for daily life in industry. In other words, metals that did not have a real value in the past nowadays may essentially contribute to economic viability when recovered from residues.

In combination with increased metal prices and the need for special and rare metals in various highly sophisticated technologies (e.g. the electronics industry), more attention must be paid to such residues, which often represent a potential secondary resource. Currently, recycling rates are still low and huge amounts of residues are dumped annually.

Recycling is mainly based on scraps, where the elements in focus are available as pure metals. However, scraps have a defined volumetric limit and their treatment is already optimized to a certain level. As a matter of fact, considering the continuously dropping grades in primary ores, implying that new sources need to be exploited, recycling rates must be improved in the near future, as described above. As an important solution to this problem, by-products of various metallurgical processes *(*see *Figure 3)* already dumped or continuously being produced, have started to move into the focus of interest of both industry and research.

Screening the metallurgical area, residues emerging from the lead, zinc and copper industries must be considered. Processed ores commonly contain a high number of critical and valuable metals at the same time. Typical by-products are produced either in hydro-metallurgical or pyro-metallurgical process routes, as shown in *Figure 3*. Some of the contained metals are recovered to a certain amount by primary metallurgical processes but the bulk ends up in different waste streams.

Very often sludge from hydrometallurgical operations and dust from pyrometallurgical operations offer a significant number of metals at concentration levels that might be of economic interest. In addition, some recycling processes of highly diversified and contaminated scraps (e.g. car bodies or waste electric and electronic equipment) generate complex by-products.

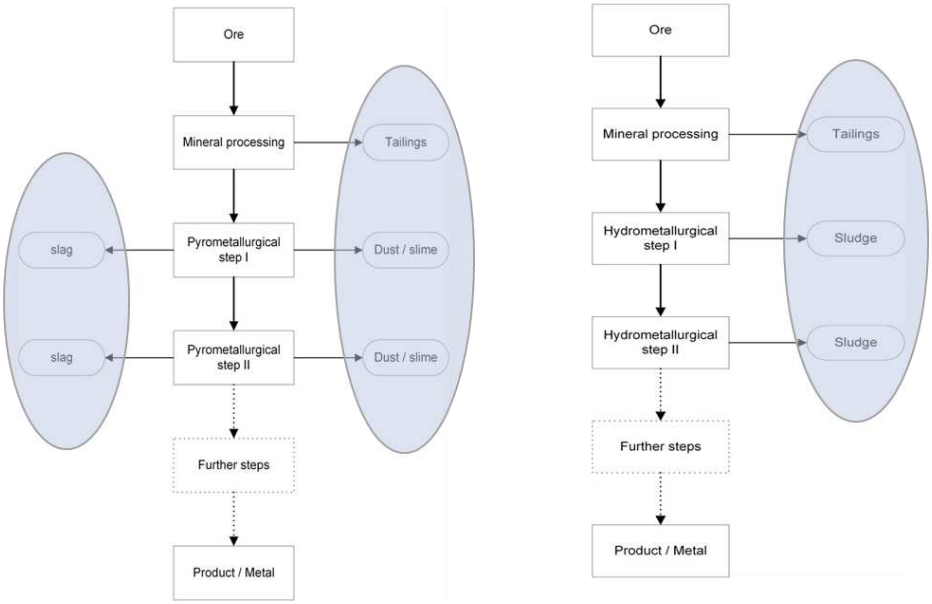

Figure 3
By-products of metallurgical processes

Figure 4 illustrates the possible recoverable elements but also shows the high overall metal content available in currently produced residues.

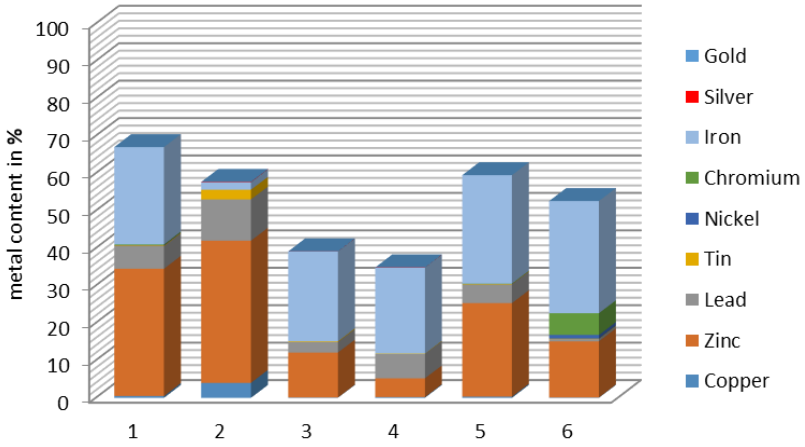

Figure 4
Examples for different residues and their metal content (except PGM) out of own investigations
(1 – Electric Arc Furnace steel mill dust, 2 – Dust from copper recycling, 3 – Slags from lead industry, 4 – Jarosite from zinc industry, 5 – Dust from cupola furnaces, 6 – Stainless steel production dust)

These residues can be found worldwide in huge quantities, either on dumps dating from the end of the last century or being currently produced, and they form an interesting secondary resource of metals with high availability. Due to the long European history in mining and metallurgy, such landfilling sites and producing mills are still present and have to be considered as 'part of the market' [4, 5].

Some of the residues described in *Figure 4* are already recycled to a certain extent. However, also for these secondary materials the worldwide recycling rates are still well below 50% for two main reasons:

- the lack of optimized processes
- missing information and data about the materials.

Both factors are responsible for the inefficiently utilized potential on secondary resources [4].

Another reason for the weak exploration and use of residues is the lack of any guideline or competence describing how to evaluate residual materials. This is partly due to the lack of adequate databases. For primary materials like metal ores, codes exist that serve as accepted and applied guidelines for a qualified evaluation by following pre-defined steps, leading to a "bankable feasibility study". Such guidelines currently do not exist for secondary materials. A consequent "stepwise approach" must be applied right from the beginning of the project.

4. ASSESSMENT OF METAL-BEARING BY-PRODUCTS

Montanuniversität Leoben has started to develop guidelines for the assessment of specific metal-bearing by-products to allow a clear perspective on how valuable typical materials are.

Two main areas are important from the technical point of view: 4.1. "Characterization of by-products" and "Processes development and product quality".

4.1. Characterization of by-products

Depending on the feed material used and the treatment technology applied, various residues with different properties emerge that can be distinguished by their origin or properties. Some of the residues mentioned above have already been investigated to a certain extent with respect to characterization and a first evaluation.

Detailed geochemical and mineralogical characterization of metallurgical residues is of highest importance in order to develop appropriate mineral processing recipes and then appropriate metallurgical methods to recover all metals of interest. Hence, the following questions need to be answered:

(1) Which particles contain the metals to be recovered?
(2) What is their particle size, shape and texture, i.e. zoned grains, coated grains?
(3) How intensive/complex are incorporated phases intergrown in different particle fractions?
(4) What is the concentration level of metals in the major particles?
(5) Presence and concentration of deleterious elements (such as As, Cd, Hg)?

In order to separate minerals or metallurgical phases by means of mineral processing techniques with physical, physical-chemical and/or chemical methods it is necessary to know the relevant phases regarding the key aspects mentioned above. In the end, the size, shape, structure and the chemical and mineralogical composition define a particle [6].

Deriving from these parameters, the density, optical, electrochemical, thermal, chemical and mechanical characteristics of any particle can be determined. As the way of managing a metallurgical process and its actual parameters highly affect the residues – not only in composition but also in structure – the variance of the residues' properties with regard to mineral processing characteristics is large, even for an existing plant in operation. In analogy to primary mineral deposits, processing results may vary widely if these changes are not taken into account. Thus, the residue has to be investigated and characterized properly.

Based on that, the main goal is to generate a basis for assessing possible metal or metal compound recycling methods. Additionally, the different metallurgical possibilities for treatment – hydro- or pyro-metallurgical – need to be determined. These results are mandatory for evaluating possible process steps to generate products from the residues. To generate this information, the main properties such as melting behavior, volatilization behavior, reducibility, and solubility need to be determined in advance by using special metallurgical characterization procedures.

4.2. Process development and product quality

To cope with the continuously stricter environmental legislation along with a shortage of critical metals in Europe, the process development for treatment of secondary resources and the optimization of existing processes are two major concerns. The challenge of the years to come is to minimize newly generated residues and at the same time to achieve maximum product quality within the recycling process. In addition, the quality of the products influences the targeted market and achievable revenues. Therefore, state-of-the-art processes have to be continuously adapted regarding energy consumption, mass-balancing and further improvement of the product quality. A specific geochemical, mineralogical and metallurgical characterization creates the basis for improving such existing processes. Thus, it will be possible to obtain higher product qualities and lower amounts of newly generated waste streams.

As demonstrated by several investigations carried out at Montanuniversität Leoben, the residues are not at all homogenous. Hence, it is not possible to recycle such residues as one combined single input stream. In order to increase the recoverable metal grade and to reduce the content of substances that hinder the metallurgical process, some separation by physical/mechanical techniques is required. If such a process shall be developed systematically rather than by trial-and-error, the residue must be characterized properly in terms of its properties relevant for a separation process.

Fractional analysis is the standard tool in mineral processing for assessing the amenability of primary mineral resources to be upgraded to saleable products of defined and consistent quality. Taking into account the heterogeneity of the residues, it is expected that some upgrading is possible, which may pay off during recycling. Fractional analysis yields the optimum results for separating a given feed material by assuming perfect separation. It thus also serves as a benchmark for assessing the performance of an existing process. The possible benefits of assessing and processing the residues in a similar way to primary mineral resources are obvious. As some common properties of the residues (e.g. the generally fine particle size distribution of dusts, just to name one) are problematic in fractional analysis, the methods require further adaptations.

In order to find the suitable processing chain, tests need to be carried out. Once a residue is tested, the obtained data will be collected and condensed in a database, which acts in future assessments as a decision support tool. Although similarities within the same type of material (e.g. slags, dust) can be found, each residue is generated in slightly different processing routes with varying input material. This leads to variable extraction yields, consumable consumption, energy input, obtained product quality, etc. Based on the experimental results the database will grow, and the more materials are cataloged, the more accurate the data for the assessment becomes.

One major disadvantage of past attempts in recycling by-products was that often just one single metal was recovered while possible further valuable metals were distributed into newly generated wastes and were therefore lost for production. Pyrometallurgical concepts allow the recovery of valuable metals by applying different basic operations: forming a volatile phase, where e.g. zinc or lead can be collected as oxides in the off-gas, or forming a liquid metal phase, where e.g. iron or lead act as an efficient collector for various minor metals. In combination with mineral processing steps, where a separation of metal containing fractions could be realized prior or subsequent to a metallurgical step, targeted multi-metal recovery can be realized. For hydrometallurgical approaches the dissolution of a larger number of elements followed by selective precipitation, again combined with mineral processing, would offer multi-metal recycling. However, also a combination of hydro- and pyro-metallurgy could lead to appropriate solutions [6].

Given the situation that for some by-products recycling techniques do not exist, and that the majority of methods recover only one metal, such an approach must be regarded as an essential novelty.

4.3. Economic considerations

Within the investigations also a model for economic verification was established and different dumps worldwide have been investigated. Within this evaluation very promising dump sites have been detected, as well as residues of poor quality.

Economic analyses were done for different materials and metal prices. As already mentioned above, gold and silver contribute in a very important way to the

overall revenues of the various process concepts. However, the key message is that multi-metal recovery is essential for the economic stability of a recycling process and allows a higher flexibility regarding varying metal prices.

5. SUMMARY

By-products from the metallurgical industry can play an important role as a secondary resource for different metals in the future. Detailed evaluation and assessment of the materials is important for successful utilization, offering interested parties a reliable information tool similar to already existing guidelines for primary resources. Important steps towards such an assessment concept are advanced characterization of the by-products combined with sophisticated processing concepts, which in certain cases might be already available but may benefit from new developments. Especially the idea of recovering more than one metal from by-products would allow economical and ecological utilization of such wastes and will form an important strategy for the future.

REFERENCES

[1] Mudd, G. (2007): An analysis of historic production trends in Australian base metal mining. *Ore Geology Reviews*, 32 (1–2), pp. 227–261.

[2] Gold ore grade evolution (2015): http://www.wikiwand.com/en/Gold_mining #/cite_ref-Postan_&_Miller_6-0, retrieved February 2019.

[3] Reuter, M. A. (2013): *Metal recycling*. United Nations Environment Programme.

[4] Antrekowitsch, J., Steinlechner, S. (2011): The Recycling of Heavy-metal Containing Wastes: Mass Balances and Economical Estimations. *JOM*, 63, 1, pp. 68–72.

[5] *Mineral Yearbooks. Volum III, Area reports* (2016): *National Minerals Information Center, United States Geographical Survey.* Online-version, various country reports, http://minerals.usgs.gov/minerals/pubs/country/index.html# pubs, retrieved June 2018.

[6] Antrekowitsch, J. (2016): Recycling of Poly-Metallic Residues from Metal Industry – Current Status and Future Developments. *Proc. of TMS 2016, 145 Annual Meeting & Exhibition – REWAS*, Nashville, USA.

Geosciences and Engineering, Vol. 7, No. 10 (2019), pp. 14–27.

PURIFICATION OF ALUMINUM SALT SLAG BY LEACHING WITH ACID OR ALKALI SOLUTIONS FOR ALTERNATIVE UTILIZATION

B. HEGEDÜS – T. KÉKESI

Institute of Energy and Quality, University of Miskolc

Abstract: The melting of aluminum scrap is accompanied by the generation of dross consisting of an oxide matrix and a large proportion of entrapped liquid metal. The general practice is to recover the entrapped metal at high temperature and apply mechanical forces in rotary furnaces with the addition of a large amount of NaCl-KCl based salt. The residual dross (salt cake/slag) is categorized as hazardous waste and is usually disposed of despite its potentially containing non-metallic components. We examined the structure and composition of extreme types of the residual dross applying instrumental techniques. Chemical leaching experiments were carried out applying acid, alkaline and neutral media to eliminate the unwanted components. In all cases, the chloride salts can be fully removed and recycled, while dilute sulfuric acid proved to be efficient in eliminating the still remaining metals. After removing the basically NaCl-KCl salt content, the residue may be suitable as an additive to ceramic materials used in the construction industry.

Keywords: *Aluminum dross, aluminum recycling, salt recovery, hydrometallurgy*

1. INTRODUCTION

As the primary resources are hardly capable to provide enough raw material for the strongly increasing need for aluminum in the world, some countries with bauxite reserves and processing traditions, like Hungary, are also changing the structure of the aluminum industry to be based mostly on secondary raw materials. The global share of secondary production is currently approaching 35%, while the ratio in Hungary is well beyond 70% [1]. Primary metal is mainly used for metallurgical production of the required compositions of usually low Al-Fe and Al-Si alloys. The metallurgical recycling of scrap Al consumes ~95% less energy than primary production and dangerous emissions can also be avoided [2]. The increasing share of obsolete scrap recycled from consumption causes an increased dross formation in the usually applied gas-fired melting furnaces. The thicker non-metallic layers on the usually large specific surface area entail a higher degree of oxidation during melting [3] [4]. The molten drops of the metal are isolated and they can be unified in a molten pool only by the influence of mechanical forces and special salts breaking the oxide barriers. The oxidation of the dispersed aluminum and especially of magnesium, a common alloying component, is highly exothermic, possibly causing an extreme local

superheating which, in turn, results in an increased rate of oxidation. The highly negative Gibbs free energy change (< –900 kJ/mol O_2) associated with the oxidation of Al and of Mg at the typical melting temperature results in extremely high stability of the oxides [5]. Oxidation is also highly likely due to the main furnace gas components, CO_2 and H_2O, arising from natural gas combustion. The principal oxide components of the dross are Al_2O_3 and MgO or the spinel compound $MgAl_2O_4$ when melting AlMg alloys. The spinel causes great structural changes, resulting in higher dross volumes. Due to the high exothermic heat of aluminum oxidation (<1,100 kJ/mol O_2), the surface of the melt can be superheated and such solid phases as AlN and Al_4C_3 can also form.

The oxides of aluminum and also of magnesium do not form a protective slag layer, as they are solid at the temperature of melting. Despite the higher densities, their fine particular shape and the high surface tension results in the formation of the heterogeneous dross layer at the surface of the melt [6]. Beside direct oxidation, most of the metal loss can be caused by physical entrapment in the heterogeneous dross layer, usually removed manually from the surface of the metal bath after melting. The metallic content of the aluminum melting dross may reach as high as 70–80% by weight, which is usually removed by hot (thermo-mechanical) treatment [4] in a converter-type rotary furnace applying the addition of a significant amount of NaCl-KCl based salts and physical forces to liberate the metal droplet from the oxide matrix. As shown in *Figure 1*, the heterogeneous material is heated, while the oxide structure is broken by the abrasive and pressing forces arising from the rotation.

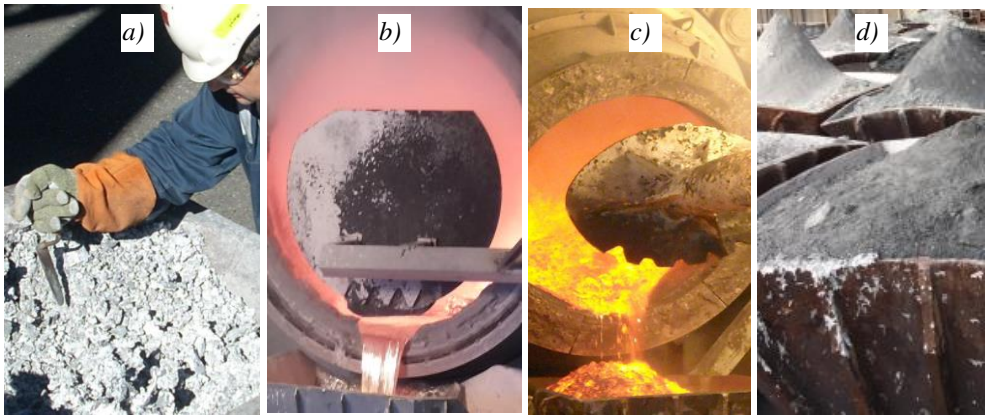

Figure 1
Hot (thermo-mechanical) treatment of aluminum dross to recover the entrapped metal
[a) primary dross to be charged, b) aluminum tapping, c) removing the residual dross, d) cold residual dross – salt cake – for disposal]

The tapped metal is aluminum, containing the less reactive alloying components, while Mg is almost entirely lost by selective oxidation, generating extra heat. As

most of the entrained metal content can be recovered by this process, the residual dross (salt cake) usually consists of mostly the oxides and the salt components, accompanied by a low (2–10%) concentration of metal. The amount of this residual dross may be measured in several thousands of tonnes in Hungary. As no significant metallic value can be recovered from it, and its oxide and chloride components cannot be utilized in this form, the major part of it is disposed of. It is even considered hazardous because of the water soluble and reactive compounds it contains. In order to make the hot treated residual dross also useful, it is imperative to separate the salt and the oxide constituents. The recovered salt can be recycled to the thermo-mechanical treatment of the primary aluminum dross. The salt-free final residue, containing mostly the oxides and a minor amount (a few percent) of aluminum metal, could be utilized for different industrial applications such as:

- raw material for geo-polymer production
- additive to special cements and concrete (to improve thermal insulating properties)
- additive to asphalt (to increase wear resistance)
- additive to produce glass foams (to increase strength and heat insulation)
- slag forming agent in steel making (in ladle metallurgy).

However, all of the alternative applications would require an almost complete elimination of the chloride components from the residual dross [7]. The remaining little metallic aluminum content may be useful (in steel slag modification) or irrelevant as it is dispersed and covered by a firm oxide layer (in the other potential applications noted).

The salt in the residual dross contains basically NaCl and KCl, which may be dissolved in any aqueous solution at ordinary temperatures [8]. The obtained brine can be evaporated for significant chloride salt recycling. The minor CaF_2 component may not be recovered by leaching, but can be supplied additionally to the recycled chlorides. A preliminary grinding step may be followed by a physical separation of the larger malleable particles containing a predominant metallic core, or added directly to the leaching step to produce a brine of approx. 25% saturation for efficient dissolution, but also subsequently the energy saving removal of water by evaporation. Side reactions occurring as a result of the high-temperature treatment of the dross may occur, producing some noxious gases too:

$$AlN + 3H_2O = Al(OH)_3 + NH_3 \quad (1)$$

$$AlN + NaOH + H_2O = NaAlO_2 + NH_3 \quad (2)$$

$$Al_4C_3 + 12H_2O = 4Al(OH)_3 + 3CH_4 \quad (3)$$

If acidic or alkaline solutions are present, the minor metallic aluminum content may also be dissolved:

$$2Al + 3H_2SO_4 = Al_2(SO_4)_3 + 3H_2 \quad (4)$$

$$Al + NaOH + H_2O = NaAlO_2 + 1.5H_2 \quad (5)$$

The reactions above – especially the last two – are exothermic, which will beneficially increase the temperature. These effects may also be present if the residual dross is disposed of in the environment.

There are proposed technologies [9] which promise 99% recovery of the salt and a low (< 0.2%) chloride content in the final residue, and where the harmful gases evolved during the hydrometallurgical treatment are combusted. The generated heat of dissolution can be utilized for the evaporation of water. Although the proposed hydrometallurgical process may seem straightforward, there remain questions of dissolution kinetics, efficiency of solid/liquid separation by decantation or filtering, solubility of metals, the application of acid or alkaline media, purity of the solid residue and the efficiency of evaporation. These questions required clarifications by fundamental experiments.

2. THE EXAMINED TYPES OF THE RAW MATERIAL

The residual dross samples collected at an industrial site for the thermo-mechanical treatment of aluminum melting dross were used as the raw material for the examinations and the experiments. They represent two extreme cases and belong to a common category by sight. They are obtained as residues from the same rotary furnace illustrated in *Figure 1*, but they are quite different in color. One extreme type is light – almost white – while another is definitely dark – almost black – and other samples have the most common gray appearance. The metallic content was determined by a special method [10]. It is divided into a physically obtainable and a hidden fraction, left in the finely ground powder after grinding and classification. The latter part can be determined only indirectly by collecting the hydrogen gas evolved from reaction (5) carried out in hot and concentrated NaOH. This method has pointed out a total metal content of 9.9%, (with 1.1% in the powder fraction) of the ground light-colored residual dross and a total metal content of 13.6% (with 4.5% in the powder fraction) of the dark material. No metal could be obtained from either sample through repeated thermo-mechanical treatment in the laboratory induction furnace with more salt addition, whereas – after granulating the hot material in water – grinding and classifying resulted in a fine fraction of ~90% of mass from both materials. *Figure 2* displays the characteristic photographes and the EDS spectra taken during the Scanning Electron Microscopic (SEM) analysis and also the X-ray Diffraction (XRD) spectra of the fine (< 250 μm) fractions obtained after grinding the extreme types of the hot treated residual dross materials.

The XRD spectra reveal that the light-colored dross residue mainly consists of α-Al_2O_3, while the dark residue exhibits a relatively large proportion of the salt components. In the former case, the thermo-mechanical treatment of the primary dross from the aluminum melting could be more intensive, resulting in the evaporation of the added salt, severe oxidation of the dispersed metal content, and the formation of AlN. However, metallic aluminum was neither detected appreciably in the dark sample, which may have gone through a milder thermo-mechanical treatment. This is understood as the residual metal is dispersed and covered by a thick oxide layer.

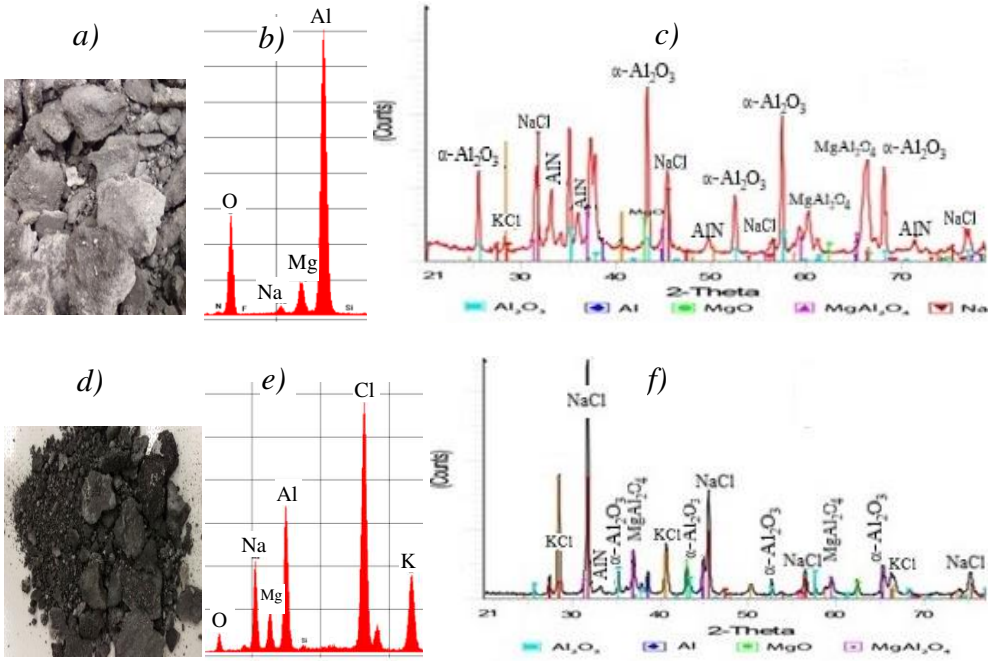

Figure 2

Macro images, EDS and XRD spectra of the light (a, b, c) and the dark (d, e, f) coloured dross residues from the thermo-mechanical treatment

Only the analytical method based on the collected volume of the H_2 evolved from reactions (4-5) could reveal the real metal content hidden under the oxide coatings of the fine particles [10]. Apart from the extreme types, some samples were collected from the common gray dross residues. However, they were identified by the Mg content of the metal phase in the primary dross treated in the industrial thermo-mechanical processing, as indicated by the images and the relevant XRD spectra of *Figure 3*.

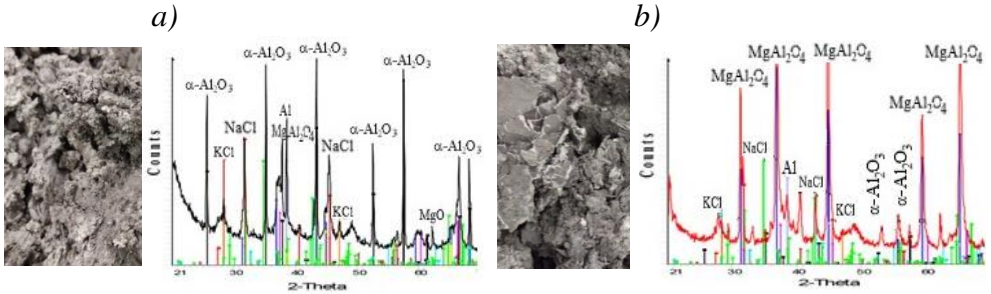

Figure 3

The SEM images and XRD spectra of the residue from the hot treatment of primary dross batches obtained from the melting of aluminum alloys containing low (a) and high (b) Mg

The visual appearance of the two residual dross samples is quite similar, but the XRD spectra reveal some differences. Due to the Mg alloying, the spinel $MgAl_2O_4$ phase appeared in the residual dross, while the salt and metallic Al content diminished. This can be attributed to the strongly exothermic reaction of Mg oxidation during the hot dross treatment.

3. THE EXPERIMENTAL PROCEDURE

The goal of the proposed hydrometallurgical treatment was to remove the remaining salt and metal content from the thermo-mechanically treated residual dross. Thus the most suitable cases to be examined are related to the dark dross of high salt content and the gray sample obtained from the hot treatment of the most usual primary dross with a medium high-Mg metallic phase in it. The fine fraction (<250 μm) of the ground residual dross samples obtained from the industrial thermo-mechanical processing was leached in two series of experiments. At first, the kinetics and the equilibrium of dissolution were examined by applying 16.3% H_2SO_4 for various times. In the second series, the elimination of the components was investigated by complex procedures involving repeated leaching with 8.5–23.5 m/m% H_2SO_4, followed by filtering combined with water rinsing or simple decantation and multiple steps of washing with water. As an amphoteric metal, Al can also dissolve in alkaline solutions, and NaOH may efficiently react also with the oxide layer at the surface of the metal particles [8]. The alkaline reagent may enhance the dissolution of the entrapped aluminum, constituting overwhelmingly the remaining metal in the hot treated residual dross. Therefore, further elimination tests were carried out with 3–6M NaOH solutions applied in similar multi-step procedures, providing a reference. The main steps of the laboratory leaching experiments are shown in *Figure 4*.

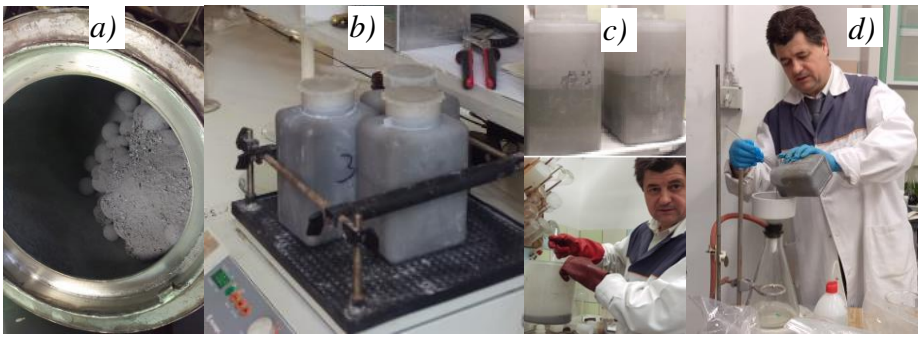

Figure 4

The main steps of the hydrometallurgical procedure: a) – grinding, b) – leaching, c) – settling and washing, d) – filtering

The concentration of the applied dilute sulfuric acid corresponds to a 10% volume ratio, which is convenient to prepare, and is preferred in hydrometallurgy [5] [11]. To examine the reaction rate, 10 g or 20 g samples were contacted with 100 cm^3 of

the solutions, which was a safe ratio to provide complete solubility. A horizontal shaking machine assured virtually homogeneous dispersion in reactor bottles of 300 cm^3 in volume. The kinetic experiments were carried out for various times, and further examinations included 1 h leaching times to allow equilibration. The larger scale experiments examining the elimination of the salt content in the various dross samples were usually carried out with 300 g material samples contacted with 500 cm^3 of fresh solutions in each step of the complex hydrometallurgical procedure, applying 1,000 cm^3 reaction vessels (as shown in *Figure 4b*). The concentrations of the chloride and the hydrogen ions were determined by classical titration, but the concentrations of the dissolved metals were analyzed by Atomic Absorption Spectrometry (AAS). The results are given as yields of the indicated elements (or compounds) relative to the masses of the leached dross samples. In order to check the analytical results and to demonstrate the possible recycling of the salt content removed by leaching, the solutions obtained from the aqueous treatment were evaporated to dryness by the application of a rotary vacuum distilling equipment. The process and the resulting salt products are shown in *Figure 5*.

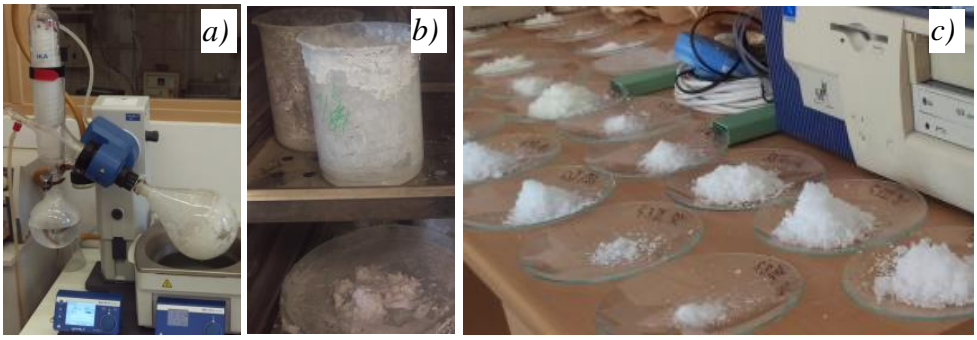

Figure 5
Salt recovery
[a) – rotary vacuum evaporation, b) – drying in oven, c) – products]

As the NaCl and KCl components are the only water soluble compounds in this material [8], applying water leaching as a first step to the residual dross means only these basic salt components are dissolved. Therefore, after evaporation to dryness, the recovered salt is pure and can be recycled directly to the hot treatment of the primary dross for aluminum recovery.

4. EXPERIMENTAL RESULTS AND DISCUSSION

Although the dissolution of NaCl and KCl can be considered complete in a short water leaching, irrespective of the S/L ratio in the 10 : 10 to 10 : 100 g/cm^3 range [12], the purification of the hot treated residual dross requires also the removal of the contained metallic components. The most convenient method is to apply a dilute

sulfuric acid reagent. This is equally efficient in removing the chloride salts, but it may also dissolve the metallic aluminum content.

4.1. Kinetic behavior and solubility

The kinetic behavior of the extreme types of 10 g batches of the residual dross as leached with water or H_2SO_4 solutions of 100 cm^3 volume is expressed in *Figure 6* in terms of yields of the dissolved elements (masses relative to the mass of the raw material).

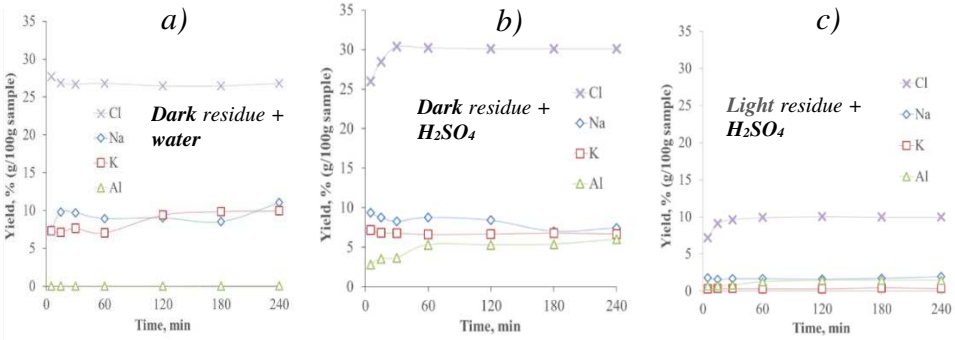

Figure 6

Dissolution rates of NaCl, KCl and Al in water (a) or 16.3% H_2SO_4 (b, c) from the dark (a, b) and the light-colored (b) extreme-type dross samples obtained from industrial hot treatment

The Na and K concentrations analyzed by AAS can be used for calculating the relative amounts of the removed salt. This value reached the stabilized maximum level in the solutions obtained after the shortest time (10 min) of leaching. It corresponds to a salt yield of 36% relative to the solid sample mass. A prompt argentometric analysis was also used as a direct indication of the dissolved salt; however, the acid medium could cause positive error by converting the potassium chromate indicator to the inert chromic acid form in a larger proportion. As the most practical agent for purifying the dross, sulfuric acid was also efficient in removing metallic aluminum. The stabilized concentration of dissolved Al shows a ~6% recoverable aluminum metal content in the dark sample. The necessary leaching time to reach the maximum Al concentration was found to be significantly longer than for the salts, reaching approximately 60 minutes. The dissolution test also shows the difference in the composition of the two extreme types of the hot treated residual dross. The removed salt and the metallic Al contents were 5–7 times higher in the dark sample than in the light one.

In order to compare the purifying effects of the acidic and the alkaline media and also of water, finely ground samples of the dark residual dross were leached for one hour with water, 16.3% H_2SO_4 or 6M NaOH, then rinsed with water and dried at 105 ^oC to be analyzed again by XRD. *Figure 7* shows the phase compositions of the solid residues obtained from these tests for comparison.

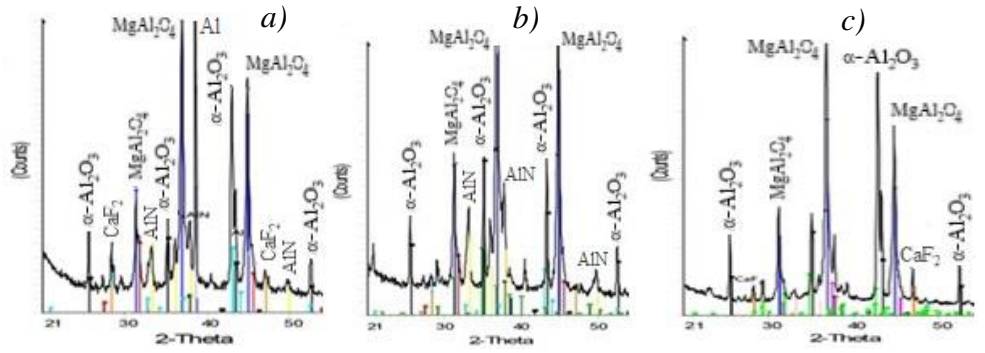

Figure 7

XRD spectra of the solid residues after leaching the dark hot-treated dross with water (a), with 16.3% H_2SO_4 (b), or with 6M NaOH (c)

The XRD spectrum of the material leached with water demonstrates complete removal of the chloride salts, while AlN and CaF_2 peaks are clearly detected. Metallic aluminum is also found, although the oxide coating of the dispersed particles makes them less detectable. The XRD spectrum obtained after the sulphuric acid leaching shows a similar predominance of the stable $MgAl_2O_4$ and α-Al_2O_3 compounds, but metallic aluminum was no longer detected. The CaF_2 may have been removed by the acid leaching followed by the water rinsing. This suggests a conversion of the fluoride into the sulfate form, which may have been removed mostly by the subsequent water rinsing. The residue after the strong NaOH leaching showed the same $MgAl_2O_4$ and α-Al_2O_3 matrix, but AlN also disappeared along with the metallic Al. This proves the higher intensity of reaction (2) in alkaline media. The highest AlN peaks – relative to the matrix – are in the residue obtained after the H_2SO_4 leaching, which suggests that the acidic solution may depress the unwanted evolution of NH_3 by reaction (1) and (2).

4.2. Elimination efficiency

In order to formulate an efficient and economical procedure for purifying the secondary dross left behind from the hot treatment of the primary melting dross, it is important to apply the minimum amount of solutions and the fewest possible steps in leaching and in the subsequent washing/rinsing, combined with the most practical solid/liquid (S/L) separation. The possible efficiency of the consecutive steps was examined by applying different concentrations of the reagent in the repeated leaching steps. The subsequent washing steps were carried out in the same way, applying distilled water. Each step was repeated after decanting the practically clear solution and replacing it with a fresh one; however, between the leaching and the washing cycles, a filtration step was included for a more complete S/L separation combined with water rinsing. The common type (gray) secondary dross was used and the S/L ratio was generally ~300 g/500 cm^3 in all the steps; however, an uncertain practical error of incomplete separation by decantation could not be excluded.

Each combined procedure consisted of repeated leaching, rinsing-filtering, multiple washing, and a final rinsing-filtering steps. Although the removal of the chloride salts is independent from the added acid or alkali reagents, all of the major elements contained in the dross were analyzed in the leachates. Elimination of the metals was examined with 8.5, 16.3 and 23.5% (m/m) H_2SO_4, and 3, 4, and 6 mol/dm^3 NaOH leaching solutions applied in 30 minutes repeated leaching steps. The total leaching time of 60 minutes was to reach the maximum dissolution, as suggested by *Figure 6*. Washing was carried out for 10 minutes and filtration time was determined by the permeability of the cake and the vacuum (~100 Pa) applied by the rotary pump. The results of the multi-step purification procedures with different concentrations of H_2SO_4 in the leaching solutions are illustrated by the cases shown in *Figure 8*.

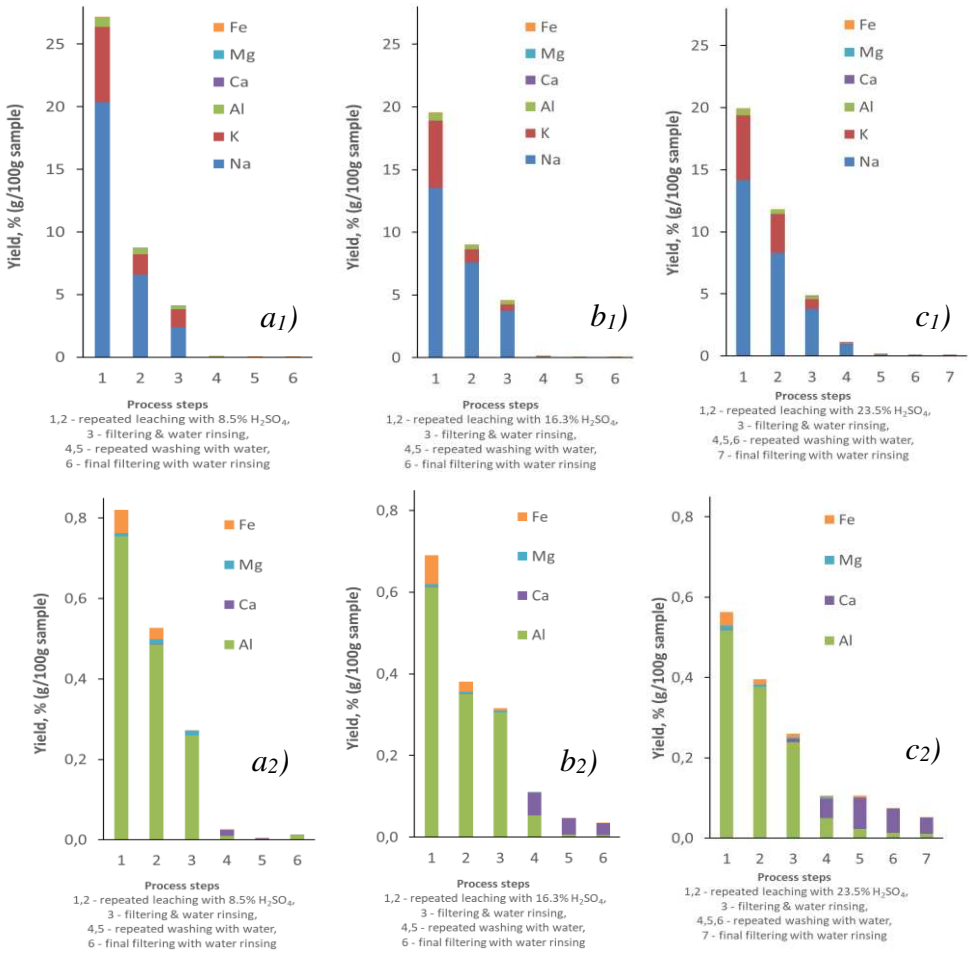

Figure 8

Metal yields obtained by leaching with 8.5% (a_1, a_2), 16.3% (b_1, b_2), and 23.5% (c_1, c_2) H_2SO_4 followed by rinsing and washing with water to purify the common type residual dross

The distribution of the eliminated components among the consecutive steps is affected also by the characteristics of the S/L separation. This is particularly important in the leaching steps, where the solute concentrations are the highest. As suggested by *Figure 8*, the removal of the solutes was most complete in the first case, where 8.5% H_2SO_4 was applied for leaching *(Figures 8a1* and *a2)*. In the other two cases more the dissolved components were carried over to the subsequent steps. However, the total amounts of the eliminated components were practically the same, irrespective of the applied H_2SO_4 concentration in the examined range. The elimination of the chloride salts was complete after the third or fourth step, but aluminum and the other metallic components required all of the included steps to become practically perfectly eliminated. The assumption of the partial conversion of the insoluble CaF_2 into the sulfate, which could be dissolved at a low rate by water in the subsequent washing steps, is also supported.

Similar elimination procedures were carried out with different NaOH solutions applied for leaching the same kind of dross. In this case, the primary purpose was complete elimination of the metallic aluminum. The oxide coated metallic particles can be more completely liberated by an efficient destruction of the covering layer [13]. The results of the direct NaOH leaching experimental series are illustrated in *Figure 9*.

The total removed amounts of aluminum by leaching with NaOH in the 3–6 mol/dm^3 range was virtually the same, and the differences in its distribution among the subsequent steps can be caused only by the inconsistency in the quality of the S/L separations. The comparison of the results in *Figures 8* and *9* shows that the NaOH leaching solutions were capable of dissolving approximately three times more aluminum than those of H_2SO_4. This proves the assumption that some metal particles are covered with thick oxide coatings that can be destroyed more efficiently by the action of the strong alkali. This reaction increases the dissolved Al concentration both directly and indirectly. The direct effect is related to the dissolved oxides, and the indirect is the dissolution of the thereby liberated metal particles. Although the ratio of these two sources is not known, the practical goal of eliminating the metallic Al phase has been proven possible. Alkaline leaching may be more efficient for removing the soluble Al_2O_3 and the hidden aluminum content from the residual dross; however, H_2SO_4 can remove also iron and the other alloying or impurity metals that are soluble in acid, and may also mobilize the CaF_2 content.

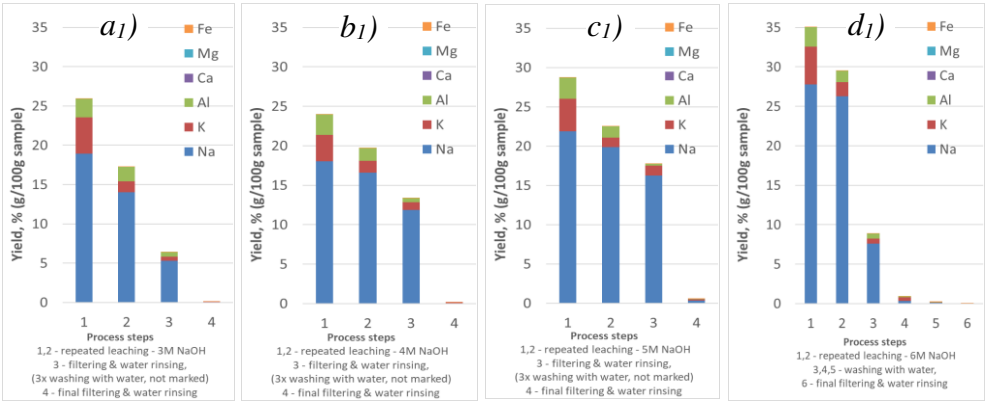

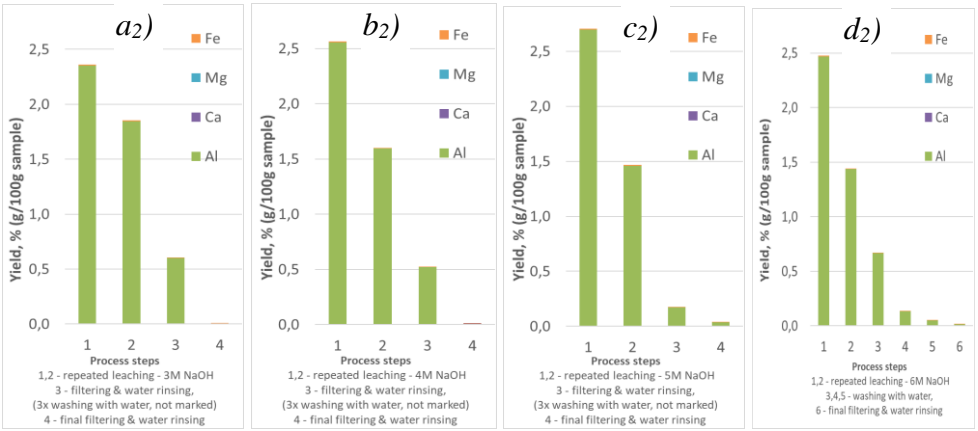

Figure 9

Metal yields obtained by leaching with 3M, (a_1, a_2), 4M% (b_1, b_2), 5M (c_1, c_2) and 6M (d_1, d_2) NaOH, followed by rinsing and washing with water to purify the common type residual dross

5. CONCLUSIONS

Leaching the final dross obtained from the hot treatment of the aluminum melting dross with H_2SO_4 or NaOH of varied concentrations removed the chloride salt content within several minutes. The acid also leached the more exposed remaining metal particles, whereas the alkaline leaching was able to also efficienty dissolve the more hidden aluminum particles and their oxide coatings. For efficient purification of the oxide matrix, the finely ground dross should be leached at room temperature, applying shaking (with a S/L ratio of 3 : 5 g/cm^3), followed by filtering combined with water rinsing. The reaction of AlN, also present in the residual dross from the hot treatment, can occur with water, and especially with alkaline solutions, to produce unpleasant NH_3 emissions. The removal of the chloride salts can be carried out separately in a preliminary water leaching procedure. If this is followed by evaporation to dryness, these salt components can be recycled to the hot treatment of the melting dross. Further purification steps by either acid or alkaline leaching can be carried out as required by any potential application of the oxide residue, e.g. in producing special cement and glass foams or geopolymer materials, or in conditioning asphalt. Application in steel making, however, only requires the removal of the chloride salts, as the remaining metallic aluminum is useful in conditioning the slag of steel ladle metallurgy. The residual minor amount of metallic aluminum is mostly covered by an oxide layer, making it virtually inert for applications in the construction materials industry.

ACKNOWLEDGEMENTS

The research was carried out in the Centre of Applied Materials Science and Nano-Technology at the University of Miskolc. The described study was carried out as part

of the EFOP-3.6.1-16-2016-00011 *Younger and Renewing University – Innovative Knowledge City – institutional development of the University of Miskolc aiming at intelligent specialisation* project implemented in the framework of the Széchenyi 2020 program. The realization of this project is supported by the European Union, co-financed by the European Social Fund.

REFERENCES

[1] Galevsky, G. V., Rudneva, V. V., Alexandrov, V. S. (2018): Current state of the world and domestic aluminium. In *IOP Conference Series: Materials Science Engineering, 411 012017*, doi:10.1088/1757-899X/411/1/012017.

[2] Schlesinger, E. M. (2017): *Aluminum recycling*. Boca Raton, London, New York, CRC Press.

[3] Han, Q. (2003): Dross formation during remelting of aluminium 5182 remelt secondary ingot (RSI). *Materials Science & Engineering,* vol. A363, pp. 9–14.

[4] Tóth, G. B., Harangi, Z., Kulcsár, T., Kékesi, T. (2013): Metal content of drosses arising from the melting of aluminium. In: *XXVII MicroCad International Scientific Conference*, Miskolc, Hungary, 21–22 March, 2013, Section C-D, p.12.

[5] Gilchrist, J. D. (1979): *Extraction metallurgy*. 2nd rev. ed., London, Pergamon Press.

[6] Ho, F. K., Sahay, Y. (1990): Interfacial Phenomena in Molten Aluminium and Salt System. In: Van Linden, J. H. L. et al. (eds.): *2nd Int. Symp. Recycling of Metals and Engineered Materials*, Williamsburg, Va, 28–31 October, TMS, Warrendale, pp. 85–103.

[7] Xiao, Y., Reuter, M. A., Boin, U. (2005): Aluminium Recycling and Environmental Issues of Salt Slag Treatment. *Journal of Environmental Science and Health,* vol. 40, pp. 1861–1875.

[8] Bruckard, W. J., Woodcock, J. T. (2009): Recovery of valuable materials from aluminium salt cakes. *International Journal of Mineral Processing,* vol. 93, pp. 1–5.

[9] Olper, M. Kaspar, T. (1994): The Engitec System for Treatment of Salt Slag from Secondary Aluminium Smelters. In: *Metal Bulletin's Fourth International Scrap & Secondary Metals Conference*, March, 21–23, Amsterdam, The Nederlands, https://www.ips-engineering.net/Doc/Engitec/STE%20Process.pdf, 1994.

[10] Kulcsár T., Kékesi, T. (2017): Thermo-mechanical extraction of aluminium from the dross of melting AlMg scrap. In: *MultiScience – XXXIst microCAD Int. Multidisciplinary Scientific Conference*, Miskolc, Hungary, 20–21 April, Section D, p. 9.

[11] Bar, D. L., Barket, D. (2015): The leaching of sulfide iron (II) with sulfuric acid. *Journal of Mining Science,* vol. 51, pp. 179–185.

[12] Hegedüs, B., Kékesi, T. (2018): Leaching behavior of the residue from the thermo-mechanical treatment of aluminium melting dross. In: *MultiScience – XXXII. microCAD International Multidisciplinary Scientific Conference, Section B.*, Miskolc, Hungary, 5–6 September, p. 12.

[13] Gasteiger, H. A., Frederic, W. J., Streisel, R. C. (1992): Solubility of aluminosilicates in alkaline solutions and a thermodynamic equilibrium model. *Industrial & Engineering Chemistry Research,* vol. 31, pp. 1183–1190.

Geosciences and Engineering, Vol. 7, No. 10 (2019), pp. 28–38.

GEOPOLYMER COMPOSITES REINFORCED WITH PLASTIC WASTES

KORNIEJENKO K.[1] – MIKUŁA J.[1] – ŁACH M.[1] – MOURE ALASSIO F.[2] – MOREIRA GARMENDÍA L.[2] – DUARTE GUIGOU M.[2]

[1]*Institute of Materials Engineering, Faculty of Mechanical Engineering, Cracow University of Technology*
[2]*Engineering and Technology School, Catholic University of Uruguay*

Abstract: The article analyses the possibilities of using plastic wastes as the reinforcement for geopolymer composites. The mechanical properties of fly-ash based geopolymers reinforced with three different kinds of plastic wastes were investigated. The samples were prepared using sodium promoter and plastic wastes (1% by mass of the composite). The following kinds of waste were used for manufacturing the composites: post-processing waste – basalt fibres with polystyrene, waste from discarded plastic Euro pallets (made from mixed plastic) utilization and mixing of waste polyolefin materials such as polyethylene, polypropylene and other waste packing materials. The empirical part of the research is based on compressive strength tests, flexural strength tests, and macro- and microstructure examination. The results show the different polymer wastes can be utilized in geopolymer composites. The best results for compressive strength, 57.6 MPa, are achieved for the matrix reinforced by post-processing waste (basalt fibers with polystyrene). It is better result than for plane geopolymer – 55.6 MPa. The results for other samples yield also very high values of compressive strength – 56 MPa for composites with waste form plastic pallet utilization and 54.5 MPa for composites with mixing polyolefin materials. The best results for flexural strength are achieved for the matrix without reinforcement – 9.7 MPa. However, the results for other reinforced composites, ranging from 7 to 8.3 MPa, are also very good. Using waste materials it is possible to achieve a composite with good mechanical properties that could be used for different applications in the construction industry.

Keywords: *Geopolymer, Composite, Plastic Waste*

1. INTRODUCTION

The construction industry is a very important field in the global economy as well as in the EU economy. At world level, civil works and building construction consume 60% of the raw materials extracted from the lithosphere and in Europe, the mineral extractions per capita intended for building amount to 4.8 tonnes per inhabitant per year [1]. Innovations in this branch have a strong impact on the sustainable development of Europe's competitiveness. Modern materials in the construction industry should not only improved safety and functionality, but should also have reasonable prices and take into consideration the final product recyclability [2, 3]. In Europe buildings are responsible for more than 40% of the energy consumption and green-

house gas emissions [4, 5]. The main goal of the research was to develop an eco-friendly material for the construction industry using a geopolymer matrix and waste material. The article presents research attempting to determine the possibilities for utilization of plastic waste to create composites based on a geopolymer matrix, especially using mixed waste, which is hard to process.

Nowadays, geopolymers may be one solution to the problem of high CO_2 emissions and other environmental aspects connected with using traditional Portland cement in the construction industry [6–8]. In comparison to the traditional materials, such as concrete, geopolymers have a number of advantages. They are not only eco-friendly but the production of such composites compared to the other cementitious materials is economically more beneficial, including the low energy consumption of their manufacturing [9]. Additional environmental benefits are connected with using production process waste materials: for example fly ashes and mine tailings [10, 11]. At the same time, the obtained materials have better properties than the conventional ones [12, 13] e.g. high initial strength; reduced shrinkage; low thermal conductivity; good fire resistance (up to 1,000 °C); lack of emission of toxic fumes when heated; high level of resistance to a variety of acids and salts; good resistance to abrasion; adherence to new and old concrete, steel, glass and ceramics; lack of corrosion of the steel reinforcement in a geopolymer matrix; high level of adhesion to steel; protection of steel against high residual pH as well as low diffusion rates chloride, high resistance to atmospheric conditions; lower costs; wide availability of the raw materials required for their manufacturing; the possibility of hazardous waste immobilization by trapping wastes in geopolymer composites.

Moreover, the positive environmental influence can be even higher if waste materials are applied to production of these composites. Tests have been performed with both natural and synthetic reinforcement. Among the natural additions, some waste form plant production has been successfully tested, especially waste from abaca [14], coir [15], and coffee grounds [16]. Among the synthetic waste investigations have been carried out on waste form production carbon fibers [17] and glass fibers [18], waste Rockwool [19], waste form used tires [9, 20] and other plastic waste [21, 22].

One of the most problematic wastes for recycling is mixed plastic waste [23, 24]. It is non-biodegradable and takes many years to degrade. The previous investigations made on cementitious materials show that this kind of waste can be successfully applied for replacement for fine aggregate as a substitution for sand in the formulation of concrete [25, 26]. The replacement materials reduce the weight of the final product, which reduces the costs of transport [25] and provides a good approach to reducing the cost and problems posed by disposing of plastics [26]. Further research showed that this kind of additive can also be beneficial for geopolymer concrete [27].

2. MATERIALS AND METHODS

2.1. Materials

The geopolymer matrix was based on fly ash from a CHP plant located in Skawina, Poland. SEM observations show that the fly ash contains spherical aluminosilicate particles. The sieve analysis gives the following values for sizes [28]: > 100 μm – ca. 3%; 71–100 μm – ca. 12%; 63–71 μm – ca. 10%, 56–63 μm – ca. 15% and < 56 μm – ca. 60%. This fly ash is rich in oxides such as SiO_2 (47.81%) and Al_2O_3 (22.80%). High values of SiO_2 and Al_2O_3 are advantageous for geopolymerization. The results of oxygen analysis are shown in *Table 1*. This kind of fly ash is appropriate for geopolymer production because of its physical properties and chemical composition [29].

Table 1

Chemical composition of fly ash, presented in % [28]

loss on ignition	SO_3	chloride (Cl)	CaO	SiO_2 (reactive)	SiO_2	Al_2O_3	Fe_2O_3	SiO_2 + Al_2O_3 + Fe_2O_3	MgO	P_2O_5	Na_2O	K_2O	Na_2Oeq
2.84 ± 0.14	0.95 ± 0.24	0.034 ± 0.010	0.02 ± 0.01	35.86 ± 0.64	47.81	22.80	7.60	78.21 ± 1.28	3.06 ± 0.23	0.0008	1.72	4.62	4.76 ± 0.47

Three different types of reinforcement were applied:

- basalt fibres with polystyrene (FA1),
- waste from discarded plastic Euro pallets (FA2),
- mixed waste polyolefin materials such as polyethylene, polypropylene and other waste packing materials (FA3).

2.2. Samples preparation

The samples were prepared using sodium promoter, fly ash, and sand to create geopolymer matrix. Reinforcement by polymer particles came from different types of waste (1% by mass). The matrix was based on fly ash and fine sand at a ratio of 1 : 1. The process of activation was made by 12M sodium hydroxide solution combined with the sodium silicate solution (liquid glass at a ratio of 1 : 2.5). To manufacture geopolymers, flakes of technical sodium hydroxide were used and an aqueous solution of sodium silicate (R-145) with molar module 2.5 and density of about 1.45 g/cm^3. Tap water was used instead of distilled water. The alkaline solution was prepared by pouring the aqueous solution of sodium silicate over the solid sodium hydroxide. The solution was mixed and left until its temperature became stable and the concentrations equalized, which took about 2 hours. The fly ash, sand, alkaline solution and fibers were mixed about 15 minutes by using a mixing machine (Varimixer Bear) to produce a homogeneous paste. Afterward, the mixture was poured into sets of plastic molds and were heated in the laboratory dryer for 24 h at

75 °C. Then, the samples were removed from the mold and cured under laboratory conditions for 14 days. After this time, the mechanical properties were investigated.

2.3. Methods

Compressive strength tests were carried out according to the methodology described in the standard EN 12390-3 ('Testing hardened concrete. Compressive strength of test specimens'). The tests involved 4 cubic samples: 50 × 50 × 50 mm. A scanning electron microscope (SEM) type JEOL JSM 820 was used for microstructure research. Samples previously broken during compressive or flexural strength tests were used. The samples were covered with a thin layer of gold with JEOL JEE-4X vacuum sputter. The investigations were made at various magnifications (20–100×).

Flexural strength tests were carried out according to the methodology described in the standard EN 12390-5 ('Testing hardened concrete. Flexural strength of test specimens'). The tests involved 2 prismatic samples: 50 × 50 × 150 mm. Tests were performed on a concrete press – MATEST 3000 kN with speed 0.5 MPa/s.

3. RESULTS AND DISCUSSION

3.1. Micro- and macroanalysis

Micro- and macro-observations were carried out on the prepared samples. The particles distribution was evaluated. Macro-observations showed that the composites FA1 as well as the composites FA2 have regular particular distribution by volume and do not tend to create agglomerates. In the composites FA3 the distribution was irregular. The vibration process applied during the manufacture of the specimens probably caused most of particles to rise to the upper surface of the sample *(Figure 1)*. This irregular distribution in the matrix heavily influences the mechanical properties of the composite.

The SEM observations were made for composition reinforced by three different kinds of plastic particles (FA1, FA2 and FA3). The images were made at various magnifications – between 20–100× for each composition. The observation of the microstructure of composites gave preliminary information about the coherency of the reinforcement with the geopolymer matrix.

Figure 2 presents the morphology of the composite with waste: basalt fibers with polystyrene (FA1). The figure shows polystyrene particles and geopolymer matrix. The observation does not show any basalt fibers; they probably dissolved during the production process because of the high molar ratio of the sodium hydroxide solution (12M). The microstructural observation also allows us to notice that the structure is coherent (good adhesion of the polystyrene particles to the matrix).

Figure 1
The irregular distribution of plastic particles in the geopolymer matrix, cross-section through the sample (FA3) after compressive strength test

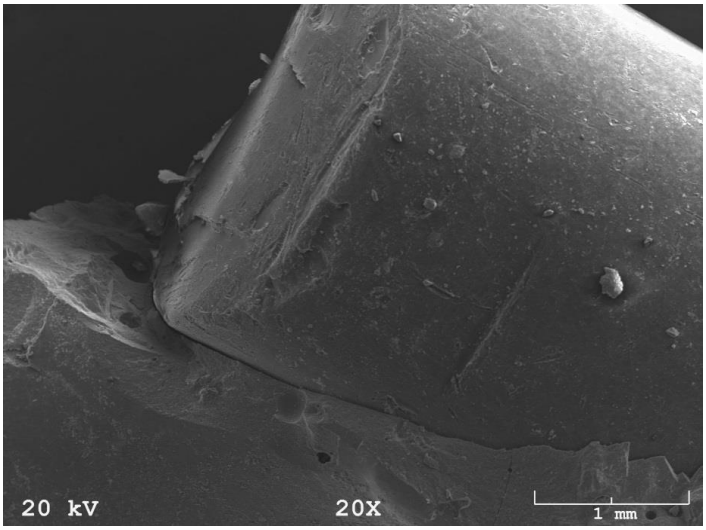

Figure 2
SEM image of composite: geopolymer matrix with basalt fibers with polystyrene (FA1)

The results from the scanning electron microscopy analysis for the composite with waste form waste from discarded plastic Euro pallets (FA2) are shown in *Figure 3*. The figure shows plastic particles and parts of the geopolymer matrix. The observations do not show any problems with particle-matrix coherence.

A SEM image of the composite with additive mixing of waste polyolefin materials such as polyethylene, polypropylene and other waste packing materials (FA3) is presented in *Figure 4*.

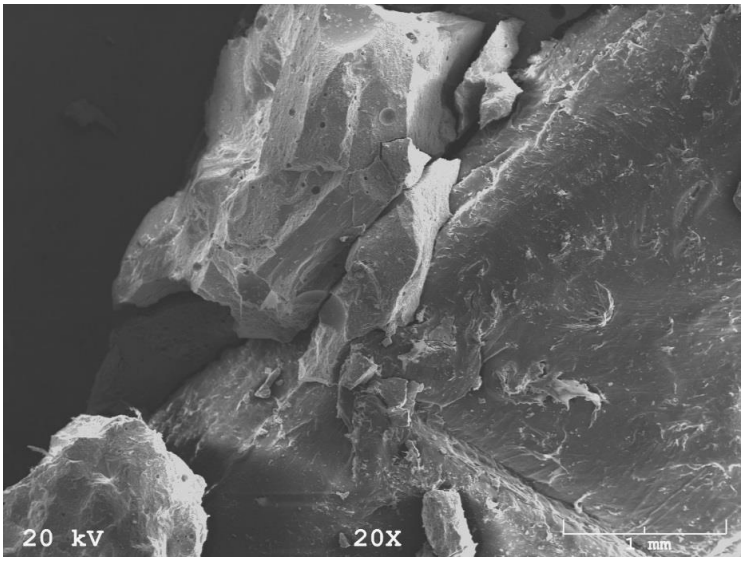

Figure 3
SEM image of composite: geopolymer matrix with form waste plastic pallet utilization (FA2)

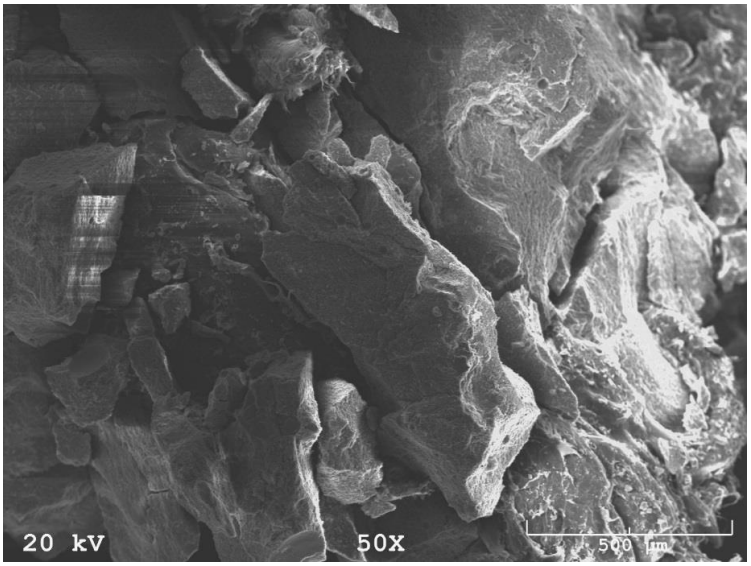

Figure 4
SEM image of composite: geopolymer matrix with mixing of waste polyolefin materials such as polyethylene, polypropylene and other waste packing materials (FA3)

The observations confirm the cohesiveness between particles and matrix. The coherent structure has a positive impact on the mechanical properties of the composites.

3.2. Mechanical properties tests

Results for mechanical properties tests are presented in *Tables 2* and *3*. The results (averaged values) of the compressive strength test are shown in *Table 2*. For comparison results of a non-reinforced specimens (FA0) are also presented.

Table 2

Results of compressive strength tests

Samples	Compressive strength [MPa]	Standard deviation
FA0	55.6	7.7
FA1	57.6	14.2
FA2	56.0	7.7
FA3	54.5	3.1

The best results for compressive strength were achieved for the FA1 at 57.6 MPa, followed by the composite FA2 at 56 MPa. These are better than for the plain geopolymer matrix, which was 55.6 MPa. The results for the composite FA3 are slightly worse than for the plain material – 54.5 MPa. However, it should be noted that the results of compressive strength for different kinds of reinforcements are very similar. The differences are statistically not important.

The results (averaged values) from the flexural strength tests are shown in *Table 3*. The results of the reinforced composites are presented and for comparison the plain (without reinforcement) specimen values are also given.

Table 3

Results of flexural strength tests

Samples	Flexural strength [MPa]	Standard deviation
FA0	9.7	0.9
FA1	8.1	1.4
FA2	8.3	0.2
FA3	7.0	0.1

The best results for flexural strength are achieved for the matrix without reinforcement – 9.7 MPa. However, the results for other reinforced composites are also very good. The differences between the plain matrix and composites FA1 (8.1 MPa), and composites FA2 (8.3 MPa) are statistically not important. The composition FA3 has worse properties than the plain matrix, with 7.0 MPa. However, the values are still acceptable taking under consideration the applications of this material in civil engineering.

4. CONCLUSIONS

Geopolymer composites reinforced with various types of waste have been produced and characterized. The samples were prepared using sodium promoter and three various types of waste additives (1% by mass of the composite): basalt fibres with polystyrene (FA1), waste form plastic pallet utilization (FA2), and mixing of waste polyolefin materials such as polyethylene, polypropylene and other waste packing materials (FA3). The matrix was geopolymer cement (fly ash and sand in ratio 1 : 1).

The observation of macrostructure gives the information about particles distributions. In the case of additive basalt fibres with polystyrene (FA1) and waste form plastic pallet utilization (FA2) the particle distribution was regular. For the composites reinforced by mixing of waste polyolefin materials such as polyethylene, polypropylene and other waste packing materials (FA3) the particles accumulated in the upper part of the composite. The microstructure analysis of composites gave preliminary information about the coherency of the reinforcements with the geopolymer matrix. The results of compressive strength tests for different kinds of reinforcements as well as the plain matrix are very similar. The differences are statistically not important. The results of flexural strength tests show that the differences between plain matrix and composites with basalt fibres with polystyrene (FA1) and composites with waste form plastic pallet utilization (FA2) are statistically not important. The composition with mixing of waste polyolefin (FA3) has slightly worse properties; however, they are still acceptable taking under consideration civil engineering applications of this material.

This study demonstrates that it is possible to produce composites of reasonable properties from industrial wastes (fly ash and waste polymers). Although the results show the addition of different waste polymer materials to a geopolymer matrix do not increase significantly the mechanical properties of the composites, it still can be promising way of waste material utilization. The investigated materials work in the composites as a filler, not as a reinforcement. Based on these kinds of waste materials it is possible to obtain a composite with good mechanical properties that could be used for different applications. Additionally, using the plastic waste has a positive impact on environment. Thus, the designed composites have the potential to be used as new eco-friendly material, e.g. in construction industry. The industrial application in this area requires further research for features such as water absorption, durability, corrosion resistance, and cost-effectiveness.

ACKNOWLEDGEMENTS

This work was supported by the ERANet-LAC 2nd Joint Call (http://www.eranet-lac.eu) and funded by National Centre for Research and Development, Poland, as well as the National Research and Innovation Agency (ANII), Uruguay, under the grant: “Development of eco-friendly composite materials based on geopolymer matrix and reinforced with waste fibers”.

REFERENCES

[1] Bribián, I. Z. et al. (2011): Life cycle assessment of building materials: Comparative analysis of energy and environmental impacts and evaluation of the eco-efficiency improvement potential. *Building and Environment*, 46, pp. 1133–1140. Doi: 10.1016/j.buildenv.2010.12.002.

[2] Arulrajah, A. et al. (2017): Recycled plastic granules and demolition wastes as construction materials: Resilient moduli and strength characteristics. *Construction and Building Materials*, 147, pp. 639–47. Doi: https://doi.org/10.1016/j.conbuildmat.2017.04.178.

[3] Iucolano, F. et al. (2013): Recycled plastic aggregate in mortars composition: Effect on physical and mechanical properties. *Materials & Design*, 52, pp. 916–922. Doi: https://doi.org/10.1016/j.matdes.2013.06.025.

[4] Crawley D. B. (2008): Estimating the impacts of climate change and urbanization on building performance. *Journal of Building Performance Simulation*, 1, pp. 91–115. Doi: https://doi.org/10.1080/19401490802182079.

[5] Pacheco-Torgal, F. (2014): Eco-efficient construction and building materials research under the EU Framework Programme Horizon 2020. *Construction and Building Materials*, 51, pp. 151–62. Doi: https://doi.org/10.1016/j.conbuildmat.2013.10.058.

[6] Celik, A. et al. (2018): High-temperature behavior and mechanical characteristics of boron waste additive metakaolin based geopolymer composites reinforced with synthetic fibers. *Construction and Building Materials*, 187, pp. 1190–203. Doi: https://doi.org/10.1016/j.conbuildmat.2018.08.062.

[7] Nazari, A. (2013): Compressive strength of geopolymers produced by ordinary Portland cement: Application of genetic programming for design. *Materials and Design*, 43, pp. 356–366. Doi: https://doi.org/10.1016/j.matdes.2012.07.012.

[8] Palomo, A. et al. (2014): A review on alkaline activation: new analytical perspectives. *Materials de Construccion*, 64 (315), p. 22. Doi: http://dx.doi.org/10.3989/mc.2014.00314.

[9] Łach, M. et al. (2017): The possibilities of use granulates made from tires as an additive to geopolymer concretes. In: Hager I. (ed.): *Energy Efficient, Sustainable Building Materials and Products*. Cracow, Wydawnictwo Politechniki Krakowskiej, pp. 63–78.

[10] Sedira, N. et al. (2017): A Review on Mineral Waste for Chemical-Activated Binders: Mineralogical and Chemical Characteristics. *Mining Science*, 24, pp. 29–58. Doi: 10.5277/msc172402.

[11] Mierzwiński, D. et al. (2018): Stabilization of ash and slag from combustion of medical waste in the geopolymers matrix. *E3S Web of Conferences*, 44, p. 8. Doi: 10.1051/e3sconf/20184400110.

[12] Cheng, T. W. et al. (2011): The heavy metal adsorption characteristics on metakaolin-based geopolymer. *Applied Clay Science*, 56, pp. 90–96. Doi: https://doi.org/10.1016/j.clay.2011.11.027.

[13] Ogundiran, M. B. et al. (2013): Immobilisation of lead smelting slag within spent aluminate-fly ash based geopolymers. *Journal of Hazardous Materials*, 248–249 (1), pp. 29–36. Doi: https://doi.org/10.1016/j.jhazmat.2012.12.040.

[14] Malenab, R. A. J. et al. (2017): Chemical Treatment of Waste Abaca for Natural Fiber-Reinforced Geopolymer Composite. *Materials*, 10, pp. 579–98. Doi: 10.3390/ma10060579.

[15] Palanisamya, P., Suresh Kumar, P. (2018): Effect of Molarity in Geopolymer Earth Brick Reinforced with Fibrous Coir Wastes Using Sandy Soil and Quarry Dust as Fine Aggregate. (Case Study). *Case Studies in Construction Materials*, 8, pp. 347–358. Doi: https://doi.org/10.1016/j.cscm.2018.01.009.

[16] Mierzwiński, D. et al. (2018): Effect of Coffee Grounds Addition on Efflorescence in Fly Ash-based Geopolymer. IOP Conference Series: *Materials Science and Engineering*, 416 (2018) 012035, p. 7. Doi: 10.1088/1757-899X/416/1/012035.

[17] Luna-Galiano, Y. et al. (2018): Carbon fiber waste incorporation in blast furnace slag geopolymers composites. *Materials Letters*, 233, pp. 1–3. Doi: https://doi.org/10.1016/j.matlet.2018.08.099.

[18] Novais, R. M. et al. (2017): Effective mechanical reinforcement of inorganic polymers using glass fibre waste. *Journal of Cleaner Production*, 166, pp. 343–349. Doi: https://doi.org/10.1016/j.jclepro.2017.07.242.

[19] Kinnunen, P. et al. (2017): Rockwool waste in fly ash geopolymer composites. *Journal of Material Cycles and Waste Management*, 19, pp. 1220–1227. Doi: 10.1007/s10163-016-0514-z.

[20] Mucsi, G. et al. (2018): Fiber reinforced geopolymer from synergetic utilization of fly ash and waste tire. *Journal of Cleaner Production*, 178, pp. 429–40. Doi: https://doi.org/10.1016/j.jclepro.2018.01.018.

[21] Mucsi G. et al. (2017): Development of polystyrene-geopolymer composite for thermal insulating material and its properties with special regards to flame resistance. IOP Conference Series: *Materials Science and Engineering*, 251 (2017) 012079, p. 8. Doi: 10.1088/1757-899X/251/1/012079.

[22] Vishwakarma, V., Ramachandran, D. (2018): Green Concrete mix using solid waste and nanoparticles as alternatives – A review. *Construction and*

Building Materials, 162, pp. 96–103. Doi: https://doi.org/10.1016/j.conbuildmat.2017.11.174.

[23] Singh, N.: Recycling of plastic solid waste (2017): A state of art review and future applications. *Composites Part B*, 115, pp. 409–422. Doi: https://doi.org/10.1016/j.compositesb.2016.09.013.

[24] Wang R, Xu, Z. (2014): Recycling of non-metallic fractions from waste electrical and electronic equipment (WEEE): A review. *Waste Management*, 34 (8), pp. 1455–1469. Doi: https://doi.org/10.1016/j.wasman.2014.03.004.

[25] Ismail Z. Z., Al-Hashmi E. A. (2008): Use of waste plastic in concrete mixture as aggregate replacement. *Waste Management*, 28 (11), pp. 2041–2047. Doi: https://doi.org/10.1016/j.wasman.2007.08.023.

[26] Ghernouti Y. et al. (2014): Use of recycled plastic bag waste in the concrete. *Journal of International Scientific Publications*: *Materials, Methods and Technologies*, 8, pp. 480–487.

[27] Colangelo F. et al. (2013): Experimental and Numerical Analysis of Thermal and Hygrometric Characteristics of Building Structures Employing Recycled Plastic Aggregates and Geopolymer Concrete. *Energies*, 6, pp. 6077–6101; Doi:10.3390/en6116077.

[28] Korniejenko, K. (2018): Geopolymers for increasing durability for marine infrastructure. *Durability and Sustainability of Concrete Structures (DSCS-2018): proceedings 2nd International Workshop*, June 6–7, 2018 Moscow, Russia.

[29] Korniejenko, K. et al. (2018): The mechanical properties of flax and hemp fibres reinforced geopolymer composites. IOP Conference Series: *Materials Science and Engineering*, 379 (2018) 012023, p. 9. Doi:10.1088/1757-899X/379/1/012023.

Geosciences and Engineering, Vol. 7, No. 10 (2019), pp. 39–47.

ELECTROCHEMICAL OXIDATION OF REACTIVE BLACK 5 AZO DYE IN CHLORIDE MEDIA

D. JÁGER[1] – D. KUPKA[1] – M. VÁCLAVÍKOVÁ[1] – L. IVANIČOVÁ[1] – G. GALLIOS[2]

[1]*Institute of Geotechnics, Slovak Academy of Sciences, Watsonova 45, 040 01, Košice, Slovakia, e-mail: jager@saske.sk*
[2]*Lab. Chemical & Environmental Technology, School of Chemistry, Aristotle University of Thessaloniki, University Campus, 54124, Thessaloniki, Greece*

Abstract: The breakdown of commercial grade Reactive Black 5 (RB5) azo dye by electrochemical treatment was studied using a dimensionally stable anode and stainless steel cathodes as electrode materials, with NaCl as supporting electrolyte. The compounds present in the commercial grade RB5 azo dye and the products of its electrochemical degradation were separated using ion-pairing high performance liquid chromatography (HPLC) on reversed phase. The separated species were detected by diode array detector and identified utilizing high resolution mass spectrometry (HRMS) and tandem mass spectrometry (MS/MS). A suitable ion-pairing reversed phase HPLC-MS method with electrospray ionization for identification and quantification of the components was developed. The accurate mass of the parent and fragment ions was used in the determination of the empirical formulas of the components and degradation products. Structural formulas of degradation products were proposed using this information and principles of organic chemistry and electrochemistry.

Keywords: *Azo dyes, Decolorization, Electrochemical oxidation, HPLC-MS analysis, Water treatment*

1. INTRODUCTION

Reactive Black 5 (RB5) is one of the most common dyes used in textile industries. Reactive dyes contain functional groups that form a covalent bond with the fiber, achieving extremely high wash fastness properties [1]. Most reactive dyes fall in the category of azo dyes. Azo dyes are aromatic compounds with one or more azo functional groups *(*see *Figure 1)*. Azo dyes constitute the largest class of synthetic dyes [2]. A large amount of these compounds is lost during the dyeing process, resulting in azo dye contaminated effluents. Dyes are generally recalcitrant to biodegradation [3]. Different techniques of dye removal from waste effluents have been developed. Conventional processes applicable for this purpose include adsorption, coagulation, membrane filtration and ion exchange [4]. In fact, these approaches only transfer the contaminants from wastewater to solid wastes that have to be disposed of.

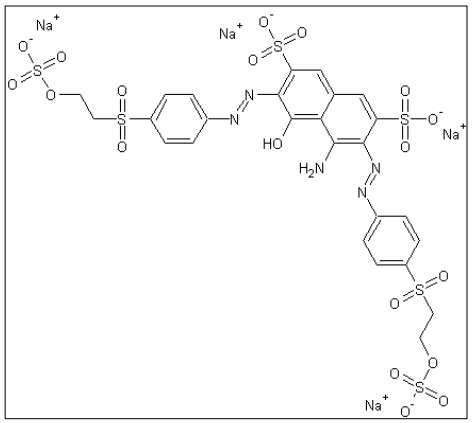

Figure 1
Structural formula of the RB5 molecule

Electrochemical oxidation is a modern technology for the treatment of various wastewaters [5–9]. Oxidants are produced during the process *in situ*, either directly at the electrode surface or indirectly from chemicals that are present in the treated water. The electrode material strongly influences both the selectivity and the efficiency of the process [10, 11]. Titanium based mixed metal oxide anodes have been widely applied in wastewater treatment due to their structural and chemical stability over a wide range of electrical potentials. In the presence of chlorides the electrochemical treatment can be carried out at lower potentials compared to those required for the direct anodic oxidation [12]. A significant disadvantage of electrolysis in chloride media is the formation of chlorinated organics. Indeed, chlorinated organic compounds are detected during electro-chlorination, but in most cases they are degraded during further electrolysis [13].

The exact nature of the electrochemical and chemical reactions that take place during electrolytic treatment in chloride media is complex and not entirely known [11]. The degradation mechanism of RB5 during electrolysis with NaCl as supporting electrolyte has not been fully described so far. The identification of degradation products is important in order to ensure that the treated wastewater is not toxic [14]. The objective of this study was to identify the products of electrochemical degradation of RB5 dye using HPLC-MS. The accurate mass of the parent and fragment ions was used in the determination of the empirical formulas of the components. Structural formulas were suggested using the mass spectra.

2. MATERIALS AND METHODS

2.1. The electrochemical system

Electrolysis of RB5 solutions was performed under galvanostatic conditions in an undivided electrochemical cell. Titanium-based dimensionally stable anode DSA® coated with mixed oxides of $RuO_2/IrO_2/TiO_2$ was surrounded by two stainless steel cathodes. The geometric area of the anode was 73 mm × 100 mm. With an applied current of 1.5 A, the calculated current density was approx. 100 A m^{-2}. The corresponding electric potential difference was 17 V at the start of the electrolysis. The anodic potential was not measured. Electrolysis was carried out at room temperature in a batch mode. The solution was mixed by up-flow gas lifting *(*see *Figure 2)*. The reaction cell was gas tight sealed by the lid with openings for excurrent gas analysis and liquid sampling. A synthetic aqueous solution of RB5 was prepared by dissolving 300 mg L^{-1} commercial grade Reactive Black 5 in 8 mM NaCl electrolyte.

Colour disappearance during chemical and electrochemical reaction was measured at 597 nm by UV-VIS spectrometer Helios gamma (Thermo Electron Corporations).

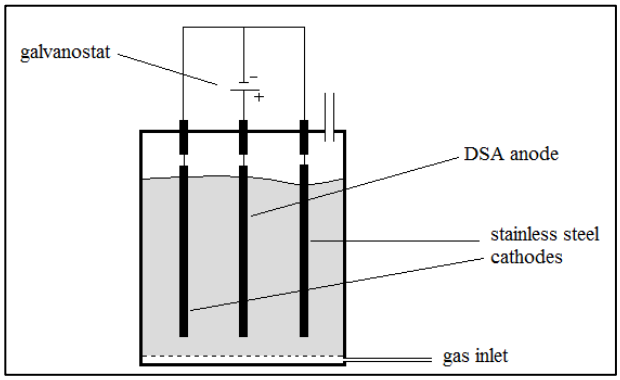

Figure 2
The configuration
of the electrolytic cell

2.2. Solvents and reagents for HPLC-MS

Ultrapure water (18.2 MΩ), analytical grade sodium chloride, HPLC and LC-MS grade reagents and solvents (methanol, triethylamine and acetic acid) were used for the eluents preparation. The solvents were degassed in ultrasonic bath. Triethylammonium acetate (TEAA) was prepared by mixing equimolar amounts of triethylamine and acetic acid.

2.3. Identification of the organic species using HPLC-MS

Samples of the electrolyte were withdrawn at regular intervals during the electrolysis for chromatographic and mass spectrometric analyses. The samples were filtered using 0.22 mm PTFE syringe filters before analysis. The HPLC-MS analyses of the reaction products were performed using a DIONEX UltiMate 3,000 HPLC system linked with micrOTOF-Q II quadrupole-time of flight hybrid mass spectrometer (Bruker Daltonics). The separation of the compounds was performed by ion-pairing reversed-phase HPLC using Acclaim™ 120-3 C18, 150 mm × 2.1 mm column (Thermo Scientific). Multistep gradient elution was carried out using a mixture of water (A) and methanol (B) with 2.5 mM TEAA, cationic ion-pairing reagent. Flow rate was adjusted at 250 μL min^{-1}. The mobile phase composition during the gradient elution was changed as follows: 0–30 min 10→70% B, 30–40 min 70→10% B, 40–45 min 10% B. The column temperature was set at 40 °C. The injected sample volume was 50 μL. The HPLC eluate was further analysed by MS. The mass spectrometer was equipped with an electrospray ion source working in negative mode. The sum formulas were determined and possible structures of the species were suggested using the accurate masses of the molecular and fragment ions. The mass deviations (experimental vs. theoretical) were below 5 ppm for every m/z.

3. RESULTS AND DISCUSSION

3.1. Reactive Black 5

Commercial dyestuffs that are placed on the market are not pure compounds. They usually contain other additives that improve the product's application properties. A number of impurities are present, such as precursors of the synthesis, products of partial azo-coupling, and products of hydrolysis, as well as compounds formed by elimination reactions of the main RB5 component. The impurities are formed during dye manufacturing as well as during storage. Several peaks appeared on the UV chromatogram of the dye solution *(Figure 3)*.The compounds that corresponds to the three major peaks are listed in *Table 1*. The m/z ratios of the detected fragment and adduct ions are also indicated in the table.

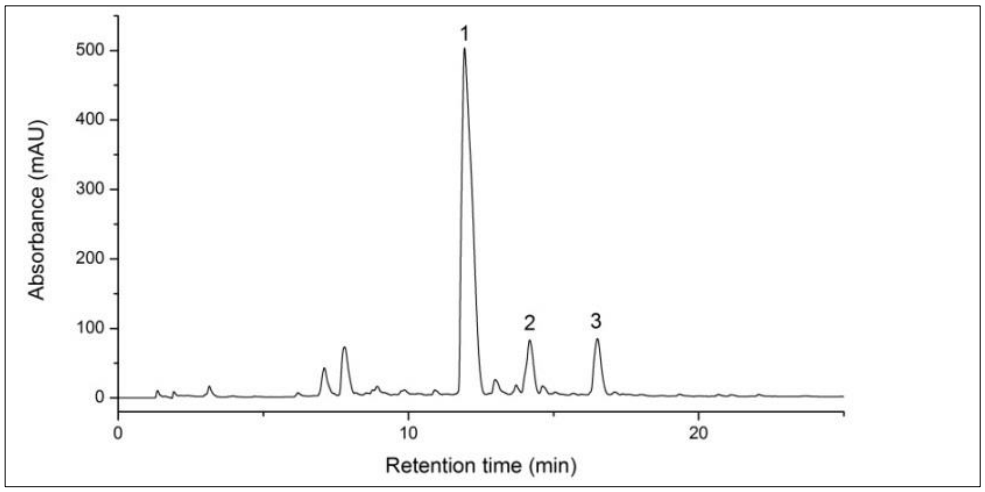

Figure 3
UV chromatogram at 254 nm
from the HPLC-DAD analysis of the dye solution

The typical ESI mass spectra of sulfated dyes are complex, with many fragment ions being present in the first-order spectra [15–17]. The mass spectrum of polysulfated dyes, like RB5, usually shows extensive fragmentation with typical neutral losses of H_2O, SO_2, SO_3 and sulfuric acid, and reduced relative abundance of single charged $[M\text{-}H]^-$ pseudo-molecular ions [16-18]. Multiple-charged quasi-molecular ions are present in the ESI mass spectra of polysulfated dyes, which are usually more intensive than the single-charged deprotonated pseudo-molecular ion. Adducts of the species with triethylammonium and sodium cations are also present in the spectra.

Table 1

The suggested structural formula of the compounds that correspond to the 3 major peaks of the UV-chromatogram

Retention time (min)	**m/z (monoisotopic) of the detected molecular ion(s) and charge**	**m/z (monoisotopic) of the detected fragment and adduct ion(s) and charge**	**Empirical formula and the suggested structure of the neutral compound**
12.9	450.465 $[M\text{-}2H]^{2-}$ 299.976 $[M\text{-}3H]^{3-}$	401.483 $[M\text{-}2H\text{-}H_2SO_4]^{2-}$ 461.458 $[M\text{-}3H\text{+}Na]^{2-}$ 501.027 $[M\text{-}2H\text{+}TEA]^{2-}$ 410.489 $[M\text{-}2H\text{-}SO_3]^{2-}$	$C_{26}H_{25}N_5O_{19}S_6$ 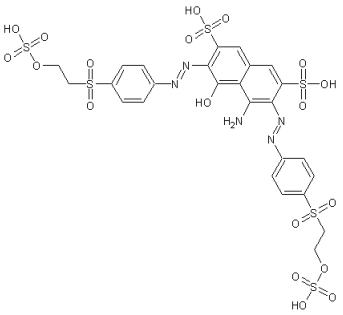 RB5
14.6	821.984 $[M\text{-}H]^{-}$ 410.48 $[M\text{-}2H]^{2-}$	843.966 $[M\text{-}H\text{+}Na]^{-}$ 923.102 $[M\text{-}H\text{+}TEA]^{-}$ 421.479 $[M\text{-}3H\text{+}Na]^{2-}$ 370.510 $[M\text{-}2H\text{-}SO_3]^{2-}$	$C_{26}H_{25}N_5O_{16}S_5$ 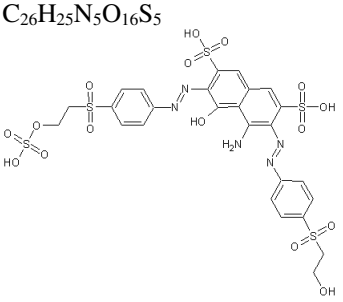 One of the 2 possible isomers
16.4	803.972 $[M\text{-}H]^{-}$ 401.482 $[M\text{-}2H]^{2-}$	825.951 $[M\text{-}2H\text{+}Na]^{-}$ 905.092 $[M\text{-}H\text{+}TEA]^{-}$ 412.473 $[M\text{-}3H\text{+}Na]^{2-}$ 361.501 $[M\text{-}2H\text{-}SO_3]^{2-}$	$C_{26}H_{23}N_5O_{15}S_5$ 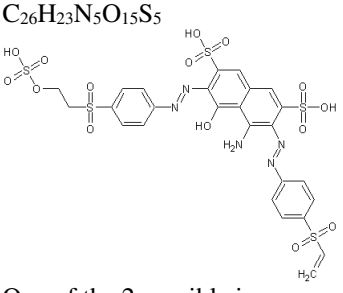 One of the 2 possible isomers

M – neutral molecule
TEA –triethylamine

3.2. Electrochemical degradation

The variability of compounds that are already present in the initial solution makes the identification of the species formed during electrolytic treatment more complicated. Two concurrent processes take place during the electrolysis of azo dyes: heterogeneous direct oxidation/reduction on the surface of electrodes and indirect homogeneous reactions, which occur in the bulk solution. During electrolysis with DSA anode in chloride media the decolourization of the RB5 solution was rapid *(*see *Figure 4)*. After 15 min of electrolytic treatment the concentration of the dye decreased under the HPLC-MS detection limit. The decolourization is caused by the changes in the chemical structure of the dye molecule: either by oxidation of the functionalities or by the interruption of the conjugated system of double bonds in the structure. Despite the complete colour removal, azo compounds were still present among the degradation products with molecular weight between 400–600 Da *(*see *Table 2).*

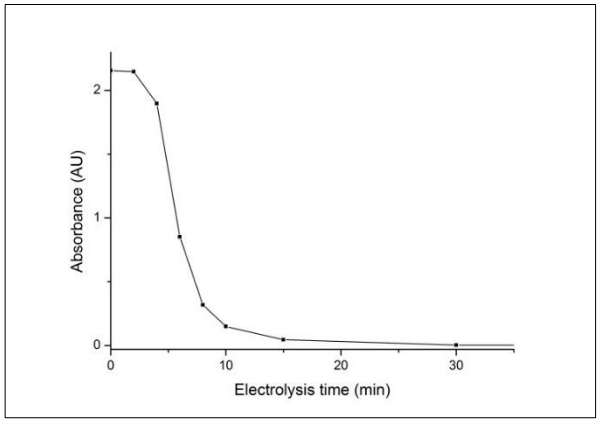

Figure 4
Absorbance of the solution at 597 nm during electrolysis

The chemical oxygen demand (COD) of the solution decreased by 33% during electrolysis from the initial value of 180 mg L^{-1}. The production of CO_2 and the decrease of total organic carbon (TOC) of the solution is negligible, meaning that the anode material is not able to completely incinerate the organic matter in the solution to carbon dioxide. The parent molecules were degraded/ transformed to highly polar and smaller molecules like formic acid, acetic acid and oxalic acid. These polar products showed the least retention on a reversed stationary phase. Some halogenated organic products are present during the experiment, e.g. trichloroacetic acid, dichloromethanesufonic acid *(*see *Table 2)*. The chlorinated products are produced by the reaction with active chlorine species that are generated in the solution during electrolysis, such as Cl_2 and hypochlorous acid. These chloroderivatives were gradually degraded with extended time of electrochemical treatment. The exact mechanisms of the formation of the small polar compounds are in fact complex. No opening and mineralization of the aromatic rings was observed during the experiments. The small aliphatic products were formed from the aliphatic parts of the RB5 molecule. Nitrates and sulfates were identified after treatment. The nitrates are oxidation products of the azo and amine functionalities.

Table 2

Selected azo compounds and chlorinated by-products that were identified by HPLC-MS/MS in the solution during electrochemical treatment

Retention time (min)	**m/z (monoisotopic) of the detected molecular ion(s) and charge**	**m/z (monoisotopic) of the detected fragment and adduct ion(s) and charge**	**Empirical formula and the suggested structure of the neutral compound**
19.7	351.489 $[M-2H]^{2-}$ 703.992 $[M-H]^{-}$		$C_{26}H_{19}N_5O_{11}S_4$ 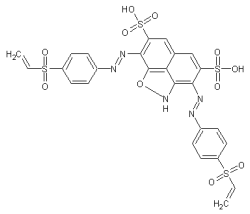
12.4	822.922 $[M-H]^{-}$ 410.956 $[M-2H]^{2-}$	924.036 $[M-H+TEA]^{-}$ 421.947 $[M-3H+Na]^{2-}$ 370.976 $[M-2H-SO_3]^{2-}$	$C_{26}H_{21}ClN_4O_{15}S_5$ 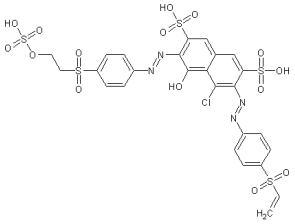 One of the possible isomers
13.8	298.948 $[M-H]^{-}$		$C_8H_9ClO_6S_2$ 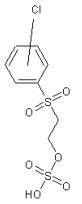
5.4	160.898 $[M-H]^{-}$	116.906 $[M-H-CO_2]^{-}$	$C_2HCl_3O_2$ 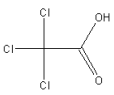
2.6	162.903 $[M-H]^{-}$		$CH_2Cl_2O_3S$ 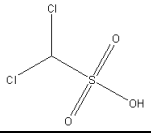

4. CONCLUSIONS

Electrochemical oxidation using DSA anode was employed to treat a synthetic solution of RB5 azo dye. Complete colour disappearance was achieved within 15 min of the electrochemical treatment. Despite decolourization the azo compounds were still detected in the solution, but their quantity was considerably reduced with increasing time of electrolysis. More than 40 degradation by-products, including chlorinated compounds, have been proposed by the HPLC-MS/MS method. In order to identify all compounds with high accuracy and to distinguish structural isomers, different analytical techniques such as ^{1}H and/or ^{13}C nuclear magnetic resonance are required. The proposed chemical formulas of identified species could serve as a starting point for the study of toxicity of treated wastewaters. Measuring of the absorbance and chemical oxygen demand of these solutions after treatment is not adequate for toxicity assessment of these solutions.

ACKNOWLEDGEMENTS

This work has been supported by the Marie Curie Programme FP7-People-2013-IAAP-WaSClean project No. 612250, the Slovak Grant Agency VEGA project No. 2/0142/19, ERDF project No. ITMS 26220120064-Centre of Excellence for Integrated Research of the Earth's Geosphere, Slovak R&D Agency project No APVV-10-0252-WATRIP, as well as the Greek national support project No. 40124, and an R&D support project (MVTS) of the Slovak Academy of Sciences.

REFERENCES

[1] Tappe, H. et al. (2000): Reactive Dyes. In: *Ullmann's Encyclopedia of Industrial Chemistry*. Wiley-VCH Verlag GmbH & Co. KGaA, Weinheim, Germany.

[2] Hunger, K., Mischke, P., Rieper, W. (2000): Azo Dyes, 1. General. In: *Ullmann's Encyclopedia of Industrial Chemistry*. Wiley-VCH Verlag GmbH & Co. KGaA, Weinheim, Germany.

[3] Pagga, U., Brown, D. (1986): The degradation of dyestuffs: Part II Behaviour of dyestuffs in aerobic biodegradation tests. *Chemosphere*, 15 (4), pp. 479–491.

[4] Forgacs, E., Cserháti, T., Oros, G. (2004): Removal of synthetic dyes from wastewaters: a review. *Environ. Int.,* 30 (7), pp. 953–971.

[5] Sirés, I. et al. (2014): Electrochemical advanced oxidation processes: today and tomorrow. A review. *Environmental Science and Pollution Research*, 21 (14), pp. 8336–8367.

[6] Brillas, E., Martínez-Huitle, C. A. (2015): Decontamination of wastewaters containing synthetic organic dyes by electrochemical methods. An updated review. *Applied Catalysis B: Environmental*, 166–167, pp. 603–643.

[7] Martínez-Huitle, C. A. et al. (2015): Single and Coupled Electrochemical Processes and Reactors for the Abatement of Organic Water Pollutants: A Critical Review. *Chemical Reviews*, 115 (24), pp. 13362–13407.

[8] Särkkä, H., Bhatnagar, A., Sillanpää, M. (2015): Recent developments of electro-oxidation in water treatment. A review. *Journal of Electroanalytical Chemistry*, 754, pp. 46–56.

[9] Moreira, F. C. et al. (2017): Electrochemical advanced oxidation processes: A review on their application to synthetic and real wastewaters. *Applied Catalysis B: Environmental*, 202, pp. 217–261.

[10] Christos, C. et al. (2008): Advanced oxidation processes for water treatment: advances and trends for R&D. *Journal of Chemical Technology & Biotechnology*, 83 (6), pp. 769–776.

[11] Panizza, M., Cerisola, G. (2009): Direct And Mediated Anodic Oxidation of Organic Pollutants. *Chemical Reviews*, 109 (12), pp. 6541–6569.

[12] Bonfatti, F. et al. (2000): Electrochemical Incineration of Glucose as a Model Organic Substrate. II. Role of Active Chlorine Mediation. *Journal of The Electrochemical Society*, 147 (2), pp. 592–596.

[13] Fóti, G. et al. (1999): Oxidation of Organics by Intermediates of Water Discharge on IrO2 and Synthetic Diamond Anodes. *Electrochemical and Solid-State Letters*, 2 (5), pp. 228–230.

[14] Madsen, H. T., Søgaard, E. G., Muff, J. (2014): Study of degradation intermediates formed during electrochemical oxidation of pesticide residue 2,6-dichlorobenzamide (BAM) at boron doped diamond (BDD) and platinum–iridium anodes. *Chemosphere*, 109, pp. 84–91.

[15] Ansorgová, D., Holčapek, M. Jandera, P. (2003): Ion-pairing high-performance liquid chromatography-mass spectrometry of impurities and reduction products of sulphonated azodyes. *Journal of Separation Science*, 26 (11), pp. 1017–1027.

[16] Sakalis, A. et al. (2004): Analysis of sulphonated azodyes and their degradation products in aqueous solutions treated with a new electrochemical method. *International Journal of Environmental Analytical Chemistry*, 84 (11), pp. 875–888.

[17] Holčapek, M., Volná, K., Vaněrková, D. (2007): Effects of functional groups on the fragmentation of dyes in electrospray and atmospheric pressure chemical ionization mass spectra. *Dyes and Pigments*, 75 (1), pp. 156–165.

[18] Vaněrková, D. et al. (2006): Analysis of electrochemical degradation products of sulphonated azo dyes using high-performance liquid chromatography/ tandem mass spectrometry. Rapid Communications in Mass Spectrometry, 20 (19), pp. 2807–2815.

Geosciences and Engineering, Vol. 7, No. 10 (2019), pp. 48–59.

OPPORTUNITIES AND LIMITATIONS OF SOLAR ENERGY PROJECTS FOR TERRITORIAL COMMUNITIES OF THE CARPATHIAN REGION OF UKRAINE

OLEG MANDRYK[1] – LIUDMYLA ARKHYPOVA[2] – OLENA POBIGUN[2] – NATALIIA LATSYK[1]

[1]Ivano-Frankivsk National Technical University of Oil and Gas, Institute of Natural Sciences and Tourism, Department of Ecology, Ivano-Frankivsk, Ukraine
[2]Ivano-Frankivsk National Technical University of Oil and Gas, Institute of Natural Sciences and Tourism, Department of Tourism, Ivano-Frankivsk, Ukraine
E-mail: konsevich@ukr.net, antoniuknataliia@gmail.com
Institute of Natural Sciences and Tourism, Ivano-Frankivsk National Technical University of Oil and Gas: 76018, 15 Karpatska Street, Ivano-Frankivsk, Ukraine

Abstract: The use of renewable energy in sustainable tourism development of the region is grounded in the paper. There are three stages of selecting areas for projects of renewable energy sources: selection of potentially suitable areas, consideration of exclusion criteria, and the detailed assessment of potential sites or areas. The factors of impact on spatial constraints and opportunities for building wind, solar and small hydropower plants on the parameters of sustainable tourism development in the Carpathian region were determined. The most common factors are the appropriate wind, solar, and hydrological resources, topographical conditions and existing obstacles, accessibility of terrain, infrastructure, availability of points of joining the network, the quality and composition of soil incorporation of residential areas, open areas, slopes, environmental constraints, analysis land use, and the presence of protected areas and landscapes.The paper introduces the example of site selection for a solar power plant, considering also aspects related to sustainable tourism.

Keywords: *sustainable development, sustainable tourism development, renewable energy, landscape and spatial constraints*

1. INTRODUCTION

Sustainable development meets present day needs and guarantees the same opportunity to future generations. The following interrelated components should be considered with sustainable development: social, economic, environmental and political development. According to the definition developed by the World Tourism Organization (WTO) in 1996, modified in 2004, "sustainable tourism" is the concept of visiting somewhere as a tourist and trying to make a positive impact on the environment, society, and economy. The development of sustainable tourism is seen as a process that, in addition to meeting the needs of tourists and places that receive them, maintains and develops opportunities for the future. According to this definition,

sustainable tourism development considering the situation in the country regarding energy and environmental impact of traditional energy sources, should serve the interests of tourists in the economy and society, take into account the ecological environment, and take measures for its preservation.

The Carpathian region has great potential; the wealth of its natural resources is one of the main reasons tourists travel, and it has all the preconditions for sustainable tourism and recreation development. The use of renewable energy sources (RES), which have recently gained popularity because of the individual economic and political factors prevailing in the country, fully meets the criteria of modern energy ecological tourism development in the region.

The rationality of usage of renewable energy sources was based on work by Plachkova et al. [1], Kudria et al. [2], and Adamenko et al. [3], while methods for increasing the efficiency of the development of alternative and renewable energy sources were considered by Bevz et al. [4] and other scholars and researchers. Among the issues raised by scientists is the question of implementation problems of renewable energy projects and the project realization. But for the future there is an issue of rational argumentation for selection of locations of projects considering also renewable energy sources, such as taking into account factors that need to be considered when choosing such areas, given the parameters of sustainable development in tourism [5].

This paper gives an overview of the process for selecting sites for installing renewable energy facilities. It describes the various aspects considered for wind power, solar power and hydropower plant, with special attention to issues related to sustainable tourism. Then it focuses on possibilities of solar power in relation to infrastructure of the tourism industry.

2. SITE SELECTION FOR RENEWABLE ENERGY PROJECTS

During development phase and implementation of projects of renewable power sources, the essential component is the site finding, which consists of three stages:

- Selection of potentially suitable areas;
- Consideration of the exclusion criteria;
- Detailed assessment of potential sites or areas.

For all projects in which renewable power sources are used, the project will have many potential overall impacts on the landscape, biodiversity and the local population, which should be considered when selecting a suitable site for the project. These general potential impacts may include [6]:

- negative impacts of new energy-generated construction and ancillary facilities such as transmission lines and access roads on the quality of the landscape, environment and aesthetic appearance;
- loss of habitat, habitat fragmentation and simplifying of the ecosystem caused by the influence of site development, and related to potential adverse impacts on the fauna and flora that exist in this natural environment;

- changes in land use and the formation of business struggle because of valued land use (e.g., land being withdrawn from agricultural production);
- impacts on protected areas or sensitive areas and objects of cultural heritage or archeological monuments;
- impacts on local infrastructure facilities and privately owned property.

2.1. Site selection for wind power stations and farms

Finding a suitable site for a wind power station is essential for the success and economic viability of the project. The main aim in site finding is to determine potential wind regions that are also characterized by other parameters which are necessary for wind energy projects implementation. The project developer may be interested only in those areas that are at his disposal or within a selected district or municipality.

At the first stage, the potential sites for wind power are determined by taking into account the wind resources at the height of the hub. This process covers quite a large area (e.g., district or territory which is served by public utility) to determine areas with necessary wind resources on the basis of information which is contained in sources such as maps of wind resources, satellite wind data, time series of design winds, wind data from airport, topography and other indicators.

It is necessary to take into account following restrictions which are related to the site finding. The main factors to be taken into account during site finding include:

- initial assessment of wind conditions by using available public data which are related to the potential site or a place located nearby, although the obtained results cannot be entirely correct and reliable, but they will give an idea of how this terrain can be potentially favorable;
- overall assessment of the site, including topography and existing obstacles, such as buildings or woods and their potential effect on productivity and project value;
- location accessibility, taking into account access roads, their condition and distance from potential site, the size of components and quality specifications for necessary roads;
- availability of a node for the planned wind power station and the network power of the node in relation to the planned capacity and cost of additional electrical grid, taking into account network operation and adequate legislation;
- soil quality and work related to foundation plan and construction, as well as costs and their impact on the possibility of realization of wind power station;
- accounting of residential areas, infrastructure and potential effect of wind power station on the following factors: shade, noise, visibility, microwave data transferring, interference with radar, airports, etc.;
- openness of terrain, as to prevent wind current diffusion uplands must be separated by a distance at least 2-3 km;
- uplands should be columnar or cone shape;
- slopes must be low-sloped with incline not above 20°.

At the second stage exclusion criteria are used to determine if the place is suitable for wind power exploitation.

Exclusion criteria which are used for site finding for wind power stations include:

- districts near communities;
- industrial and commercial sites;
- hamlets, farms or detached houses;
- infrastructural areas where construction is prohibited;
- transportation infrastructure;
- overhead transmission lines;
- airports;
- mining areas;
- national parks, natural monuments, biosphere reserves, reserves, habitats which are protected by law;
- ponds.

At the third stage in conducting assessment of the site potentially suitable areas are tried out by taking into account technical and layout (ecology and land use) aspects:

- site topography, location of obstacles;
- access to transmission systems;
- maximum installed capacity;
- access to the site;
- land ownership;
- distance to populated localities;
- environmental constraints;
- layout of visually sensitive objects;
- the reliability of mobile telephone networks for data transfer;
- restrictive factors associated with communication signals such as microwave communication corridors, if applicable.

Construction of wind farms negatively affects the quality of the landscape and the aesthetic appearance of high quality landscapes on large areas of land. They are perceived as new, unnatural vertical structures that are not in harmony with most landscapes. The visibility of such facilities may be limited in landscapes with wedged elements, but in a flat, steppe, and arable landscapes they will be especially noticeable. High quality landscapes and environment which surround such areas, namely, environmental facilities, may be especially vulnerable to these effects.

All potentially suitable sites must be visited if possible in order to verify their existing conditions. Depending on the available land and topography, a wind-power station chart and balance settings can be designed. The assessment of the potential sites results in a ranking of site candidates.

2.2. Site selection for photovoltaic solar farms

The key characteristics of solar electricity technologies and their advantages and disadvantages which are taken into account when assessing the project are attributed to the location of the site (external shading and spatial constraints).

Choosing a proper site for a photovoltaic power station is essential for the success and economic viability of the project. The main factors which are taken into account when choosing the site include:

- initial assessment of solar resources in the form of global horizontal irradiation using publicly available data about the potential site or nearby locations;
- assessment of the site including the area, topography and existing obstacles, such as buildings or trees, and their potential impact on productivity associated with shading;
- availability of water for the construction and operation phases;
- analysis of land use that affects the cost of the land;
- the availability of areas on the basis of existing access roads, their condition and distance from a potential site. Proper condition of roads is required to avoid damage, mainly to inverters and photovoltaic modules during their transportation;
- existence of a point for attaching to the mains for the planned solar power-station and capacity of this main in relation to the planned capacity, and cost of necessary additional electricity;
- seismic risk, groundwater, soil resistivity, properties such as natural pH and bearing capacity. The last options are especially important for assessing the type of possible foundations of the mounting system;
- consideration of environmental and social sensitivity, visual and potential impacts of the solar system;
- the possibility of rational use of land which is situated under the station.

At the second and third stages while evaluating the site, potentially suitable areas are studied in detail considering technical and planning (ecology and land utilization) aspects and a ranking of sites is conducted. It is necessary to take into account the effect that the placement of photovoltaic panels and ancillary facilities on a flat area can have on the landscape, replacing the existing picturesque landscape with areas of panels which can be perceived as significant unnatural objects. Conservation areas and high quality landscapes and their environment may be especially vulnerable to these influences. However, solar energy facilities are likely to be low-lying, thus the impact on scenic views will be mostly noticeable if only observing from a hill or close to the facilities.

2.3. Site selection for hydroelectric power stations

Projects of small hydroelectric power stations differ with their significant flexibility. Small hydropower plants (SHPP) are characterized by great diversity. Areas of highlands and fast flowing waterways in the Carpathian region create the necessary

conditions for the construction of hydroelectric power plants (HPP) with medium or high pressure. Lowlands with wide rivers provide conditions for the construction of low-pressure SHPP. Most SHPP are channel stations, thus they produce electricity depending on the availability of water in the river. Therefore, they cannot be used for the production of peak electricity, and can only work in basic mode, the overall energy system.

Depending on the topography of the site, medium-, high- or low-pressure SHPP can be applied for power generation. Medium- and high-pressure HPP usually have a channel-forcing pipe or its variants in their schemes. The channel track depends on the form of terrain. If the construction of the channel includes difficulties, or it can be completely avoided, only the pressure pipeline is used. In places that are especially sensitive from an environmental point of view the only solution may be to lay down pressure pipeline in the ground to minimize its impact on the environment. Low-pressure SHPP may be built according to two schemes: with a derivative channel or a dike dam.

Planning and development of small hydropower stations must be take into account prevailing environmental conditions with simultaneous consideration of the possible impact on the environmental and social ambient which may be caused by its construction and operation. Therefore, in the first phase the basic requirements for the selection of the territory are related to the following data:

- topographical;
- hydrological;
- geological.

Possible costs for water intake combined with hydraulic pressure are the most important parameters for designing an SHPP. Typically, regional authorities of water resources measure water consumption on the most important rivers and streams, so these data can be obtained from them. The assumption of water in alignment does not take place except in cases where a water gauge post is installed. Therefore it is necessary to transfer data of an already existing water stage gauge on characteristics of water consumption in SHPP alignment. For this purpose measurement data are used, obtained at the nearest water stage gauge along the same river, or if possible, the data of a water stage gauge located near the proposed site of the SHPP. Data on the cost of water should cover the time period equal to at least 15 years in a row, if possible, to obtain statistically justified conclusions [7].

For the proper design of the engineering structures foundation it is necessary to obtain geological data that is as detailed as possible. The first assessment can be made with the help of geological maps that may exist at the district level. At this point estimates are indicative and should be complemented by further studies (e.g. geological mapping), during which a quite detailed map of the project area is prepared.

At the second stage of choosing the territory the accuracy should be raised and considered in more detail. Before the evaluation stage, it is necessary to carry out geological studies with further laboratory analysis of the samples. These tests are conducted to determine the parameters of rocks and soil on which the project of SHPP will be based. It must be emphasized that without adequate information of the

geological parameters of rock and soil, SHPP design contains a large number of unknown variables, which is a significant source of risk. Therefore, proper geological studies are a prerequisite for proper SHPP design.

It is necessary to exclude territory with:
- low or unregulated river flow;
- restricted or prohibited zones of economic activity;
- very steep slopes.

When evaluating areas for ranking it is necessary to consider a few key points:
- compliance with national legislation on environmental and social aspects;
- loss of habitat for local animals and plants;
- passes for fish and other aquatic organisms;
- rare species that are at risk of extinction.

Often the most attractive platform for small hydropower plants from an economic and technical point of view is less suitable in terms of ecology and tourism. For example, while the mountainous Carpathian region has the highest potential for small hydropower in Ukraine, it is also the richest in terms of clean, valuable and vulnerable areas. The presence of new dams, derivative pipes (if they are not underground), power lines and flooded areas may adversely affect the landscape's character and high quality environment, which in turn may adversely affect the tourism and recreational potential of the area.

3. SOLAR POWER IN THE TOURISM INFRASTRUCTURE

In this work recommendations are proposed for the pre-innovation segment of the tourism infrastructure for future development as major tourist centers and isolated settlements in the Carpathian region, focusing on the example of solar energy. Solar radiation depends on altitude, slope orientation and other mesofactors and microfactors, but throughout the Carpathian region it exceeds 1,000 kWh/m^2 per year [8]. That enables inclusion in a "green" tariff for electricity build as industrial, cost-effective solar power, as the source and use of solar energy for tourist complexes, private rural estates, "green tourism", street lighting, of local communities. The regional average annual values of the total solar radiation within the whole Carpathian region on the horizontal surface are presented on the Map Info map built in GIS by us in *Figure 1* containing 10 color gradations. The results indicate a gradual decrease in the quantitative indicators in the direction of the south-east-northwest.

The Ivano-Frankivsk region is suitable for solar energy usage *(Table 1)*. The annual solar radiation flux for the Ivano-Frankivsk region is 1,200 kWh/m^2, which is appropriate for solar energy facilities as well as for an industrial scale which would raise the infrastructural level of tourism in the region.

The analysis of the operation of power plant units in Lviv, Ivano-Frankivsk and Zakarpattia regions showed that solar photovoltaic power plant units (with a capacity of 1 megawatt) may generate nearly 1 million kWh of energy per year. It may take

nearly 7 years to pay off the investment of 1 million euro for 1 megawatt of solar electric plant peak power. The establishment of a local energy source as an element of tourist infrastructure in certain Carpathian regions will enable reliable and effective electricity supply to local consumers [9].

The estimated monthly volume of electricity production by installed photovoltaic solar power panels installed at a maximum of 2.8 MW of electric power *(Table 2)*.

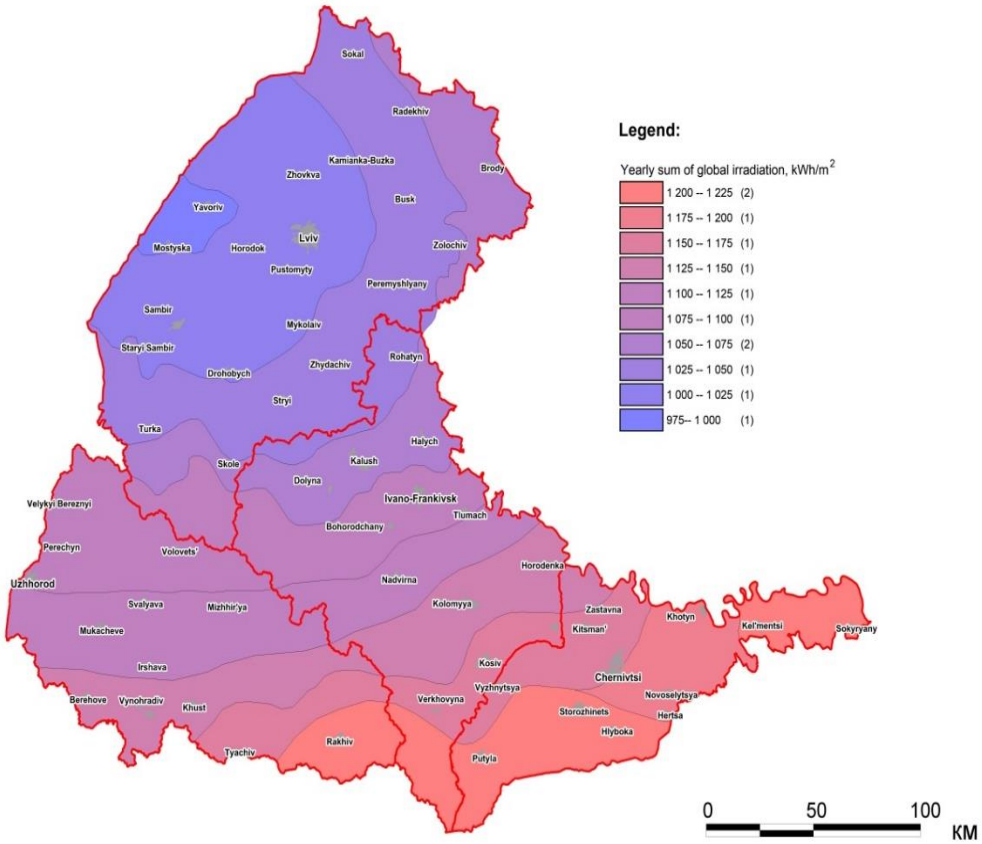

Figure 1
Total solar radiation on a horizontal surface
in the Carpathian region of Ukraine

For the development of tourism infrastructure it is proposed to use solar panels which are composed of photovoltaic cells and renewable energy sources for street lighting in villages *(Figure 2)* [10].

Table 1

Monthly meteorological data (Ivano-Frankivsk)

Month	**Horizontal emission, Kwh/m²**	**Tempe-rature, °C**	**General emission per area kWh/m²**	**Effective global emission, kWh/m²**
January	21.9	–3.98	46.4	44.9
February	39.9	–2.77	59.8	57.8
March	77.9	0.96	109.9	106.6
April	124.9	7.92	145.6	141.1
May	162.9	14.65	167.0	161.0
June	177.8	16.75	159.9	154.3
July	172.8	18.87	169.2	163.5
August	135.9	17.85	153.8	148.7
September	89.9	12.32	123.1	119.1
October	59.9	7.66	87.6	84.8
November	28.9	2.35	55.5	53.7
December	14.9	–3.53	41.3	39.9
YEAR	1,108.0	7.3	1,319.1	1,275.3

Table 2

Estimated monthly volume of electricity production by photovoltaic solar power panels installed at a maximum of 2.8 MW of electric power

Month	Efficient production on output of modules, MW per hour	The volume of supply to the network, MW per hour	The efficiency degree of generation, %	The degree of the system effectiveness
January	68.3	66.25	13.3	12.8
February	137.0	132.89	13.5	13.2
March	219.5	214.01	13.2	12.9
April	346.7	339.77	12.7	12.5
May	404.0	395.92	12.2	12.0
June	410.9	402.68	12.0	11.8
July	395.9	387.98	11.9	11.7
August	371.3	363.87	12.0	11.8
September	250.0	243.75	12.3	12.1
October	185.9	182.9	12.6	12.3

Novem-ber	99.4	96.42	13.0	12.6
Decem-ber	69.0	66.93	12.9	12.4
Year	2,957.9	2,893.37	12.4	12.2

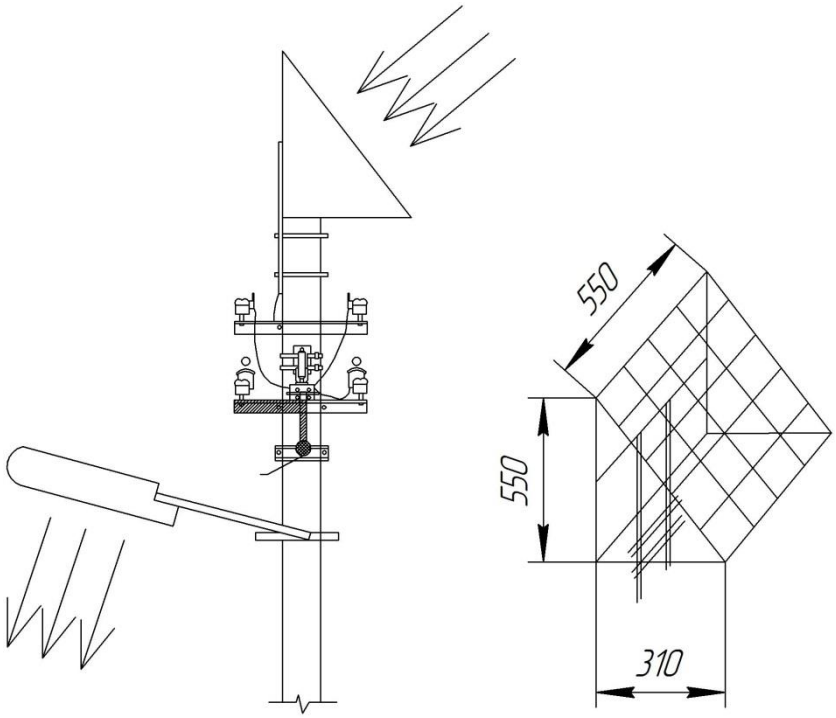

Figure 2
Technical parameters of solar panels

Technical parameters:

- Fully automatic operation control.
- Vertical ground level of illumination can reach 10–12 Lx.
- Provide 10 hours light every day, 4–10 hours light in bad weather.
- 7 m height. Operating temperature from –30 °C to 45 °C.
- It is appropriate to use LED lamps for the effective implementation of street lighting powered by photovoltaic solar cells.

4. CONCLUSIONS

When operating facilities using solar energy produce electricity without using fossil fuel (or nuclear power), a corresponding decrease is seen in fuel consumption for conventional thermal or nuclear power plants. Energy savings through the use of renewable, environmentally-friendly sources of energy is a promising innovative

segment in the development of tourism infrastructure and the development of green tourism in the Carpathian region, where more investment in the future will result in increased tourist demand.

The establishment of local energy sources as an element of tourist infrastructure in certain Carpathian regions will enable reliable and effective electricity supply to local consumers. Solar panels based on photovoltaic and renewable energy sources are proposed to develop the tourism infrastructure for street lighting in villages.

REFERENCES

[1] Plachkova, S. G., Plachkov, I. V., Bazeiev, E. T., Bondarenko, V. I., Buriachok, T. O. (2012–2013): Book 5. *Електроенергетика та охорона навколишнього середовища. Експлуатація енергетики в сучасному світі /Electric-power Industry and environmental protection. Operation of energy in the modern world.* Access: http://energetika.in.ua/ua/books/book-5/part-1/section-2.

[2] Kudria, S. A., Mkhytarian, N. M., Reztsov, V. F., Surzhyk, T. V., Yatsenko L. V. (2011): Потенціал та перспективи використання відновлюваних джерел енергії в Україні/Potential and Perspectives of Use of Renewable Energy Sources in Ukraine. *International scientific journal Alternative Energy and Ecology*, V.32. pp. 150–163.

[3] Adamenko, O. M., Vysochanskyi, V. V., Lotko, V. V., Mykhailiv, M. I. (2000): *Альтернативні види палива та інші альтернативні джерела енергії./Alternative fuels and other alternative energy sources. Tutorial for energy and environmental specialties of higher educational institutions*. Ivano-Frankivsk: Polumia.

[4] Shydlovskyi, A. K. (2007): *Енергоефективність та відновлювана енергія /Energy Efficiency and Renewable Energy*. Kyiv, Ukrainian Encyclopedic Knowledge.

[5] Mandryk, O. M., Arkhypova, L. M., Pobigun, O. V., Maniuk, O. R. (2015): Renewable energy sources for sustainable tourism in the Carpathian region, IOP Conf. Series: *Materials Science and Engineering*, 144.

[6] *Програма стратегічного екологічного аналізу в Україні (Прог-рама альтернативного енергетичного фінансування)/The Program of Alternative Energy Funding in Ukraine (USELF) Strategic Environmental Analysis*. Environmental report, 2012.

[7] *Атлас енергетичного потенціалу відновлюваних та альтер-нативних джерел енергії в Україні: вітроенергетика, сонячна енергетика, малі річки, біомаса, геотермальна енергія, енергетика, навколишнє середовище, енергетичні відходи в енергетичному потенціалі енергія нетрадиційного палива/Atlas of the energy potential of renewable and*

alternative energy sources in Ukraine: wind power, solar power, small rivers, biomass, geothermal energy, energy, environment, energy waste in Energy potential energy of unconventional fuels. Kyiv, Ukraine: National Academy of Sciences, Institute of Electrodynamics, State Committee of Ukraine Energy Eaving, 2001.

[8] Mandryk, O. M., Moskalchuk, N. R., Arkhypova, L. M., Pryhodko, M. M., Pobigun, O. V. (2020): Research quantitative indicators of the potential of solar energy in the Carpathian region of Ukraine IOP Conference Series: Materials Science and Engineering/IOP Conf. Series: *Materials Science and Engineering*, 749, 012033/IOP Publishing/.

[9] Kinash, I., Arkhypova, L., Polianska, A., Dzioba, O., Andrusiv, u., Yuras, Yu. (2018): Economic evaluation of tourism infrastructure development in Ukraine. IOP Conf. Series: *Materials Science and Engineering*, 477 (1).

[10] Архипової, Л. М., Мандрик, О. М., Архипова, Л. М., Адаменко, Я. О., Приходько, М. М., Адаменко, О. М., Побігун, О. В., Манюк, О. Р., Москальчук, Н. М., Мурава, Ю. І., Михайлюк, Ю. Д. (2016): *Стратегічна оцінка використання відновлюваних джерел енергії у сталому туристично-рекреа-ційному розвитку Карпатського регіону/Strategic assessment of the use of renewable energy in sustainable tourism and recreational development of the Carpathian region :колективна монографія за ред*. Івано-Франківськ: ІФНТУНГ, pp. 323.

Geosciences and Engineering, Vol. 7, No. 10 (2019), pp. 60–73.

THE LEGAL CATEGORIZATION OF FLY ASH IN EU AND THE HUNGARIAN LAW – ANALYSIS OF RELATED CJEU CASE-LAW

CSILLA CSÁK – GYÖRGY MARINKÁS

Faculty of Law, University of Miskolc

Abstract: The aim of the current article is to examine the rules on utilization of the fly ash in Hungarian and EU law. In order to thoroughly present and introduce these rules, the authors of the current article – in the *first chapter* – first took a glance on the technical assessment of the fly ash. In the *second chapter* the authors introduce the legal standing of the fly ash in the EU law and provide a glance on the international examples, than in the second subchapter they introduce the actual EU law. Having regarded that the European Court of Justice (CJEU) has a paramount role in shaping EU law, one should not omit the introduction of the concerning CJEU case-law.

Keywords: *fly ash, waste management, waste disposal, cyclic environment, EU law, CJEU*

1. INTRODUCTION

The aim of the current article is to examine the rules on utilization of fly ash in Hungarian and EU law. Fly ash, which is a residue material of coal combustion power plants, nowadays is widely used to enhance the mechanical – and other – properties of building materials – e.g. concrete – and to produce geopolymers, which is a relatively novel utilization of fly ash. In doing so – that is to say in utilizing the fly ash – it is not irrelevant what the legal rules and the legal environment allow and what they offer to the economic actors who opt for the utilization of this material instead of depositing it. As an example: while the EU law prefers utilization of waste materials in order to create a circular economy, the principle of proximity – which shall be taken into consideration – does not facilitate the utilization of fly ash, since this principle – alongside economic considerations – excludes the transportation of material for greater distances.

In order to thoroughly present and introduce these rules, the incentives and the difficulties, the authors of the current article – in the *first section* – first take a glance at the technical assessment of the fly ash: its formation and ways of utilization. Taking into consideration that they are lawyers and not technicians, this part only strives to sum up the formation, types and utilization of the fly ash, without going into technical details. Speaking of fly ash – which mainly arises from coal combustion power plants – the sustainability of the coal combustion power plants shall be examined

from an economic and environmental aspect. Thus the authors devoted a subsection to this topic.

In the *second section* the authors introduce the legal standing of the fly ash in EU law and provide international examples, then in the second subsection they introduce the actual EU law and the Hungarian laws and government decrees implementing it. The relevant EU law is rather divergent: while the Waste Directive – which classifies fly ash as waste and thus determines its legal standing – provides the regulatory framework, other directives, regulations and decisions of the Commission provide for the detailed rules of utilizing fly ash. Considering that the European Court of Justice (CJEU) has a paramount role in shaping EU law, one should not omit the introduction of relevant CJEU case law concerning the notion of waste, the classification of materials as waste and concerning coal combustion power plants. Thus, the authors introduce the relevant cases in order to provide a full picture on the utilization of fly ash.

Last, in the third, summarizing section, the authors draw their conclusions.

2. TECHNICAL ASSESSMENT OF FLY ASH: ITS FORMATION AND WAYS OF UTILIZATION

2.1. Energy resources and heating by coal

Power plants can be divided into three groups; depending on the primer – that is to say natural – *energy resources* they are either *thermal, hydroelectric* or *nuclear power stations*. Thermal power plants utilize *coal, oil, oil derivatives* and *natural gas* for combustion. The three categories of coal are *lignite, pitch-coal,* or *hard/black coal.* The latter one is the most commonly used type of coal. Nowadays, power plants fuelled by *biomass* or *household waste* are more common; however the fly ash arising from these has different physical and chemical attributable, which can affect its utilization [1].

In Hungary coal is the third most important energy source for producing electricity after natural gas and nuclear power; the major part of the extracted coal is utilized for this purpose. Thus coal as a source of energy cannot be circumvented and interest in environment-friendly and sustainable *clean coal technologies* (CCT) is on the rise [2].

2.2. The formation of fly ash in power plants and its utilization

Thermal power plants can be categorized based on the coal combustion procedures used. The chosen technology affects the characteristics of the *residues*, which have various names in the literature.[1] These residues can be divided into two major groups: the first group consists of fly ash*, bottom ash* and *boiler slag*, which are the incombustible residues of the coal. The second group is constituted from the residues of the air quality management devices – e.g. *desulphurisation systems* – among others FGD[2] gypsum. [2]

---

[1] Among others: reuse waste from coal-fired power plants, bottom ash and slag tap from coal-fired power plants, etc. [2]

[2] Flue Gas Desulfurization.

As mentioned above, power plants can be categorized based on the technologies they use. The first of the three types is *high temperature combustion*, which produces *ash* and *boiler slag*. Ash is the residue arising from the combustion of organic materials and consists of mainly dust or melted material in greater pieces. The melted materials are constituted from the non-volatile residues of the oxidisation: non-organic salts and oxides. In case the ash is cooled in water, the originating residue is *boiler slag*. These kinds of power plants produce fly ash only in a limited extent, and much of it can be fixed in the chimney via abatement technologies [2]. From the total amount of ash produced in power plants, 80–85% arises from *dry combustion power plants* as *ultra-fine* fly ash, which is collected in the *mechanical* or *electro filters.* Fly ash can be defined as the fine-grain part of the coal's ash content, which exits through the chimney together with the combustion/flue gases [3]. *Mechanical dust abatement* devices collect the rough and hard particulars of the fly ash and thus function as a pre-abatement system. Mechanical abatement can be realized through a settling chamber, whirl-tube, etc. Electro-static dust abatement is carried out through electro-filters, which fix the finer and lighter parts of the ash[3] [2]. The third method is *fluidized bed combustion*, where the procedure is carried out without melting. The resulting grains mostly have an irregular shape with a high amount of crystals [1].

The utilization of fly ash from power plants is quite far-reaching: the cement and concrete industry has been using it since the 1930s in order to enhance the characteristics of their products. Furthermore, it has long been used in the construction of motorways and for stemming in the mining industry [44]. As a novel utilization method, fly ash is used for the production of *geopolymers* and to *fix harmful materials* [4].

2.3. Fly ash arising from the combustion of waste materials [5]

Although the aim of the current article is to introduce the fly ash arising from coal combustion power plants, it is worth mentioning that the combustion of waste too, produces fly ash. Based on the literature, *thermal waste management* procedures can be divided into three main categories: *waste combustion*, *cracking*, and *gasification.* The first one is the most common method among them. The procedure – to keep it simple – is the following: the organic components of the waste are transformed into gases and steam, then exit the system as combustion/flue gases. Incombustible materials remain in the system as slag and ash. The aim of this procedure is to *extract and utilize the energy to be found in the waste to the greatest possible extent;* thus, it is quite common that waste combustion plants often produce heat, steam or electricity. This renders a demarcation between the power plants and the waste combustion plants necessary: in this regard Directive 2010/75/EU on industrial pollution provides the necessary guidance, stating that

[3] In case of coals with greater sulphur content, the combustion/flue gases are led into an absorber in order to desulphurize them. The side-product of this procedure is *flue gas desulphurisation (FGD) gypsum.*

the determinant factor is the primary aim of the plant. That is to say, if the management of waste is the primary objective of a plant, then the plant in question shall be regarded as a waste management plant [1].

As mentioned earlier, the fly ash coming from waste combustion has different physical and chemical attributes, which can affect the utilization of the fly ash [1].

2.4. The sustainability of coal combustion power plants and the limitations of utilizing fly ash

Coal as a fossil combustible is the most evenly distributed energy source in the world. Based on the current estimations, the world's stocks of coal will be enough for the next 130–200 years [2]. That is to say, coal combustion power plants should be sustainable for a rather long period of time; their sustainability is affected by two other factors, however. First, regarding the aspects of environment protection, it is necessary to decrease the waste produced worldwide, including the waste produced by these power plants; second, a major part of the coal-combustion plants already run with a negative trade balance, which questions their sustainability in the long run.

Regarding the *first factor* it has to be emphasized that the primary objective is to reduce the amount of waste produced. The *European Coal Combustion Products Association* (ECOBA) in its report estimated that in 2012 the mining and the industrial sector of the then 27 EU member states produced 100 million metric tons of power plant residues per year, 68% of which was fly ash. This amount can be reduced as the technology evolves; however, it cannot be eliminated totally [2]. Furthermore transporting the fly ash for longer distances is not conforming to the *principle of proximity* as contained by Article 16 of *Directive 2008/98/EC* [7] *on waste* (hereafter: waste directive). The article sets out that waste shall be utilized or disposed where it was produced. Last but not least, fly ash cannot be transported on the road economically, which limits its utilization. [8]

Regarding the *second factor* mentioned above, is that *2017 was the point of inflexion in the rivalry between the fossil fuels and renewable energy sources:* from that year – considering the cost of the construction and the index of return – it became more economical to invest in renewable energy sources than in fossil ones. *At the moment 619 coal combustion power plants function within the territory of the EU, half of which exhibit a negative trade balance,* according to a recent report [9] of the *Carbon Tracker*, a think tank specialized in climate change. Based on the calculations of the *Financial Times* [10], by the year 2030 the proportion of power plants with a negative trade balance will grow to 97% from the current 54%. Should governments decide to keep the sector alive, they will have to spend 22 billion euros for that purpose. The costs are enhanced furthermore by the fact that in order to reach the goals of climate protection, these investments should be realized swiftly and productivity should be reduced at the same time. The lost profit must be subsidiarized, which likely means a rise in energy prices, paid by the consumers at the end of the day [11]. Nevertheless, the current plans propose to shut down only one third of

the power plants by 2030. Thus, the amount of fly ash will not reduce by any considerable amount until then.

3. THE LAW OF THE EUROPEAN UNION ON FLY ASH AND RELEVANT CASE LAW OF THE CJEU

3.1. Waste management in the EU and the legal standing of fly ash

The most important secondary EU law is the already mentioned waste directive [7]. Given the fact that *the EU law does not have a distinct regulation on the fly ash*,[4] *general waste management rules shall prevail.* Based on Article 3 Point 1 of the waste directive – which defines 'waste as' any substance or object which the holder discards or intends or is required to 'discard' – *fly ash shall be classified as waste*. The exact classification of fly ash is to be found in Commission Decision 2014/955/EU, [12] which in its index list fly ash among wastes, under the number '10 01 02 coal fly ash'.

The reasoning for this classification is that fly ash, bottom ash, boiler slag and FGD-gypsum are created as a result of the functioning of power plants. Strictly speaking, however, the product of these plants is the energy. Any other product originating from the procedure is a by-product, which is not needed by the power plants. As a result these materials are classified as *industrial wastes*, or technological industrial wastes to be more precise [2]. In order to secure the prevalence of the environment protection principles – with special regard to the *polluter pays principle* – the law of the EU prefers to call these materials waste [13], [14]. Thus the secondary sources of EU law list these materials in the waste catalogue. The case law of the CJEU[5] also supports this. It is worth mentioning, however, that in other parts of the world – e.g. in the US or India – the above-mentioned materials are classified as by-products, as their characteristics are identical to natural raw materials and can be utilized as a raw material [2].

Considering the fact that coal combustion power plants produce greenhouse gases, it is worth taking a look at the secondary sources of EU law concerning the topic and the CJEU's case law regarding their applicability. The rules on the emission of greenhouse gases and the system of quotas are to be found in *Directive 2009/29/EC* [15] which – among others – modified the earlier *Directive 2003/87/EC* [16].

Another directive to be mentioned is *Directive 2010/75/EU on industrial emissions* [6]. Articles 28–41 of Chapter III of the directive define the scope of the directive as follows: '[it] covers any combustion plants, the total rated thermal input of which is equal to or greater than 50 MW, irrespective of the type of fuel used.' The articles furthermore contain the specific rules on any combustion device and the rules on monitoring emissions. Article 42 of Chapter IV demarcates the difference between power plants and waste incarceration plans that produce energy as a by-product.

---

[4] Contrary to the wastes of the mining industry, which are regulated under a specific directive.

[5] To be introduced in the next sub-chapter.

The related decisions of the Commission and the implementing decisions of the Commission are given in Commission implementing decision (EU) *2017/1442* [17], in which the Commission recorded its conclusions regarding the *best available techniques* (BAT) as provided in Directive 2010/75/EU. *Commission Decision 2011/278/EU* [18] and *Commission Decision 2017/126* [19] are worth highlighting too, where the Commission laid down the transitional Union-wide rules for the harmonized free allocation of emission allowances under Directive 2003/87/EC from 2013 onwards and amended Decision 2013/448/EU, respectively [20]. Commission Regulation (EU) No. 601/2012 on the monitoring and reporting of greenhouse gas emissions pursuant to Directive 2003/87/EC [21] is also worth mentioning, where the Commission set out rules for aircraft operators. In order to facilitate the execution of the this directive, the Commission issued guidance on 16 July 2012 [22].

Last but not least, the 2012 opinion of ECOSOC[6] [23] is worth mentioning: ECOSOC reminded us that based on a 2012 ECOBA report on the then EU-27 the mining and the industrial sector produced 100 million metric tons of waste, 68% of which was fly ash. ECOSOC examined the utilization of fly ash and the issue of the high amount of fly ash disposed in landfills. It found that the fly ash is not only suitable to produce geopolymers, but is also suitable for use as an additional material in concrete, as scale in the automotive industry and as a detergent in sewage water management. The body also stated that it would be expedient to carry out voluntary research on the quantity and quality of fly ash and boiler slag created in power plants and factories EU-wide in order to find out the percentage of these by-materials that is being deposited in landfills instead of being utilized. It is worth mentioning, however, that based on the ECOSOC opinion the fly ash being produced in Europe is not always suitable for re-utilization and the potential utilizers are not always well aware of the possibilities.

3.2. The objectives of waste-management

After introducing the secondary legal sources on waste management we introduce how the EU institutions set the objectives based on the secondary sources of law. One of these documents is a 2017 report of the *European Parliamentary Research Centre* [24]. The main objective in this regard is that the single market of the EU shall become a *circular economy* in the future. Thus, waste generation cannot be considered as a necessary evil, instead the member states should strive to (i) reduce the waste generated during production. – The most effective waste-management tool. – Furthermore, member states should strive to (ii) implement a holistic view, which takes into consideration the demand on good quality secondary materials. That is to say, producers should generate as little waste material as possible and – in case it is impossible to avoid the creation of waste – the generated waste should be suitable for re-utilization to the greatest extent possible.

---

[6] European Economic and Social Committee.

Both the EU and the member states have numerous tools to achieve these goals and to stimulate economic actors: (i) setting objectives and creating obligations – like the liability of the manufacturer – through *legislation;* applying (ii) *economic incentives* in the field of waste collection and research. Furthermore (iii) *market-based solutions* like taxes, fees and Pay as You Throw Schemes (PAYT) can be applied, or they can (iv) *demand producers to inform consumers on their envirentalism.* Last, but not least (v) *voluntary tools* can be applied, e.g. campaigns, voluntary obligations, labelling, good practices.

Examining the actual status of waste management does not show an appealing picture, however: based on the 2015 report of the *Waste and Resources Action Programme* [25] (hereafter: WRAP) in 2012 the industry of the EU-28 processed a total 5 billion metric tons of raw materials. Only 20% of this amount was secondary raw material. That is to say *the economy of the EU-28 is still linear* and characterized by the wasteful utilization of our limited natural resources: *most of the processed raw materials perish in the end of the process.* The situation is worsened by the fact that 1.2 billion tons are still deposited on landfills, creating a heavy burden on the environment. The report states – in accordance with the EPRC report [24] mentioned above – that the most effective waste-management method is prevention, that is to say the decreasing of the waste generated. Considering that the amount of household waste is on the rise year by year, reversing this trend seems almost impossible. The waste directive demands the utilization of 70% of the waste generated by 2030. Several member states are lagging far behind in this question, however [7].

3.3. Relevant case law of the CJEU

The fact that the waste can be utilized as raw material with a value that can be expressed in money and thus it constitutes "goods" for the purposes of the Treaty was stated in the case *C-2/90 Commission vs. Belgium* [27]. *The definition of waste was elaborated by the ECJ*[7] *in the C-235/02 Saetti et Frediani case*: the domestic court sought for the answer of whether *petroleum coke* constitutes waste for the purposes of Council Directive 75/442/EEC. The ECJ was of the view that: 'Petroleum coke which is produced intentionally or in the course of producing other petroleum fuels in an oil refinery and is certain to be used as fuel to meet the energy needs of the refinery and those of other industries does not constitute waste within the meaning of Council Directive 75/442/EEC' [28].

In the C-252/05 *Thames Water Utilities* case the referring court sought to ascertain whether waste water constitutes waste within the meaning of Directive 75/442 where it escapes from a sewerage network. The ECJ was of the view that the fact that waste water escapes from a sewerage network does not affect its character as 'waste' within the meaning of Directive 75/442. The ECJ stated furthermore that *'the fact that the waste water is spilled accidentally does not alter the outcome'* [29].

---

[7] The CJEU is composed of the General Court (GC) and the European Court of Justice (ECJ).

The *C-304/94 Tombesi et al. case* was the first case, where the ECJ – concurring with the opinion of the advocate general – held as a principle that '[t]he Community rules on waste [...] apply to any substances or objects which the holder discards or intends or is required to discard, even where they are capable of re-use and may be the subject of a legal transaction or quoted as being of commercial value on public or private commercial lists'. On the other hand, the advocate general emphasized that *it was difficult to make a distinction between the utilization of waste and the utilization of secondary raw materials* based on then-effective directives since their definitions were ambiguous. Furthermore, it is worth mentioning that this was the first case where FGD-gypsum was nominated *expressis verbis* [30], [31].

The limitation of emissions of certain pollutants into the air from large combustion plants was the subject of the *C-304/15 Commission v. United Kingdom case* [32]. When the case was instituted Directive 2001/80/EC [33] was in force. The Commission launched an infringement procedure because the Aberthaw power plant did not fulfil the criteria provided in Footnote 3 Part 'A' of Annex IV of the directive. The government argued that the criteria were unfounded and it was impossible to fulfil them based on the calculation method demanded by the directive. The advocate general was of the view that the position of the United Kingdom is untenable: since the directive requires compliance on an annual basis it can be fulfilled even if the emission protrudes on occasion due to the insufficient quality of the coal. Thus, the advocate general suggested that the court should order that the UK was in breach of its obligations under the Treaty [34]. The ECJ was of the same view [32].

In the *C-460/15 Schaefer Kalk case* the advocate general was of the view that *producing greenhouse gases does not constitute emission provided that these gases are never released into the atmosphere. In case they are released, however, the date and place of release* – that is to say if they were released from another factory – *is irrelevant*. The advocate general argued that any other interpretation would allow the issuers to play tricks on the emission quotas. On the other hand, the advocate general discarded the arguments of the Commission and the German authority: the Germans argued that the quotas should be applied on the whole amount of the transferred carbon dioxide. The advocate general was of the view that this would be disproportionate compared to the otherwise legitimate objective [35]. The ECJ approved and delivered the following judgement: 'The [mentioned EU laws] are invalid in so far as they systematically include the carbon dioxide (CO_2) transferred to another installation for the production of precipitated calcium carbonate in the emissions of the lime combustion installation, regardless of whether or not that CO_2 is released into the atmosphere' [36],

One of the most recent cases is the *C-58/17 INEOS Köln GmbH v. the Bundesrepublik Deutschland case.* In the preliminary ruling the referring court in essence sought the answer for the question of whether Article 3(h) of Decision 2011/278 must be interpreted as precluding national legislation, such as that at issue in the main proceedings, which excludes from the concept of 'process emissions sub-installation', within the meaning of that provision, greenhouse gas emissions stemming from the combustion of incompletely oxidised carbon in a liquid state? [37] The ECJ

was of the view that the aim of Directive 2003/87 is to reduce the emission of greenhouse gases, with regard to economic aspects. On the other hand, neither Directive 2003/87 nor Decision 2011/278 on its execution refers *expressis verbis* to effective energy recovered from incompletely oxidised carbon in a liquid state. The aim of the directive is to recycle or utilize any by-products – including greenhouse gases – for energy production. Environmental protection rules must be taken into consideration, however: these rules make it clear that incompletely oxidized carbon in a liquid state is not in conformity with the rules. As a consequence, the ECJ was of the view that "[related EU law] must be interpreted as not precluding national legislation, such as that at issue in the main proceedings, which excludes from the concept of 'process emissions sub-installation', within the meaning of that provision, greenhouse gas emissions stemming from the combustion of incompletely oxidised carbon in a liquid state".

Similarly *the definition of sub-installation constituted the subject of the C-158/15 Elektriciteits Produktiemaatschappij Zuid-Nederland EPZ NV case*. The advocate general was of the view that the warehouse is part of the installation, as it is technically necessary for the installation's functioning, thus CO_2 quotas shall prevail. In her view the coal wasted as a result of self-heating does not constitute 'exported' within the meaning of Commission Regulation 601/2012/EU, only if it is transported to other installations or sub-installations which actually fall out of the system. In the case at hand neither condition applied [38]. The ECJ in its judgement was of the same view [39].

In the *C-302/17 PPC Power case* the referring court asked 'whether Directive 2003/87 must be interpreted as precluding national legislation, such as that at issue in the main proceedings, which taxes, at 80% of their value, greenhouse gas emission allowances allocated free of charge which have been sold or not used by the undertakings subject to the greenhouse gas emission trading scheme' [40]. The Court was of the view that: 'By eliminating virtually all of the economic value of emission allowances, *the tax amounts to a negation of the incentive mechanisms underpinning the emission allowance trading system* [and[8] thus the relevant EU law] must be interpreted as precluding national legislation, such as that at issue in the main proceedings, which taxes, at 80% of their value, greenhouse gas emission allowances allocated free of charge which have been sold or not used by the undertakings subject to the greenhouse gas emission trading scheme.' [40]

Last but not least, the *T-57/11 Castelnou Energía SL case* [41] is worth mentioning. In this case the domestic law required the ten electricity plants to source 'indigenous' coal (i.e. coal of Spanish origin), the price of which is higher than that of other fuels, and to produce certain volumes of electricity from that coal. In order to compensate the affected power plants the government created a so called 'preferential dispatch mechanism'. While the Commission was of the view [42] that the above-mentioned mechanism constituted state aid, it decided to dispense with insti-

[8] Emphasis added by the authors.

tuting procedures since 'it declared the aid at issue compatible with the internal market under Article 106(2) TFEU […] in so far as the application of such rules does not obstruct the performance, in law or in fact, of the particular tasks assigned to them'. *The General Court (GC) dismissed the application on the ground of the lack of locus standi:* the applicant was not the addressee of the contested decision and failed to put forward any specific arguments that the decision directly and individually concerned it [41].

4. SUMMARY

The aim of the current article was to examine the rules on utilization of the fly ash in Hungarian and EU law. We first took a look at the technical assessment of the fly ash, the majority of which comes from power plants, introducing its formation and ways of utilization. We also introduced and examined the sustainability of coal fuelled power plants and found that 2017 was the point of inflexion: from that year on investors should invest in renewable energy sources instead of fossil energy sources. The current energy policy seems determined to subsidize the already loss-making sector until 2030 and only proposes the shut-down of 1/3 of coal fuelled. Keeping such plants in operation provides the industrial sector with the useful secondary raw material – that is to say, with fly ash – but does not conform to the environmental goals of the EU, including the goals of the waste-management, which aims at reducing waste generated.

In the *second section* the authors introduced the legal standing of the fly ash in EU law and provided a glimpse at international examples. The relevant EU law is heterogeneous: the Waste Directive provides the regulatory framework and the framework is filled in with other directives, regulations and decisions of the Commission. Commission decisions provide the detailed rules of utilizing fly ash. The authors introduced the relevant cases in order to provide a full picture of the rules of waste management in the EU, including the notion and classification of waste and the rules on power plants that produce fly ash. The ECJ in its case law tries to strike a fair balance between the interests of environment protection goals and economic actors, as highlighted by the C-460/15 Schaefer Kalk case.

REFERENCES

[1] Mucsi G. (2014): Széntüzelésű erőműi pernye keletkezése. In: Mucsi Gábor (szerk.): *Erőműi pernye komplex hasznosítása.* CriticEl Monográfia sorozat 6, p. 45.

[2] Bőhm J. (2012): Erőműi maradványanyagok jogi megítélése az Európai Unióban. *Műszaki Földtudományi Közlemények,* 83. kötet, 1. szám, pp. 5–12.

[3] Heidrich, C., Feuerborn, J. J., Weir, A. (2013): *Coal Combustion Products: A Global Perspective.* World of Coal Ash Conference. Lexington KY, April 22–25.

[4] Bokányi L., Rácz Á. (2014): Kritikus elemek kinyerése erőműi pernyéből. In: Mucsi Gábor (szerk.): *Erőműi pernye komplex hasznosítása.* CriticEl Monográfia sorozat 6, pp. 89–210.

[5] Képviselői Információ Szolgálat: *Hulladékerőművek, hulladékégetés.* Infójegyzet 2016/23 – Available online at: http://www.parlament.hu/documents/10181/595001/Infojegyzet_2016_23_hulladekegetes.pdf/c4ea1502-7026-4a7b-98eb-99bc653ece1a (30/01/2019).

[6] *Directive 2010/75/EU* of the European Parliament and of the Council of 24 November 2010 on industrial emissions (integrated pollution prevention and control) (OJ L 334, 17. 12. 2010, pp. 17–119.).

[7] *Directive 2008/98/EC* of the European Parliament and of the Council of 19 November 2008 on waste and repealing certain Directives (OJ L 312, 22. 11. 2008, 3–30.). Implemented into the Hungarian legal-framework by: Act CLXXXV of 2012 on waste. National Waste-management Plan of Hungary, enacted by Government Decree 2055/2013 provides for the details of the execution of the said act.

[8] Debreczeni Á., Gombkötő I. (2014): Pernye-zagyok hidraulikus szállítása, paszta technológia. In: Mucsi Gábor (szerk.): *Erőműi pernye komplex hasznosítása*. CriticEl Monográfia sorozat 6, p. 63.

[9] Carbon Tracker (2017): *Lignite of the living dead*. – Available online at: https://www.carbontracker.org/reports/lignite-living-dead/ (30/01/2019).

[10] Financial Times (2017): *European coal staring into abyss, says climate study*. Available online at: https://www.ft.com/content/f32c3caa-daf3-11e7-a039-c64b1c09b482 (30/01/2019).

[11] Wynn, G., Coghe, P. (2017): *Europe's Coal-Fired Power Plants: Rough Times Ahead Analysis of the Impact of a New Round of Pollution Controls*. 20. Available online: https://ieefa.org/wp-content/uploads/2017/05/Europe-Coal-Fired-Plants_Rough-Times-Ahead_May-2017.pdf (15/04/2020).

[12] *Commission Decision 2014/955/EU* (18 December 2014) amending Decision 2000/532/EC on the list of waste pursuant to Directive 2008/98/EC of the European Parliament and of the Council Text with EEA relevance (OJ L 370, 30. 12. 2014, pp. 44–86.).

[13] Csák Cs. (2014): Hulladék vagy melléktermék? – avagy a mezőgazdasági maradványanyagok jogi megítélése. *Őstermelő: Gazdálkodók Lapja Plusz*, (2), pp. 14–16.

[14] Csák Cs.: A hulladék fogalmának értelmezése az uniós ítélkezési gyakorlat alapján. *Sectio Juridica et Politica,* Miskolc, Tomus XXIX/2. (2011), pp. 423–434.

[15] *Directive 2009/29/EC* of the European Parliament and of the Council of 23 April 2009 amending Directive 2003/87/EC so as to improve and extend the greenhouse gas emission allowance trading scheme of the Community (OJ L 140, 5. 6. 2009, pp. 63–87.).

[16] *Directive 2003/87/EC* of the European Parliament and of the Council of 13 October 2003 establishing a scheme for greenhouse gas emission allowance trading within the Community and amending Council Directive 96/61/EC (OJ L 275, 25. 10. 2003, pp. 32–46.).

[17] *Commission Implementing Decision (EU) 2017/1442* of 31 July 2017 establishing best available techniques (BAT) conclusions, under Directive 2010/75/EU of the European Parliament and of the Council, for large combustion plants [notified under document C(2017) 5225] C/2017/5225 (OJ L 212, 17. 8. 2017, pp. 1–82.).

[18] *Commission Decision 2011/278/EU* (27 April 2011) determining transitional Union-wide rules for harmonised free allocation of emission allowances pursuant to Article 10a of Directive 2003/87/EC of the European Parliament and of the Council [notified under document C(2011) 2772] OJ L 130, 17. 5. 2011, pp. 1–45.).

[19] *Commission Decision 2017/126/EU* (24 January 2017) amending Decision 2013/448/EU as regards the establishment of a uniform cross-sectoral correction factor in accordance with Article 10a of Directive 2003/87/EC of the European Parliament and of the Council C/2017/0367 (OJ L 19, 25. 1. 2017, pp. 93–95.).

[20] *Commission Decision 2013/448/EU* (5 September 2013) concerning national implementation measures for the transitional free allocation of greenhouse gas emission allowances in accordance with Article 11(3) of Directive 2003/87/EC of the European Parliament and of the Council [notified under document C(2013) 5666] (OJ L 240, 7. 9. 2013, pp. 27–35.).

[21] *Commission Regulation 601/2012/EU* (21 June 2012) on the monitoring and reporting of greenhouse gas emissions pursuant to Directive 2003/87/EC of the European Parliament and of the Council Text with EEA relevance (OJ L 181, 12. 7. 2012, pp. 30–104.).

[22] European Commission: The Monitoring and Reporting Regulation – General guidance for installations. *MRR Guidance document*, No. 1, 60.

[23] *The European Economic and Social Committee:* Opinion on 'The processing and exploitation, for economic and environmental purposes, of industrial and mining waste deposits in the European Union' (own-initiative opinion) OJ C 24, 28. 1. 2012, pp. 11–17.

[24] EPRS: *European Parliamentary Research Service Scientific Foresight Unit (STOA) PE 581.913.* Available online at: http://www.europarl.europa.eu/RegData/etudes/STUD/2017/581913/EPRS_STU%282017%29581913_EN.pdf (30/01/2019).

[25] Mitchell, P., James, K. (2015): *Economic Growth Potential of More Circular Economies*. WRAP, September 2015. Available online at: http://www.wrap.org.uk/sites/files/wrap/Economic%20growth%20potential%20of_more%20circular%20economies.pdf (30/01/2019).

[26] Communication from the commission: Closing the loop – An EU action plan for the Circular Economy COM/2015/0614 final.

[27] CJEU: C-2/90, *Commission v. Belgium*, Judgment, 9 July 1992, paras. 23, 37.

[28] CJEU: C-235/02, *Saetti et Frediani*, Judgment, 15 January 2004, para. 47.

[29] CJEU: C-252/05 *Thames Water Utilities*, Judgment, 10 May 2007, paras. 28–29, 42.

[30] CJEU: C-304/94, *Tombesi and Others*, Opinion of Advocate General Jacobs, 24 October 1996, para. 62.

[31] CJEU: C-304/94, *Tombesi and Others*, Judgment, 25 June 1997, para. 42.

[32] CJEU: C-304/15, *Commission vs. United Kingdom*, Judgment, 21 September 2016.

[33] *Directive 2001/80/EC* of the European Parliament and of the Council of 23 October 2001 on the limitation of emissions of certain pollutants into the air from large combustion plants OJ L 309, 27. 11. 2001, pp. 1–2. (No longer in force, Date of end of validity: 31/12/2015; Repealed by: Directive 2010/ 75/EU.)

[34] CJEU: C-304/15 *Commission v. United Kingdom*, opinion of Advocate General Bobek, 2 June 2016, paras. 24–32, 48.

[35] CJEU: C-460/15 *Schaefer Kalk*, opinion of Advocate General Sharpston, 10 November 2016, paras. 19–24, 38–45, 51.

[36] CJEU: C-460/15 *Schaefer Kalk*, Judgment, 19 January 2017, para. 50.

[37] CJEU: C-58/17 *INEOS Köln GmbH v. Bundesrepublik Deutschland*, Judgment, 18 January 2018, para. 21.

[38] CJEU: C-158/15, *Elektriciteits Produktiemaatschappij Zuid-Nederland EPZ NV*, opinion of Advocate General Juliane Kokott 3 March 2016, paras. 2–3, 13–19, 29–41, 44–45, 49, 52–60.

[39] CJEU: C-158/15, *Elektriciteits Produktiemaatschappij Zuid-Nederland EPZ NV*, Judgment, 9 June 2016, para. 41.

[40] CJEU: C-302/17, *PPC Power,* Judgment, 12 April 2018, para. 17.

[41] CJEU: T-57/11, *Castelnou Energía SL*, Judgment, 3 December 2014.

[42] CJEU: European Commission, Decision C (2010) 4499.

[43] Mucsi, G., Csőke, B. (2012): Power plant fly ash as valuable raw material. *Geoscience and Engineering*, 1, pp. 223–236.

[44] Mucsi, G., Debreczeni, Á., Mádai, V., Dudok, T., Csőke, B. (2011): Development of hydraulic binder using industrial wastes. *Journal of Silicate Based & Composite Materials*, 63, pp. 28–32.

Geosciences and Engineering, Vol. 7, No. 10 (2019), pp. 74–82.

HIGH-PERFORMANCE GEOPOLYMERS BY WET MILLING OF BLAST FURNACE SLAGS

T. MÜTZE – U. A. PEUKER

Institute of Mechanical Process Engineering and Mineral Processing, TU Bergakademie Freiberg

Abstract: For more than 100 years blast furnace slags have been used as additive material or substitute material in cementitious systems like mortar and concrete. Due to their different syntheses, the slag systems have binding properties which differ from conventional clinker. Some properties like limited heat generation and heat transfer due to a slow reaction kinetics are advantageous for certain applications. Other properties like low short-term strength of the corresponding concrete limit the use of blast furnace slags in applications like the pre-manufacturing of building parts.

With the help of mechanical activation due to fine grinding the properties of blast furnace slags can be shifted towards conventional clinker systems. A common blast-furnace slag cement was used to study the influence of the grinding regime in media mills on the binding properties of the corresponding cement. The grinding regime of conventional wet ball milling was compared to that of a planetary ball mill and a stirred media mill circuit. Since finely ground slag reacts with the process medium of water, several strategies have been tested to remove the process water as quickly as possible in order to evaluate the particle properties like specific surface area and size.

Fine grinding with the stirred media mill produced a hydraulic reactive material with similar properties as conventional clinker cement. The fineness of the material, which is described by the specific surface area, increased its reactivity. Nevertheless, the reactivity of the slag was still low enough that it can be processed in aqueous suspensions.

Keywords: *geopolymer, mechanical activation, blast furnace slag, stirred media mill, planetary ball mill*

1. INTRODUCTION

The application of secondary raw materials from anthropogenic high temperature processes in building material has a long tradition [1]. With proper processing of secondary raw material like slags and ashes it is possible to substitute cement [2, 3]. Some application properties even are improved due to the special properties and reaction behavior of the secondary raw materials. One example is the construction of large concrete structures like dams, which requires the slow reaction of slag-based concrete mixtures due to heat generation and heat transfer limitations. When combined with conventional cement in defined mixing ratios, slag- and ash-based concretes and mortars can be used in a broad field of building applications. Since the reactivity of cement as well as of secondary raw materials is a function of particle

size, comminution is the key to generate a sufficient amount of highly reactive fines. Furthermore ashes or slags can be chemically treatment to activate the silica structure. Typical modifiers and activators are sodium and potassium-hydroxide [4–7].

The relatively low reaction rate of secondary raw materials leads to several applications of ash and slag based concretes, especially if short-term strength of the concrete is necessary, e.g. for pre-manufactured parts. Beside chemical activation, mechanical activation is also possible. Mechanical activation can be due to size reduction and the increase in reactive particle surface or due to mechanical alteration of the internal crystal structure of the material. The latter determines the velocity of ionic or aqueous attack to the solids structure. The main problem of such a size reduction step for secondary raw materials derives from the field of operation of typical mills used in cement grinding. Conventional ball mills or roller mills are not suitable for generating ultrafine products. The alternatives are high-pressure grinding rollers (HPGR), vertical roller mills [8], or stirred media mills [9–11], which are known from pigment [12] and re-grinding applications.

2. MATERIALS AND METHODS

A common blast-furnace slag cement was used to study the influence of the grinding regime on the binding properties of the corresponding cement. The slag was produced by conventional ball milling *(Figure 2*: BM*)*. Particle properties like size and specific surface were measured in order to evaluate the process function. The particle size analysis utilized the laser diffraction system Helos (Sympatec, Clausthal-Zellerfeld, Germany) with either the dry dispersing system RODOS or with the wet dispersing system SUCELL. In order to avoid the hydration reaction in the wet dispersing mode, isopropanol was used as carrier liquid.

The comminution experiments used a planetary ball mill PULVERISETTE 5 (Fritzsch, Idar-Oberstein, Germany) and a lab scale stirred media mill Perl Mill (Draiswerke Mannheim, Germany). The planetary ball mill is a high energetic mill type, which promised both a small final particle size and an optional mechanical activation, due to the high energy milling mechanism. The stirred media mill is known for its capability to produce nano-sized materials [9, 13]. It is typically operated in wet mode, where a slurry is pumped through the grinding chamber. With a suitable size of grinding balls and a stabilizing physico-chemical milieu as well as with high specific energy input, it is possible to produce ultrafine particle systems.

The PULVERISETTE 5 has a milling chamber of 0.25 l volume and was operated at a media filling degree of 30%. The processing consisted of three subsequent grinding stages with different grinding balls *(*see *Table 1)* and used triethanolamine and diethylene glycol as grinding aids at a concentration of 0.02%. The Perl Mill *(Figure 1)* operated in a closed circuit with a mass concentration of the feed slurry $c_m = 0.3$. The grinding chamber was filled with ceramic balls *(*see *Table 1)* at a filling ratio of 60%.

Since finely ground slag reacts with the process medium water, especially during storage after comminution, several strategies have been tested to remove the process

water as quickly as possible and to preserve the material properties for analytics. The removal strategies included convective thermal drying, spray drying, filter cake washing with organic liquids (isopropanol or ethanol), and subsequent low temperature drying. The latter method proved to be sufficient to stop unwanted changes of the material properties and has been used for the experiments presented here (except for results shown in *Figure 5*).

Table 1

Grinding conditions in the planetary ball mill (PBM) and stirred media mill (SMM)

Equipment	Grinding stage	Grinding time in min	Grinding media	Diameter of grinding media in mm
PBM	1	30	Steel balls	10
	2	20		6–7
	3	20		1–2
SMM		15	Ceramic balls	1–1.6
		60		

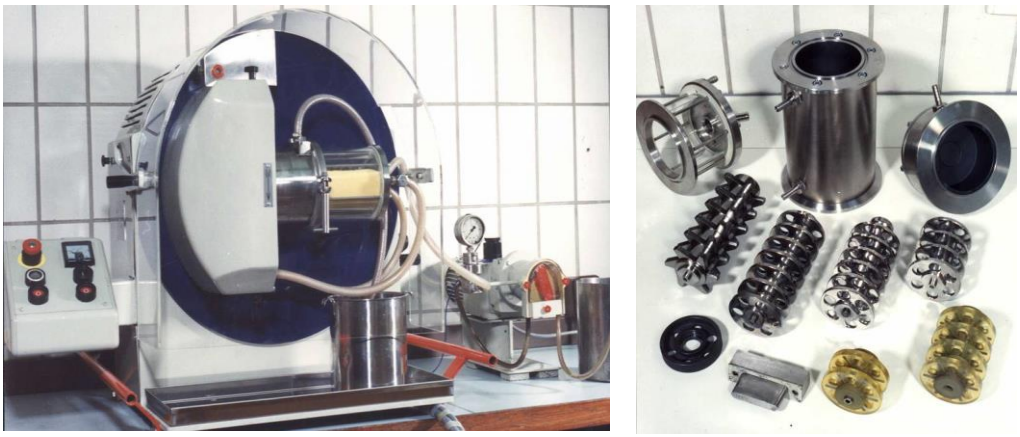

Figure 1

Left: Stirred Media Mill (SMM) type Drais Perl Mill, with a 0.75 l processing chamber; right: milling chamber and stirrer geometries

3. RESULTS AND DISCUSSION

The investigation of different types of fine grinding equipment showed that dry processing of the slag comes quickly to a grinding limit. At this limit agglomeration and breakage kinetic reach an equilibrium state and the particle size does not decrease further. The particle size distribution shows that the different concepts of fine grinding can be applied to blast furnace slags to produce superfine geopolymer material. The results of aqueous grinding of the blast furnace slag in the stirred media mill (SMM) demonstrate that the binding kinetic is sufficiently low. During one hour of

wet processing no gelation/binding could be observed. Nevertheless, it was necessary to remove the water after processing because longer contact times to water accelerated the binding reaction more and more.

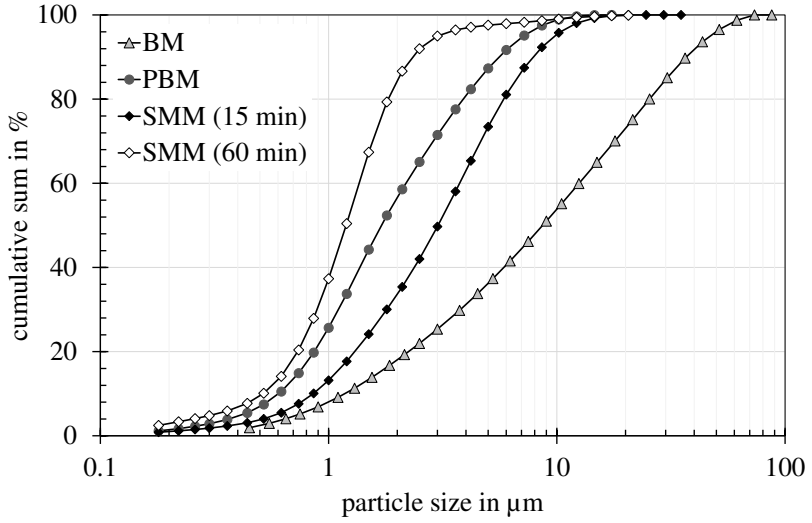

Figure 2

Particle size distribution of the feed material and grinding products (BM: ball mill product [feed], PBM: product of planetary ball mill, SMM: products of stirred media milling after defined grinding times)

Selected samples of the planetary ball mill and the stirred media mill were used in a mortar test *(Figure 3)*, which shows the relative compressive strength of a defined mortar sample as a function of the binding time. Characteristic values of this function are the ones after one day (1 d), two days (2 d) and 28 days (28 d). The last value corresponds approximately to the final strength. The one-day strength is relevant for the production of prefabricated parts.

The higher fineness of the finely milled material leads to increased compressive strength. The data is normalized to the compressive strength (28 d) of mortar produced with standard cement CEM. Both mortars which contain fine slag reach a higher final strength compared to pure CEM. The increase in final strength amounts to more than 10%. Even more relevant for the application of fine slag are the values of the compression strength after one day. After one day the stirred media mill product already reaches 80% of the final strength of the CEM, whereas the ball mill and planetary ball mill products are much weaker. Especially in comparison with the planetary ball mill product, the differences in strength do not derive from the final particle size distribution alone. During the milling chemical activation occurs due to the interaction between the silicates in the slag structure and the aqueous carrier fluid.

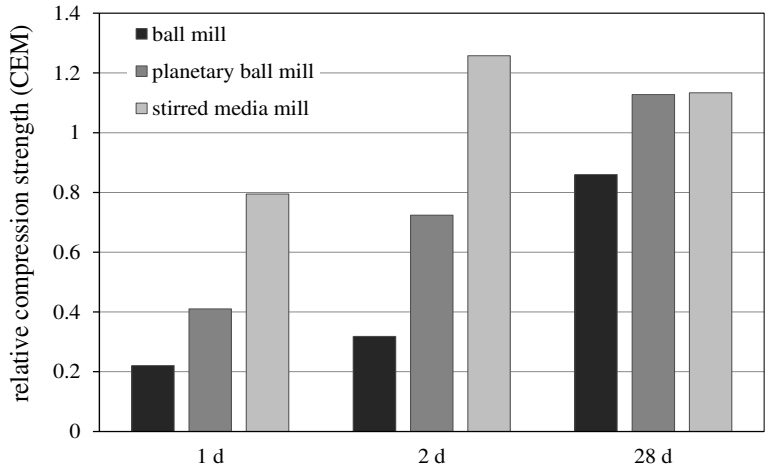

Figure 3

Compression strength of concrete manufactured of 50% CEM and 50% of milled slag fraction (testing according to DIN EN 12390-3) relative to 100% CEM

The increase of compression strength of the material depends on the reactivity of the hydraulic active component. The mechanical and chemical activation leads to a higher reactivity, which allows a faster reaction, which finally provides higher early phase compression strength (1 d). The reactivity becomes visible in the plot of the heat of reaction and heat of hydration respectively *(Figure 4)*, when differently processed slag materials are mixed with water and CEM.

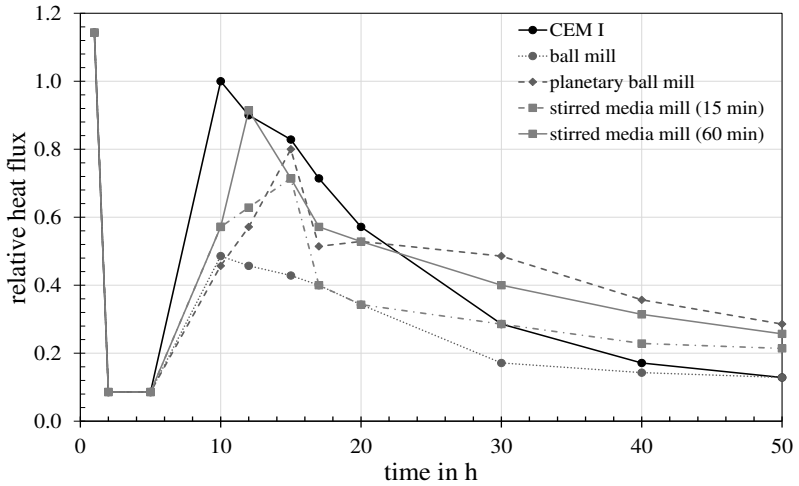

Figure 4

Heat flux of the hydration reaction of pure CEM compared to slag mixtures (50% fine blast furnace slag mixed with 50% conventional CEM, slag to water ratio 2:1)

The reference is the pure cement system "CEM". The transient heat flux shows an inhibition of about 5 h before the hydration reaction begins to start. The reaction itself shows a fast kinetic, which is comparable to the CEM system.

The maximum of the heat flux depends on the processing of the slag, which means the fineness and the chemical activation of the milled material. The finer the slag is, the closer the maximum comes to the data of the CEM system. The overall reactivity can be taken from the integral of the curves; the larger the integral area is the more binding occurs within the system. The area of the ball mill slag is smaller since the quite coarse material does not react completely. Also, the curves of the finely milled slags (planetary ball mill and stirred media mill) show longer-lasting reactivity. These systems have a significant heat flux in the period 20–50 h, which is even higher than that of the CEM system.

Thus the conventional processing provides a slow reaction kinetic, which explains the low compression strength after one day. The other slag fractions have been further processed with either the planetary ball mill as dry material or with the stirred media mill as aqueous suspension. For the stirred media mill two different milling times were investigated (15 and 60 min). These times are at least one order of magnitude smaller than the inhibition time of the hydraulic reaction shown in *Figure 4*. This explains why there is no significant setting of the reaction during the wet comminution and why a smooth replacement of the grinding environment from aqueous to organic (isopropanol) allows to study the particle characteristics of the grinding products.

Bringing all comminution data together, it becomes clear that an increase in fineness also increases the reactivity of the slag system. The inhibition time decreases and the initial heat flux as well as the overall heat flux become much higher. When looking at the integral of reaction heat, it can be stated that more CSH phases are formed in a shorter period. The increased processing time of the stirred media mill product, 60 min compared to 15 min, supports this finding, since the longer milling results in a finer product *(Figure 2)*. Furthermore, *Figure 5* illustrates that the specific surface of the slag system determines the mechanical properties of the final mortar system. This effect is more significant in the early stage (1 d and 2 d), where the difference in the strength amounts to a factor of three to four between a specific surface of 1 m^2/g to 6 m^2/g. The fine milling of slags therefore enables the application of the material where early stage strength is needed, e.g. for prefabricated parts.

The comminution of the slag material definitely consumes energy. Bringing together the data sets of different processing machines and concepts, they all follow the breakage law of the slag system which can be described by a power law *(Figure 6)*. The high quantity of mechanical energy which is needed to enhance the reactivity of the slag has to be counterbalanced with the saving of CO_2-emmissions during CEM production from limestone.

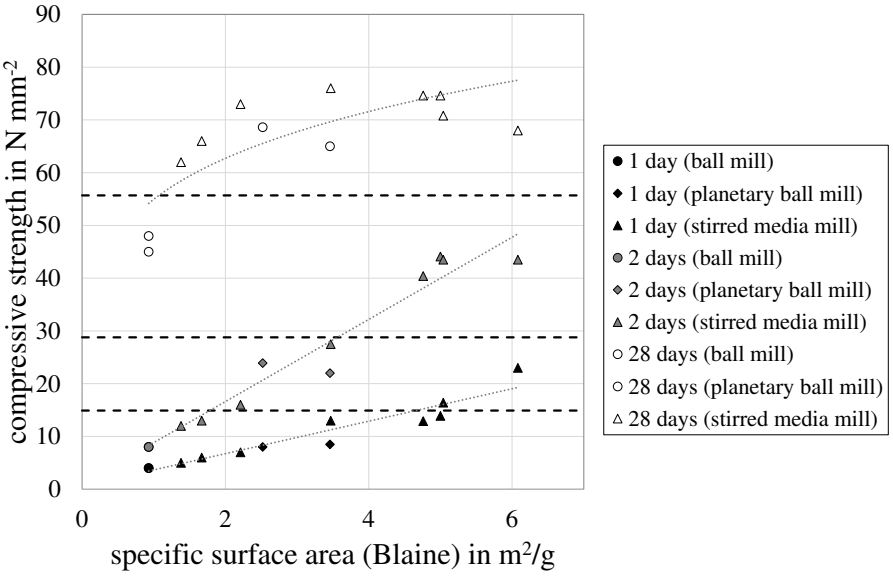

Figure 5

Compressive strength as a function of specific surface of the activated slag material for different milling strategies, measured in the system 50% slag and 50% CEM (dashed lines: pure CEM)

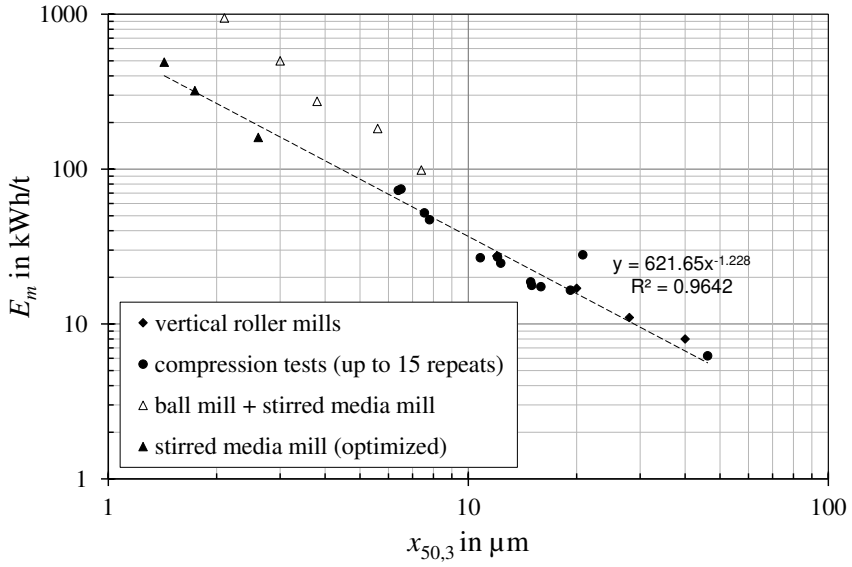

Figure 6

Comparison of comminution performance in terms of energy consumption (compression tests see [14, 15])

4. CONCLUSIONS

Fine milling with stirred media mills allows the production of a hydraulic reactive material from blast furnace slags, which has similar properties as conventional Portland cement. The fineness of the material, which is described by the specific surface, increases its reactivity. The reactivity of the slag is still low enough that it can be processed in aqueous suspension. For further application, the water has to be removed from the finely milled material, as was done in the lab-scale tests here. An alternative would be milling the slag directly prior to its application in the cementous system, thus to feed a (thickened) stirred media mills slurry in the mortar/concrete production process.

ACKNOWLEDGEMENTS

The authors would like to acknowledge the financial support from the Federal Government of Germany in the scope of the research project ECO-Zement (BMBF-No. 0327477 B).

REFERENCES

[1] Matthes, W., Vollpracht, A., Villagrán, Y., Kamali-Bernard, S., Hooton, D., Gruyaert, E., Soutsos, M., De Belie, N. (2018): *Ground granulated blast-furnace slag*. 25 Springer Netherlands.

[2] Ehrenberg, A. (2010): Current developments in the manufacturing and utilization of granulated blast furnace slag. *ZKG International*, 63, 3, pp. 52–66.

[3] Sekulic, Z., Petrov, M., Zivanovic, D. (2004): Mechanical activation of various cements. *International Journal of Mineral Processing*, 74, SUPPL., S355–S363.

[4] Ayturan, P., Tokyay, M. (2011): Alkali activation of granulated blastfurnace slag and fly ash. Ceramics – Silikaty, 56 2, pp. 168–176

[5] Tänzer, R., Ehrenberg, A., Stephan, D. (2012): Concrete based on alkali-activated granulated blast-furnace slag (Part 2). *Betonwerk Fertigteil Tech*, 78 4, pp. 44–57.

[6] Tänzer, R., Ehrenberg, A., Stephan, D. (2012): Concrete based on alkali-activated granulated blast-furnace slag (Part 1). *Betonwerk Fertigteil Tech*, 78, 3, pp. 25–33.

[7] Tomková, V., Ovčačík, F., Vlček, J., Ovčačíková, H., Topinková, M., Vavro, N., Martinec, P. (2012): Potential modification of hydration of alkali activated mixtures from granulated blast furnace slag and fly ash. *Ceram Silikaty*, 56, 2, pp. 168–176.

[8] Weimar, H., Wulfert, W., Ludwig, H. M., Moser, B. (2017): Mobilization of the hydraulically active phases in LD slags by producing ultrafine material. *Cement International*, 15, 4, pp. 76–86.

[9] Mende, S., Stenger, F., Peukert, W., Schwedes, J. (2004): Production of submicron particles by wet comminution in stirred media mills. *J. Mater. Sci*., 39, 16–17, pp. 5223–5226.

[10] Ohenoja, K., Breitung-Faes, S., Kinnunen, P., Illikainen, M., Saari, J., Kwade, A., Niinimäki, J. (2014): Ultrafine grinding of limestone with sodium polyacrylates as additives in ordinary portland cement mortar. *Chem. Eng. Technol.,* 37, 5, pp. 787–794.

[11] Stenger, F., Mende, S., Schwedes, J., Peukert, W. (2005): The influence of suspension properties on the grinding behavior of alumina particles in the submicron size range in stirred media mills. *Powder Technology*, 156, 2–3, pp. 103–110.

[12] Flach, F., Breitung-Faes, S., Kwade, A. (2018): Model based process optimization of nanosuspension preparation via wet stirred media milling. *Powder Technology*, 331, pp. 146–154.

[13] Schäfer, M., Peuker, U. (2016): Grinding of Porous Ion Exchange Particles. *Chemie-Ingenieur-Technik*, 88, 5, pp. 616–621.

[14] Mütze, T. (2014): Modeling of the stress behavior of confined particle beds. *Chemie-Ingenieur-Technik*, 86, 6, pp. 814–820.

[15] Mütze, T. (2015): Energy dissipation in particle bed comminution. *International Journal of Mineral Processing*, 136, pp. 15–19.

Geosciences and Engineering, Vol. 7, No. 10 (2019), pp. 83–93.

THEORETICAL MODELS FOR AIRFLOW SEPARATORS TO PROCESS MUNICIPAL SOLID WASTES

ROLAND RÓBERT ROMENDA

PhD student
Institute of Raw Material Preparation and
Environmental Processing, University of Miskolc
Hungary, 3515 Miskolc-Egyetemváros, ejtrom@uni-miskolc.hu

Abstract: Airflow devices have a significant role in the mechanical-physical and mechanical-biological processing of wastes. This role will continue to grow in the future due to the EU's "circular economy" strategy. Here a theoretical methodology for the process engineering design of a nozzle airflow device is discussed, which is based on separation and fundamental air jet tests with model airflow equipment. A consortium led by 3B Hungary Ltd. designed and manufactured the industrial prototype of the KLME (combined airflow, magnetic and electrical) separator, including the nozzle airflow separator unit designed by the introduced methodology.

Keywords: *residual fraction of municipal solid waste (RMSW), airflow separator, environmental processing, waste processing*

1. INTRODUCTION

According to the circular economy strategy of the European Union (EU), the recovery of the waste materials as secondary raw materials and energy sources is a priority, preferable to the other non-favorable options such as deposition. The EU member states have made significant progress in this area, which is illustrated in *Figure 1* [13].

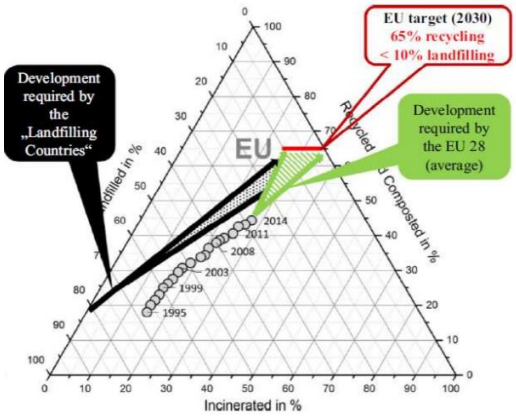

Figure 1
European (EU 28) waste management performance development, 1995–2014 [13]

The three basic options of waste treatment – recycling and composting, incineration, and deposition – are used by member states in different proportions, depending on their infrastructure and technological capability. At any given point on the ternary diagram in *Figure 1* the sum of the percentages of the three waste treatment methods is always 100%. It can be seen that in 1995, large groups of countries typically applied only landfilling, while the ratio of recycling and incineration was around 30%. By 2014, the countries had split into three parts. Typically, the so called "landfilling" countries still landfilled almost 100% of their waste. Among the "developing" countries, Hungary landfilled 60%, incinerated 10% and recycled-composted about 30%. In the "developed" countries group landfilling had dropped practically to 0%, and recycling-composting had increased up to 40–60%. [13]

According to Directive 2008/98/EC, 2015/0275 (COD), by 2030 the gradual reduction of landfilling down below 10% and the increase of recycling and composting above 65% have been targeted for all generated municipal solid wastes. This is a very serious challenge even for the "developed" countries, not to mention for the "landfilling" and "developing" countries!

In Europe, the most widely used concept is mechanical and/or biological pretreatment. This method reduces the environmental impact when the residual fraction of municipal solid waste (RMSW) is finally disposed of in landfills [17]. The main problem with this technology is the variedness of RMSW, which means a universal processing plant cannot be used. Every type of this method usually starts with a sorting step, like a trommel screen. Next, a shredder or different type of separators followed [15]. Finally, the degradable fine biofraction can be composted to reduce the mass, volume and biological hazard of the waste [13].

There are three main types of technologies, Mechanical-Biological Stabilization (MBS), Mechanical-Physical Stabilization (MPS) and Mechanical-Biological Treatment (MBT) [14]. The MBS and MPS technologies both use the same steps to treat the solid waste – shredding, metal sorting and screening. The only difference between the two technologies is the biological treatment. While physical treatment uses only drying technologies after metal sorting, MBS uses aerobic or anaerobic digestion to stabilize the organic components in the residual municipal solid waste [8, 16]. Mechanical-Biological Treatment is more complex than the previous methods because after shredding the waste is divided in two fractions by a trommel screen (50–80 mm). The fine fraction goes to biological treatment while the coarse fraction is treated with mechanical methods to make recyclable products and Refuse-Derived Fuel (RDF) [12].

Nearly 50% of municipal solid waste is still landfilled in Hungary today, although major improvements have been made over the past period. There has been a significant improvement in the collection of wastes: the selective collection of green wastes and of packaging materials have been introduced. In many places mechanical-physical and mechanical-biological processing plants have been built for the preparation of residual fraction of MSW. Such plants have been installed in Vaskút, Polgárdi, Pécs, Miskolc, Győr, etc. [1]. The newest plant is the recently commissioned Zalae-

gerszeg plant, which is supplied by equipment almost entirely developed and manufactured in Hungary (with the exception of the final rotary shredder) and where the Institute of Raw Materials Preparation and Environmental Processing, University of Miskolc was the scientific partner. If there is a biological treatment, there are such in Pécs and Győr that treatment is still only an aerobic stabilization, which reduces the volume of the landfilled waste, but the energy generated from the degradation is wasted [3, 5, 9].

On the basis of the above, it can be concluded that if Hungary would like to achieve the targets set out in Directive 2015/0275 (COD), it has to increase the enrichment ratio of the valuable substances separated from the residual MSW for material recycling. It can be seen that airflow systems have a key role to play in this because these devices divide the main waste flow into smaller ones, which then can be more efficiently processed by sensor based sorters.

The principle of separation in air flow units is based on the different terminal settling velocity of the particles or their different initial acceleration. There are different kinds of devices for separating paper, cardboard and plastic wastes (counter current-flow and cross-flow air separators) in the industry, and air streams are also used in many other devices, for example, in optical separators where nozzles blow out the selected particles by air jet.

In 2016, the project *Development of new equipment for domestic production of residual municipal solid wastes for small and medium-capacity technological systems* was started. The consortium, led by 3B Hungary Ltd. with the scientific partner Institute of Raw Materials Preparation and Environmental Processing, University of Miskolc, developed a new type of waste processing equipment called the KLME separator (the name KLME is the Hungarian abbreviation of 'combined magnetic, electric and air flow'). The feed into the KLME is the coarse fraction (>60 mm) after the drum sieve and it has five product streams. The most critical element in the development of the machine was the development of the air-flow separators, because it determines the downstream processing of the wastes [7].

2. PROCESS ENGINEERING DESIGN OF AIRFLOW SEPARATORS

Many design forms and types of airflow devices are commercially available (e.g. from Nihot, Westeria, etc.). Nevertheless, the literature contains little information about the design of the airflow separators. In this project, in addition to the theoretical work, model air flow separators have been manufactured and systematic particle settling tests have been carried out. The KLME separator contains an air-nozzle separator (3D) and a foil cage (2D) separator. For the separator design, three basic tasks were studied: the phenomenon of particle settling in quiescent air; the separation characteristics of model nozzle air flow apparatuses as two-product separators; and the nozzle design. A method for the measurement of particle settling when particles are dropped from a height has been developed. According to this method, particles are dropped in a building with a high ceiling, the motion is recorded with a camera

and the time–velocity diagram is determined by image analysis [14]. The investigation results of particle settling are not described here.

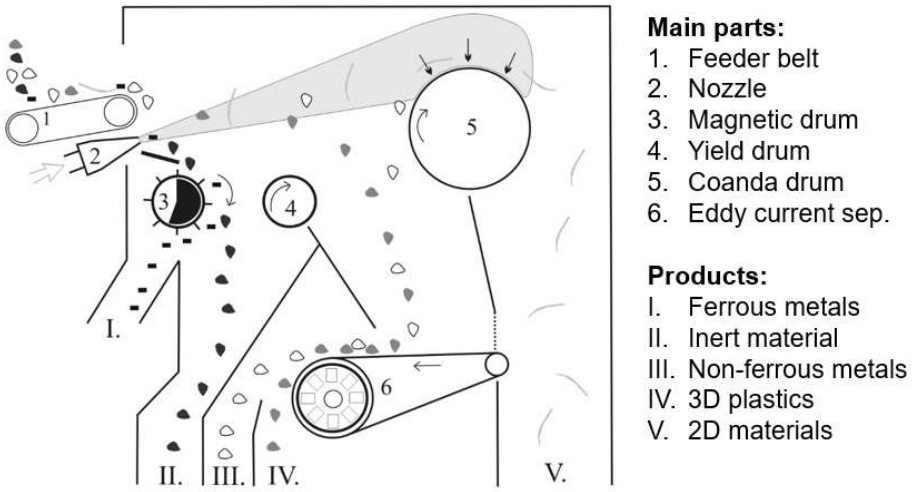

Figure 2
Combined Airflow, Magnetic and Electrical (KLME) separator schematics

The terminal settling velocity and the initial acceleration (relaxation time) of a given particle or particle size fraction are the most important data for the technical design of airflow separators. In the case of spherical particles, the calculation of the terminal settling velocity is well known in the literature [4, 6], so it is not specified here, but there is any literary data for the initial acceleration. Based on Newton's law of motion, it can be stated:

$$a_o = \frac{G - F_A}{m} = \frac{\rho_s \cdot V \cdot g - \rho_f \cdot V \cdot g}{\rho_s \cdot V} = g \cdot \left(1 - \frac{\rho_f}{\rho_s}\right) \tag{1}$$

where: a_0 – initial acceleration
G – gravitational force
F_A – aerodynamic force
m – mass of the sample
ρ_s – density of the sample
ρ_f – density of the fluid
V – volume of the sample
g – gravitational acceleration.

It can be seen that in the case of spherical particles, the ratio of the density of the medium (ρ_f) and the particle (ρ_s) causes smaller initial acceleration of the settling particles than the gravitational acceleration. Particle shape strongly influences this phenomenon. So far, there are no theoretical models to calculate even the terminal settling velocity of non-spherical particles in the literature, rather a gap exists regarding the relaxation time (initial acceleration). The measuring results obtained with particles of regular shape and real waste particles were used here. The initial acceleration can be determined by the derivation of the motion function and the substitution of t = 0. The derivative of the tangent hyperbolic function is the reciprocal cosine hyperbolic square function: ch (0) = 1.

$$v'(t) = a = v_o \cdot \frac{1}{t_R} \cdot \frac{1}{ch^2(t)} \qquad a_o = \frac{v_o}{t_R} \qquad \text{(2a, 2b)}$$

where: v'(t) – first derivate of velocity
a – acceleration
a_0 – initial acceleration
v_0 – terminal settling velocity
t_R – relaxation time
t – current time.

Equation 2b was recognized on the basis of the measured results and it is also confirmed by this derivation. From this equation it is apparent that the relaxation time parameter t_R is very important and yet it is hard to find in the literature. By comparing *Equations 1* and *2b* the measured results can be checked. The largest measurement uncertainty is caused by the measurement of the volume of irregularly shaped waste particles, but according to the developed method the measurement of v_o and t_R is reliable.

The shape factor (SF) of non-spherical particles is calculated using *Equation 3b* as the ratio of the measured terminal settling velocity of the non-spherical particle and the calculated terminal settling velocity of the volume-equivalent diameter (x) virtual particle (3a):

$$x = \sqrt[3]{\frac{6 \cdot V}{\pi}} \qquad SF = \frac{v_o}{v_{ox}} \qquad \text{(3a, 3b)}$$

where: x – volume-equivalent diameter
V – volume of sample
SF – shape factor
v_0 – measured terminal settling velocity
v_{0x} – calculated terminal settling velocity of volume-equivalent sphere.

The defined shape factor was calculated for each examined particle [10]. It was found that according to the presented method, the parameters of v_o, a_o, and t_R can be calculated for any spherical particles of diameter 70–150 mm. In the case of waste particles, the shape factor has to be measured, e.g. with the new presented method. In the case of similar particles to the measured ones, we can calculate all parameters that can be used for the design of the air flow separator using the semi-empirical shape factor.

One of the basic processes of mechanical processing is the separation phase. To characterize a two-product separation process, the Tromp function can be used to show which percent of a given particle fraction is separated into the given product. In the case of the nozzle air flow separator under construction, the yield of wastes into a product, namely the Tromp value [T (v)] is a function of the air jet velocity in the throat of the nozzle. *Table 1* shows the Tromp functions used to characterize airflow separation.

Table 1

Tromp functions which can be used to characterize airflow separation

Linear	$T(v) = m \cdot (v - v_c)$
Rosin-Rammler	$T(v) = 1 - \exp\left(-\ln 2 \cdot \left(\frac{v}{v_c}\right)^m\right)$
Schumann-Gaudin	$T(v) = 0{,}5 \cdot \left(\frac{v}{v_c}\right)^m$
Arcus tangent (at)	$T(v) = \frac{1}{\pi} \cdot \mathrm{at}\left[m \cdot (v - v_c)\right] + 0{,}5$

Among the functions given in *Table 1*, the Rosin–Rammler function and the arcus tangent can be applied in the range of 0 to ∞ m/s [2], while the linear and Schumann–Gaudin functions are defined only between a minimum and a maximum jet speed. For lower speeds than the minimum speed, separation yield is 0, while for higher speeds it is 1. For each function the cut parameter (v_c) is determined by 50% separation yield, and the parameter m is characteristic of the separation sharpness. At present, there is no known correlation to theoretically calculate the Tromp function of a given air flow separator, so measurements should be carried out either with a particular industrial machine or model air flow separator.

2.1. Theoretical model for selecting the main parameters of air flow separators

Let us look at the following phenomena to characterize the separation of an airflow unit. The air jet is coming out from an H wide and B length nozzle with α angle and v_1 velocity. At moment t = 0, place a cube-shaped particle directly into the nozzle throat and examine the initial acceleration according to the previously described phenomena. The shape of the cubic particle in the direction of the air stream should be square, marked with "X" for simplicity and comparability. If the particle is larger than the air jet thickness, the impulse force of the air stream affects the particle in the axis of the airflow *(Figure 3)*. The air stream reaches the H · X surface. At the moment of launch, the sum of the forces is the impulse force, minus the gravitational force, subtracted with the buoyancy component in the airflow axis line. From our point of view, the impulse force is the determinative force:

$$F_i = \dot{m} \cdot v_1 = H \cdot X \cdot \rho_f \cdot v_1^2 \tag{4}$$

where: F_i – impulse force
$\dot{m}$ – mass flow rate
v – velocity of air stream
H – width of air stream
X – particle size
ρ_f – density of the fluid.

In the case of particles smaller than the width of the air stream, the phenomenon is different. The air flows around the particle and due to the well-known surface friction and surface pressure distribution an air drag force awakens. The model is shown in *Figure 4*.

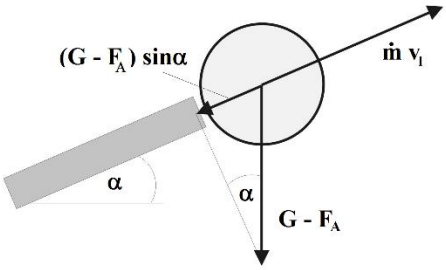

Figure 3
Impulse model for initial acceleration

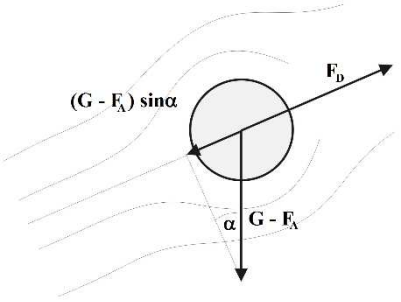

Figure 4
Drag model for initial acceleration

The mentioned drag force is the decisive factor, which can be written in *Equation (5)*. The X · X surface is perpendicular to the axis of the air jet:

$$F_D = \frac{1}{2} \cdot C_D \cdot X \cdot X \cdot \rho_f \cdot v_I^2 \tag{5}$$

where: F_D – drag force
C_D – drag coefficient
X – particle size
v_I – velocity of air stream
ρ_f – density of the fluid.

The ratio of the two forces can be written:

$$\frac{F_I}{F_D} = \frac{2 \cdot H}{C_D \cdot X} \tag{6}$$

This ratio is approximately 0.9 if the particle is a 150 mm cube and the nozzle thickness is 30 mm. The drag coefficient C_D is significantly affected by the particle shape. If we simplify the 3D separator unit of the KLME separator (nozzle airflow device) as an airflow separator, then the B length and H nozzle width is the surface through the air flows out with v_l velocity. For continuity, it can be written:

$$v_l = \frac{\dot{Q}}{B \cdot H} \tag{7}$$

where Q is airflow volume.

Imagine that we launch a particle from the worst place. This point is the upper edge of the inlet cross section. Let us assume that the particle moves horizontally with v_l velocity, while vertically it settles because of gravity. Therefore, the horizontal speed and the travelled distance (length L) are directly proportional to the vertical speed and the vertically travelled distance:

$$\frac{v_l}{v_o} = \frac{L}{H} = \frac{\dot{Q}}{B \cdot H \cdot v_o} \tag{8}$$

This gives the length of the airflow separator, because the height is simplified out from the equation.

$$L = \frac{\dot{Q}}{B \cdot v_0} \tag{9}$$

3. INDUSTRIAL APPLICATION

Based on the particle settling tests, the separation yield examinations on the model airflow separators and the presented theoretical airflow design model, the consortium led by 3B Hungary Ltd. designed and manufactured the industrial KLME separator prototype. This separator is part of the mechanical-physical waste preparation

plant in Zalaegerszeg-Búslakpuszta, which was the first, almost entirely domestic manufactured system inaugurated on 14th July, 2018. *Figure 4* shows a photograph of the industrial KLME separator.

Figure 5
The industrial size KLME separator

4. CONCLUSION

Earlier studies have found that there are two different physical phenomena in air separation, depending on the ratio between the thickness of the air stream and the particle size. These two different phenomena fundamentally determine the design of airflow devices. If Hungary wants to approach the 2015/0275 (COD) EU directive in the near future, it will have to substantially increase the amount of substances prepared (separated) from residual MSW that can be material recycled. This will require separation and sorting equipment based on airflow systems and sensors. I developed a theoretical method for determining the technical dimensions of the nozzle air flow apparatus, which can be used to determine the main dimensions of the machine. Separation tests on model airflow separators and fundamental particle settling experiments are still required for the design of such a machine because of the heterogeneous nature of RMSW particles.

ACKNOWLEDGEMENT

The described work was carried out as part of the EFOP-3.6.1-16-2016-00011 *Younger and Renewing University – Innovative Knowledge City – institutional development of the University of Miskolc aiming at intelligent specialisation* project implemented in

the framework of the Széchenyi 2020 program. The realization of this project is supported by the European Union, co-financed by the European Social Fund.

REFERENCES

[1] Bokányi L., Csőke B., Gombkötő I., Nagy S., Pintér-Móricz Á. (2018): „Hulladékból Energia" Kutatások a ME Nyersanyagelőkészítési és Környezeti Eljárástechnikai Intézetében. *Műszaki és Menedzsment Tudományi Közlemények*, 3, (1), pp. 49–57.

[2] De Lange, T., Venter, P. E. (1987) The use of simulated Tromp partition curves in developing the flowsheet of plant extensions at Grootegeluk Coal Mine. *APCOM 87. Proceedings of the Twentieth International Symposium on the Application of Computers and Mathematics in the Mineral Industries*, Volume 2: Metallurgy. Johannesburg, SAIMM, pp. 295–311.

[3] Faitli, J., Magyar, T. (2014): Optimizing the Operation of Municipal Solid Waste Landfills. In: Gombkötő, Imre (ed.): *18th International Conference on Waste Recycling*, Miskolc, pp. 1–9.

[4] Faitli J. (2015a): Szemcsemozgás mérése és számítása nem-newtoni egy- és többfázisú közegekben. *Bányászati és Kohászati Lapok – Bányászat*, 2015/3., pp. 2–9.

[5] Faitli, J., Erdélyi, A., Kontra, J., Magyar, T., Várfalvi, J., Murányi, A. (2015b): Pilot Scale Decomposition Heat Extraction and Utilization System Built into the "Gyál Municipal Solid Waste Landfill". In: Cossu, R., He, P., Kjeldsen, P., Matsufuji, Y., Reinhart, D., Stegmann, R. (eds.): *15th International Waste Management and Landfill Symposium: G13*. Workshop: Heat utilization from landfills. S. Margherita di Pula, Italy, Paper 262. p. 12.

[6] Faitli, J. (2017): Continuity theory and settling model for spheres falling in non-Newtonian one- and two-phase media. *International Journal of Mineral Processing*, 169, (1), pp. 16–26.

[7] Faitli, J., Csőke, B., Romenda, R., Nagy, Z., Németh, S. (2018): Developing the combined magnetic, electric and air flow (KLME) separator for RMSW processing. *Waste Management & Research*, 36, 9, pp. 779–787., 9 p.

[8] Fei, F., Wen, Z., Huang, S., Clercq, D. D. (2018): Mechanical biological treatment of municipal solid waste: Energy efficiency, environmental impact and economic feasibility analysis. *Journal of Cleaner Production*, Volume 178, pp. 731–739.

[9] Magyar, T., Faitli, J. (2016): Temperature Distribution Measurements in the Gyál MSW Landfill. *Inzynieria Mineralna*, 38, (2), paper IM 2-2016-a22. p. 8.

[10] Nelles, M., Morscheck, G. and Grünes, J. (2012): MBT in Germany and Europe, development, status and outlook. *International 9th ASA Recycling Days*

MBT as a Supplier of Secondary Raw Materials, Hannover, Germany, 29 February–2 March 2012, pp. 1–16.

[11] Pace, S. A., Yazdani, R., Kendall, A., Simmons C. W., VanderGheynst, J. S. (2018): Impact of organic waste composition on life cycle energy production, global warming and Water use for treatment by anaerobic digestion followed by composting. *Resources, Conservation and Recycling*, Volume 137, pp. 126–135.

[12] Połomkam, J. and Jędrczak, A. (2019): Efficiency of waste processing in the MBT system. *Waste Management*, Volume 96, pp. 9–14.

[13] Pomberger, R., Sarc, R., Lorber, K. E. (2017): Dynamic visualisation of municipal waste management performance in the EU using Ternary Diagram method. *Waste Management*, 61. pp. 558–571.

[14] Romenda R. R., Faitli J. (2017): Egyedi hulladékszemcsék instacioner és stacioner mozgásának vizsgálata nyugvó levegőben. In: Kékesi Tamás (szerk.): *MultiScience – XXXI. microCAD International Multidisciplinary Scientific Conference*, Magyarország, Miskolci Egyetem, pp. 1–9.

[15] Siddiqui, A. A., Richards, D. J. and Powrie, W. (2013): Biodegradation and flushing of MBT wastes. *Waste Management*, Volume 33, Issue 11, pp. 2257–2266.

[16] Thiel, S., Thomé-Kozmiensky, J. K. (2010) Mechanical-biological pretreatment of waste, Hope and reality. *Papers and Proceedings of the ISWA World Congress 2010 – Urban Development and Sustainability – a Major Challenge for Waste Management in the 21th Century*, Hamburg, Germany15–18. November 2010, pp. 1–16.

[17] Trulli, E., Ferronato, N., Torretta V., Piscitelli, M., Masi, S., Mancini, I. (2018): Sustainable mechanical biological treatment of solid waste in urbanized areas with low recycling rates. *Waste Management*, Volume 71, pp. 556–564.

Geosciences and Engineering, Vol. 7, No. 10 (2019), pp. 94–104.

MEDICAL ASSESSMENT OF PATIENTS RELATING TO CAVE THERAPY IN LILLAFÜRED IN THE BÜKK MOUNTAINS

ELEONÓRA JUHÁSZ[1] – ADRIEN MUNKÁCSI[2] – LÁSZLÓ LÉNÁRT[3] – ÁGNES PAPP[2] – EMŐKE KISS-TÓTH[1] – ANDREA LUKÁCS[1]

[1]*Faculty of Healthcare, University of Miskolc, Miskolc*
[2]*Borsod-Abaúj-Zemplén County Central Hospital and University Hospital, Miskolc*
[3]*Faculty of Earth Science and Engineering, University of Miskolc, Miskolc*
Eleonóra Juhász, 3515 Miskolc-Egyetemváros, efklandi@uni-miskolc.hu

Abstract: Climate conditions used in rehabilitation prevail in the Lillafüred Thermal Baths. The purpose of our present study is to analyse the suitability of cave therapy for prospective users by means of simple physiotherapeutic methods and parameters. The study was conducted at the Department of Respiratory. Rehabilitation at Borsod-Abaúj-Zemplén County Central Hospital and University Hospital in patients with COPD or bronchial asthma. One of the two groups of patients received cave therapy, while the control group did not. As an objective parameter, we determined the deviation from the ideal body weight, examined the spinal physiological curvature and specified the chest mobility. We gathered information about the endurance of the patients using the 6-minute walking test and measuring the voluntary apnoea time. The presence of ischemic heart disease was also investigated in the patient documentation. The patients' perceived health was measured using the SF-36 questionnaire. For comparison of the groups two-sample Student t-test was applied, in the case of discrete distribution variables we used Pearson's χ 2 -test. In the 'Cave group' we examined 30 patients (9 men and 21 women, mean age 60.33 ± 6.62 years), and 16 patients in the contraindicated group (6 men and 10 women, mean age 66.4 ± 7.22 years). There was only a tendency in the presence of the observed comorbidity ($p = 0.061$). In the walking test, the 'Cave group' was significantly better ($p < 0.001$). The majority of the patients in both groups were overweight, had reduced chest mobility, and incorrect body position. Our physiotherapeutic assessment methods objectively showed the difference between the groups of patients indicated for speleotherapy and those who were not indicated. The results reveal that it is crucial to eliminate patients who cannot be exposed to the pathway to the cave therapy room and it must be decided whether speleotherapy is recommended or contraindicated, and, in addition, that no clear contraindication scheme exists: the decision is always made on an individual basis.

Keywords: *cave therapy, health status, respiratory patients, contraindication*

1. INTRODUCTION

The rehabilitation of breathing is an important part of the treatment of patients with chronic respiratory diseases. It alleviates the symptoms, improves condition and motor coordination, permits the patient to move more, with less sensation of shortness of breath associated. Chronic obstructive pulmonary disease (COPD) is charac-terised by

slowly and gradually worsening functional disorder which is predominantly irreversible. It is a systemic disease usually followed by several concomitant diseases. Obstruction is reversible in many cases of bronchial asthma (Pocket Guide to COPD Diagnosis, Management, and Prevention, 2017). The natural course of COPD is characterised by a (usually progressive) decrease of respiratory reserves. In contrast to an annual decrease of 20–30 ml of FEV 1 (the quantity of the air exhaled in the first second of forced expiration) which is regarded a normal physiological change, this value may reach 60–80 ml in COPD.

Curative climate is an important component, and especially, an optimal environment for the respiratory rehabilitation applied in respiratory diseases. Its implementation requires expertise and hospital background including appropriate examination methods, equipment and personnel (Horváth, 1984). Patients arrive in our town from all points of Hungary, and, following a health check, they are placed in a complex curative respiratory rehabilitation programme on the basis of appropriate criteria (Magyar, 2006). One of the "health caves" in Hungary is the Szent István Cave in Lillafüred. In addition to speleotherapy performed in its Fekete-terem, the programme includes drug therapy, patient education, and physiotherapy. However, the programme may only include staying in the health cave if the patient is fit enough to get to the curative room and back.

The purpose of this paper is to introduce the cool karst cave climate as a therapeutic venue with the help of the relevant literature. An additional purpose is to analyse the background of the fitness of patients for the cave therapy, by determining parameters characteristic of chronic respiratory diseases and conditions which can be assessed using simple methods of physiotherapy.

2. Applicability of cool karst cave rooms for cave therapy

In the cave systems, the substrate rock, together with the sediments and sometimes water surface, fully encloses the air, except for an opening to the surface. According to studies, the most suitable rooms for medicinal purposes are medium-sized rooms which are far from the opening of the cave and have a balanced climate (Fodor, 1981). Each cave contains air with unique, characteristic qualities. Constant and ephemeral horizontal underground water courses are important factors in the case of a therapeutic cave, as such water courses convey part of both gaseous components and speleoaerosol. The vertically leaking or dripping water and the cave creeks feeding on karst water influence the air temperature in the cave, as well as the creation and maintenance of a balanced state (Fodor, 1981; Roda & Rajman, 1975).

The absolute water vapour content of the air in the cave is lower than that of the outside air in the warmer seasons. Owing to that, one feels cold relatively seldom, evaporation from the body surface is minimal, and breathing becomes deeper (Mucsi & Mucsi, 1987). One of the reasons why comfort improves is that, while the inhaled cold cave air is warmed up to 28–30 °C in the nose, its relative humidity decreases to 30–33%. That is, it gets drier, so it can absorb water in the lower airways.

The reduction in the respiratory secretion is what one perceives as relief. The temperature of exhaled air is 35–36 °C, i.e. each m 3contains 39–42 g water. Taking away the water content (9.3 g/m^3) of inhaled air from the water content of exhaled air, we find that 30 g water leaves the organism with every m^3 of air. That means losing 20 g water per hour through the airways. By comparison, one can lose 5–7 g water per hour while using the air of a city (Fodor, 1975; Fodor, 1981).

The cave as well as its outer surface and cover should meet certain criteria. Criteria for the surface: in general the cave should be easy to access, its entrance should not be situated higher than its environment, and at least half of its environment should be covered with a forest. As regards underground factors, air flow is of priority importance. The cave must not be subject to draft; the cycle of complete exchange of air is 6 to 16 hours in an optimal cave, because in that range the value of the curative components can remain constant. Another highlighted factor is the mean temperature, which should be about 10 °C. High relative humidity (95–100%) is also a condition of the therapy. The presence of vertically seeping waters is an indispensable condition of the development of high relative humidity, and the intensity of such infiltration has an effect on the ratio of negatively charged ions in the air. As regards curative factors, measuring the carbonic acid content and the quantities of constant biochemical components is also important because these are parts of the aerosol formed. Further, the air or the waters in the cave must not contain substances which are harmful to the human organism. Cave creeks and subsoil waters must not put the patients' bodily integrity at risk (Roda & Rajman, 1975). The cave corridor may only be used for cave therapy if it is declared as static, and its horizontal air flow rate should not exceed the 15 cm/sec value. Such airflows will not cause a draught or change the constant values of the curative components in the air (Fodor, 1981, Roda & Rajman 1975). It is important from biological aspects that most of the chemical components of the cave air are also parts of the speleoaerosol. As regards key source gases, the composition of the cave air is almost identical with that at the surface (Fodor, 1981). Regarding the so-called trace constituents, however, there are significant differences between the cave air and atmospheric air masses. The aerosol content is genetically characteristic of the quality of the air in the cave studied, and influences the efficiency of a health cave. Carbon dioxide plays important morphogenetic and bioclimatological roles in the cave. One of its highlighted biological functions is that it increases the intensity of reathing, it may increase respiratory volume by 1 to 1.5 litres. The volume-to-volume ratio of carbon dioxide in most caves is significantly different from that in the atmospheric air; on average, it is 15 times higher than that (Gádoros, 1989; Karlowits & Varga, 2001).

Radioactivity in the cave air is relatively strong, but it does no harm to health; on the contrary, its local effect on the mucous membrane is mentioned by several authors (Géczy, 1989).

3. THE SZENT ISTVÁN DRIPSTONE CAVE AS A HEALTH CAVE

The corridors and rooms of Szent István Cave in Lillafüred *(Figure 1)*, which is a specially protected cave, are available to visitors in a total length of 230 m. An additional adapted section of approximately 50 m is the Fekete-terem, with the Bányatáró leading to it *(Figure 2)*. This is the last member of the system of adapted halls, and has been used for the purposes of respiratory therapy since 1990.

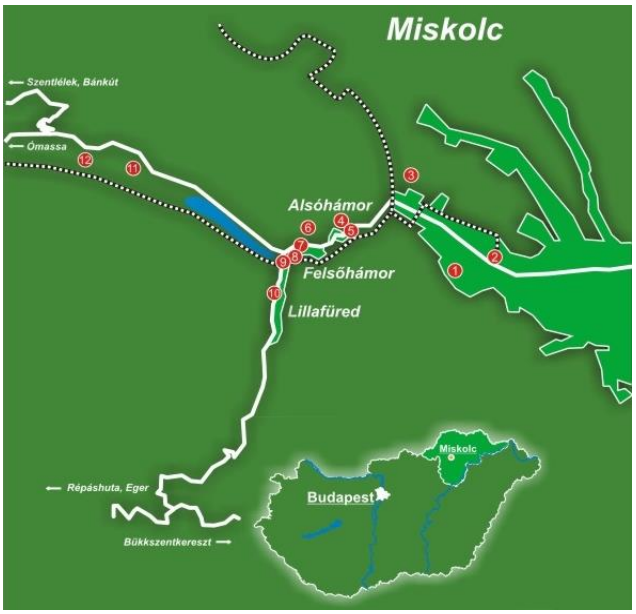

Figure 1
Location of the Szent István Cave in Lillafüred

The rock embedding the cave is karstifiable limestone from the mid-Triassic epoch (Fehérkő Limestone Formation). Regarding its genetics, the cave is a spring cave. The results published by Gyula Szabó (1963), who studied the meteorological circumstances in Szent István Cave, show that the artificial passage after the entrance is exposed to a constant draught, so the temperature here follows the changes at the surface. The amount of fluctuation decreases as one progresses to the inner parts of the cave, and a constant temperature of 9.4 °C may be measured in the Tordai-hasadék. When the entrance is open, an air flow of a speed of 3 to 12 m/minute forms between the surface and the orifice. No horizontal, but only vertical air flow was detected in the inner rooms of the cave. Based on the evaluation of temperature, air humidity and draught conditions, the cave can be divided into three microclimatic sections. The first section consists of the immediate entrance, the orifice and the passage, where the climatic elements are the most changeable due to constant ventilation. The second section reaches from the Nagy-terem to the Bástya; the tempe-

ratures are more balanced here already; and the third section lies between the Bástya and the end of the cave, and it also includes the higher regions (near the ceiling) of the second section. The annual fluctuation of the temperature remains within 1 °C here (Szabó, 1963). The climatic conditions are monitored on a continuous basis in order to control and maintain the microclimate of the cave and to control the quantities of pests (Munkácsi, 2005).

Szent István Cave climatic studies in the Fekete-terem showed that the drip rate in the cave always provides sufficient humidity for the therapy. The mean temperature is 9.93 °C, slightly changeable, but the extent of changes does not influence therapy substantially. The variability of the air temperature in the Fekete-terem is different from the fluctuations in other places of the cave, the major causes of which include the presence of therapy groups and the heating effect of the lights. The temperature fluctuations caused by the curative sessions primarily depend on the size, composition and activity of the group. The maximum air temperature is reached in 12 to 15 minutes after the start of the session, then it minimally decreases, and then stabilises. Then it rises again when the group is leaving the room. Regeneration is possible only during the night. The low radon concentration values in winter and higher values in summer indicate high seasonal fluctuation which is caused by the draught conditions in the cave. The force and direction of the draught in the Fekete-terem partly depends on the external climatic conditions. The nature of the changes in humidity shows close relation with the changes in the drip yields, but the extent of changes is not significant (Lénárt, 2003).

4. THE IMPORTANCE OF HEALTH STATUS ASSESSMENT OF RESPIRATORY PATIENTS

The reaction of a patient with chronic respiratory disease to physical exercise is different from that of a healthy person. Changes occur not only in the performance of the respiratory system but also in that of the circulatory system, as well as in the efficiency of energy production and in the strength and performance of the skeletal muscles (Barnai, 2007). Patients with mild COPD reach their breathing limits sooner than healthy people during the exercise test due to ventilation differences and pathological breathing mechanics.

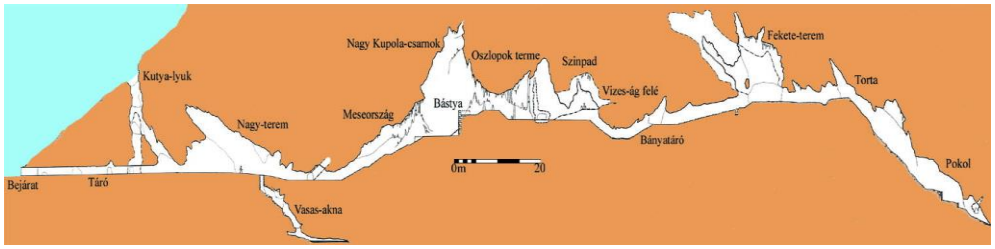

Figure 2
Vertical projection of the Szent István Cave
(Source: http://www.barlang.hu/pages/terkepek.htm)

Medical specialists assess eligibility for cave therapy on the basis of the patient's physical condition and the results of respiratory function tests. The 15–20-minute walk to the therapeutic room in the climate of the cave is significant exercise for the patients, as they need to cover an elevation corresponding to 4 floors, climbing up and down in turn, both on a pavement and stairs, which may be slippery due to dripping water or mud. It is a primary concern that the patient's state must not be put at risk. The patient is guided to the therapeutic cave room by two qualified nurses who are experienced first aid providers, know the paths in the cave well, and can manage lighting properly. No physician is present at the scene in the cave, oxygen therapy is not available for technical reasons, and any emergency care action requires extra time. Thus, it is of key importance to screen out those patients who must not be put to the risks of the tour, notwithstanding the importance of their stay in the air of the cave. Accordingly, it is fairly difficult for the specialist to decide whether speleotherapy should be indicated or contraindicated.

There are several stops on the way up, as shown in *Figure 2*. The first, 55-metre long and almost horizontal artificial passage starting from the entrance intersects several natural rock caves before reaching the first larger room. The first stop is here, in the Nagy-terem, where the patient gets accustomed to the cave air and altered visibility. To access Kupola-csarnok, the largest room of the cave, one must climb a stairway of 72 steps. This room is the second stop after a fairly demanding section of the route. The next section of the cave is the elevation called Bástya after a stairway of 30 steps. Right after the Oszlopok-csarnoka, one arrives at the Színház-terem, and from there, through 17 steps, at the Bányatáró; finally, after 32 more steps on the stairs, one may enter the Fekete-terem, the venue of the therapy.

5. MATERIALS AND METHODS

Our work was performed at the Respiratory Rehabilitation Department, Borsod-Abaúj-Zemplén County Central Hospital and University Hospital. Those patients with diagnosed COPD or bronchial asthma were involved who participated in the complex respiratory rehabilitation programme. We collected data in two periods. In the period between November 2014 and March 2015, we studied those patients whose rehabilitation included cave therapy. They constituted the Cave Group. The Contraindication Group included patients whose programme did not include the cave therapy, based on the specialist's recommendation. The latter studies took place from October 2015 to January 2016. In the case of the Cave Group, we allowed voluntary participation in the study, while the other group involved every patient who was treated at the Department in the given period and met the above criteria. In each case, we explained to the participants the purpose and method of the study and obtained their written consent. We started work after obtaining the relevant authorisation from the Regional and Institutional Committee of Science and Research Ethics, Borsod-Abaúj-Zemplén County Hospital and University Hospital.

At the beginning of our patient study, the patient's clinical status was recorded. Somatometric data was measured, and deviation from the optimal body mass was

determined using Möhr's formula (Fehérné Mérey, 1996), expressed in per cent (%); the two types of spinal length were calculated, and, based on that, the Delmas Index was calculated according to the rules of physiotherapy (Balogh, 1999).

Categorisation was also performed, and, on the basis of the result, the sagittal plane spinal curvatures were regarded as normal (n), increased (d), or reduced (s). Chest mobility was also determined by measuring the difference between the maximum circumference (at the height of the nipples) after inhalation and exhalation. Patients' endurance was assessed by two tests. The 6-minute walking test was performed in a corridor of 80 m. Before the walking test, the resting pulse was taken after 10 minutes of lying with the eyes closed in a quiet examining room. The maximum pulse value was measured with the patient standing, immediately after completion of the walking test. Voluntary apnoea time was measured in maximum inhalation position, with the patient sitting. One concomitant disease was highlighted: we looked for ischaemic heart disease (IHD) in the patient documentation. Of the respiratory function parameters we used FEV 1% for the purposes of characterisation and categorisation.

Patient's subjective perception of their health was assessed using the SF-36 Questionnaire. The questionnaire includes 36 easy-to-answer questions. The questions can be sorted into 8 groups along the various dimensions of quality of life: physical functioning, role limitations due to physical problems, bodily pain, general perception of health, vitality, social functioning, role limitations due to emotional problems, and general mental health. Scale values between 0 and 100 are assigned to the dimensions, where lower values show lower quality of life. Using these values, the electronic calculator computes Physical Health and Mental Health values, and determines so-called norm values for each dimension. These norm values make it possible to compare our patients' values to the norm values of the general population of Hungary (Czimbalmos et al., 1999; Ware, 1993).

Data was presented in terms of mean values and standard deviation. Student's t-test for two samples was used for the comparison of the groups, and Pearson's chi-squared test was applied in the case of discrete distribution of variables. The results were regarded significant in the case of $p \leq 0.05$. Calculations were performed using the SPSS 20.0 statistical software.

6. Results

Table 1 shows data of the two groups. Our study includes data of 46 patients in total. The Cave Group (CaG) included 30 patients (9 males and 21 females). Their mean age was 60.33 ± 6.62 years. During our study period, the number of patients treated at our department and receiving speleotherapy was much higher than the number of our participants. The reason for this is that voluntary participation was allowed.

Several patients who would have met the criteria preferred not to participate. The mean overweight in the group was +28.61%. COPD had been diagnosed in 43.3% of the group. Almost half (46.66%) of the participants had IHD. As regards the severity categories determined on the basis of the FEV 1%, a significant proportion of

the patients were mild or moderate (mi + mo = 90%). The physiological sagittal spinal curvatures were typically reduced (s = 70%).

Table 1

Group characteristics

Groups	Diagnosis COPD/asthma	Concomitant IHD	Stage mi/mo/se	Vertebral column status n/s/d
Cave n = 30	13/17	14	16/11/3	8/21/1
Control n = 16	9/7	12	4/8/4	5/4/7

IHD = ischaemic heart disease
mi/mo/se = mild/moderate/severe
n/s/d = physiological spinal curvature (sagittal plane) normal/reduced/increased

The Contraindication Group (CiG) included 16 patients (6 male and 10 female). Their mean age was 66.4 ± 7.22 years. This is the number of patients who could not participate in the cave therapy due to recommendation from the specialist. The mean overweight in this group was +35.27%. Diagnosed COPD was present in 56.3% of the group, which is slightly more than half of them. IHD had been diagnosed in ¾ part of the group. The FEV 1% based categorisations showed that a majority of these patients were characterised by medium severe state, but almost as many patients showed mild or severe state. The physiological sagittal spinal curvatures were typically increased (d = 43.75%). The presence of IHD was more characteristic of the Contraindication Group, but the difference was not statistically significant ($p = 0.06$). As regards objective parameters, the FEV 1%, chest mobility, voluntary apnoea time and the resting pulse showed no difference between groups. There were significant differences in the case of two parameters. The distance covered was longer in the Cave Group (CaG 468.98 ± 66.52 vs. CiG 306.56 ± 70 $p < 0.001$) and the maximum exercise heart rate was higher (CaG 103.47 ± 13.93 vs. CiG 84 ± 15.08 $p < 0.001$).

Similar to the objective parameters, most of the subjective ones showed no significant differences between the two groups. Significant differences were only found with two parameters: reduced physical activity was detected in the control group (CaG 35.43 ± 6.91 vs. CiG 22.79 ± 11.62 $p < 0.001$), and general perception of health was lower in the Cave Group (CaG 30.16 ± 6.03 vs. CiG 37.92 ± 5.94 $p < 0.001$).

7. Conclusions

Generally, the majority of the patients referred to rehabilitation are patients in good or medium condition, mainly with COPD or bronchial asthma, who look for speleotherapy. The qualified curative cave of Lillafüred attracts patients needing this type

of care to Miskolc. However, a rather rigorous path to reach the therapy cave puts our patients' endurance to the test to some extent.

On the basis of our studies, we would say that in our case those patients belong to the risk group whose walking distance is within 350 m and 400 m. Our simple test used to assess endurance showed a significant difference between the two groups. That is, the distance covered in 6 minutes may be useful information for the treating physician. We know, however, that the test is not free of subjective elements, and its end result is influenced by a number of other factors as well, for instance chest mobility, which we analysed in our study, and various posture problems. These parameters influence the patient's breathing technique – and through that, endurance as well – significantly. These factors were present in large proportions in our patient groups. Overweight was a further unfavourable factor. Our study highlights the existence of two more risk factors as well. Those patients with chronic respiratory diseases who are elderly or have IHD as a concomitant disease require a very careful and detailed evaluation of state. The severity category determined on the basis of FEV 1% does not represent contraindication in itself. We presented severe cases referred to cave therapy, as well cases where a milder state was still subject to contraindication.

As regards their disease, the patients may be classified into the "Mild" category. On the basis of relevant literature as well as our experience, we came to an important conclusion: building up individual therapies for these patients requires special attention. In both groups, the patients studied perceived their state of health to be unfavourable. In the physical activity dimension, the Cave Group showed better results, just as expected. The background cause behind our results may be that patients often have to cope with shortness of breath, and that is one of the symptoms which indicates an impairment of state in the form of difficulty in breathing and thus has a negative effect on the quality of life. An advantage of the evaluation methods we use is that they are easy to apply with elderly people as well.

Utilisation of natural features as diversely and as continuously as possible is at the heart of the professionals involved in respiratory rehabilitation, too. It will be a challenging task to design and implement respiratory rehabilitation programmes which take into account the physical and psychic state of the elderly age group with low endurance, with overweight, and with concomitant cardiac disease.

ACKNOWLEDGEMENTS

The described article/presentation/study was carried out as part of the EFOP-3.6.1-16-00011 *Younger and Renewing University – Innovative Knowledge City – institutional development of the University of Miskolc aiming at intelligent specialisation* project implemented in the framework of the Szechenyi 2020 programme. The realisation of this project is supported by the European Union, co-financed by the European Social Fund.

REFERENCES

[1] Balogh I. (1999): *Mozgás ABC. Kineziológiai alapismeretek*. Tillinger Péter Kiadó, Budapest, p. 72.

[2] Barnai M. (2007): *Az akaratlagos apnoe idő alkalmazása a mozgásterápia intenzitásának meghatározásában, és hatásainak mérésében*. Doktori értekezés, Pécs, p. 12., pp. 52–53.

[3] Czimbalmos Á., Nagy Zs., Varga Z., Husztik P. (1999): Páciens megelégedettségi vizsgálat. *Népegészségügy*, 1.

[4] Fehérné Mérey I. (1996): *Mozgás és egészség. Hungarofit: Mérd magad!* Útmutató, Budapest, p. 87.

[5] Fodor I. (1975): *Gyógybarlangok klímaviszonyainak komplex vizsgálata számítógépes feldolgozás segítségével*. Beszámoló a Nemzetközi Barlangtani Unió Barlangterápiai Szakbizottságának Magyarországi (II.) Szimpóziumáról. MKBT Budapest, pp. 83–91.

[6] Fodor I. (1981): *A barlangok éghajlati és bioklimatológiai sajátosságai*. Akadémiai kiadó, Budapest, pp. 23–168.

[7] Gádoros M. (1989): A barlangi klíma fizikai rendszere – A barlangi külső és lakásklíma összehasonlítása. In: Tardy J.: *Barlangklimatológia – Barlangterápia*. Budapest, pp. 35–42.

[8] Géczy G. (1989): *Barlangi légmozgások nyomjelzése természetes radonnal*. KLTE, TDK-dolgozat, Debrecen, pp. 3–23.

[9] Horváth T. (1984): A barlangterápia lehetőségei és szerepe az idült légúti megbetegedések komplex rehabilitációjában. *VII. Nemzetközi Szpeleoterápiai Szimpózium*, MKBT, Budapest, pp. 161–166.

[10] Karlowits T., Varga A. (2001): *A lillafüredi Szent István-barlang klímaterápiás jellemzőinek vizsgálata*. ME, TDK-dolgozat, Miskolc, pp. 18–32.

[11] Lénárt L. (2003): *Barlangterápiai célú vizsgálatok a lillafüredi Szent István-barlang Fekete-termében és környékén XIII*. Kézirat, Miskolc, pp. 8–12.

[12] Magyar P. (szerk.). (2006): *Egészségügyi szakdolgozók tüdőgyógyászati kézikönyve*. Medicina, Budapest, pp. 197–214.

[13] Mucsi J., Mucsi L. (1987): A Hajnóczy-barlang mikroklímájának hatása egészséges populáció légzésfunkcióira. *Balneológia, Rehabilitáció, Gyógyfürdőügy*, 2, pp. 93–99.

[14] Munkácsi A. (2005): *A Csanyiki Légzőszervi Rehabilitációs Osztály tevékenysége, különös tekintettel a barlangterápiára.* Tanulmány, Miskolc.

[15] Pocket Guide to COPD Diagnosis, Management, and Prevention (2017): *A Giude for Health Care Professionals 2017 Report*. http:// www.goldcopd.org/Guidelines/- resoures.html.

[16] Roda I., Rajman L. (1975): *A barlangklimatológia terén alkalmazott mérések módszertana és a barlangterápia feltételei*. Beszámoló a Nemzetközi Barlangtani Unió Barlangterápiai Szakbizottságának Magyarországi (II.) Szimpóziumáról. MKBT Budapest, pp. 48–56.

[17] Szabó Gy. (1963): Angaben zum Mikroklima der Höhlen bei Lillafüred. *Acta Climatologica*, Tom. II–III, Fasc. 1–4, Szeged, pp. 18–20.

[18] Ware, J. E. Jr. (1993): *SF-36 Health Survey: Manual and Interpretation Guide*. The Health Institute, New England, Medical Centre, Boston MA.

Geosciences and Engineering, Vol. 7, No. 10 (2019), pp. 105–115.

PORE PRESSURE PREDICTION IN PANNONIAN HYDROCARBON RESERVOIR SYSTEMS USING AN INTEGRATED INTERPRETATION APPROACH

ZSOLT NAGY[1] – MÁTYÁS KRISZTIÁN BARACZA[2] – NORBERT PÉTER SZABÓ[2, 3]

[1]MOL Plc.,
[2]University of Miskolc,
[3]MTA-ME Geoengineering Research Group, 3515, Miskolc-Egyetemváros

Abstract: The basin scale examination of pressure conditions is an important task from many aspects. One is that well planning requires an understanding of the pressure regime, another is that any abnormal pressure conditions could affect the behavior of the petroleum system.

The upper boundary of an abnormal pressure zone was identified based on sonic and resistivity logs. The analysis of the pressure trends with integrated interpretation of the lithology sensitive logs, including natural gamma-ray intensity, spontaneous potential and resistivity, proved that the overpressure generation is related to strata with high shale content. Two sedimentary environments formed during the Pannonian sedimentation cycle where shale rich sediments were deposited: the delta slope and the foreground of the turbidite systems.

As the formation of abnormal pressure regime relates to low permeability sediments, the main overpressure generation mechanism might be undercompaction. This theory is confirmed by the well log signatures of these sections. Beside the non-equilibrium compaction, at least two other mechanisms could contribute to the overpressure: clay mineral transformation and the effect of uplifts.

Basin modeling is an alternative method for pressure regime investigation. To test the technique a 3D basin model was built. This approach allowed us to investigate the effect of the lateral transfer and hydrocarbon generation. Furthermore, information about the timing of the overpressure development was gained.

Keywords: *abnormal pressure, 3D basin modeling, undercompaction, lateral transfer*

1. INTRODUCTION

Several methods have been worked out for pore pressure prediction in the last decades [1]. These methods are basically sorted into two main groups: some of them focus on well locations while others deliver information from an area.

Well logging or one-dimensional methods are continuously losing their importance due to their limitations [2]. Pore pressure prediction methods based on well logs focus on the identification of normal compaction trends. If overpressure is pre-

sent at shallow depths the normal compactional trends could be overestimated and the calculated pore pressure will be underestimated. Moreover, there is a basin scale pressure regime in sedimentary basins, which means that the overpressure developed in the deeper parts of the basin could affect the pressure regime above structural highs. This connection and pressure equalization is called lateral transfer [2].

Another type of prediction method relies on seismic modeling and inversion. Relatively few pressure prediction studies have been created with basin modeling software [1, 3, 15]. Basin models can integrate the results of different methods, e.g., laboratory measurements, formation evaluation using well logs, and seismic based maps. However, one of the biggest advantages of this method is its flexibility, since there is no required minimal dataset for the simulation. Naturally, the quality of the results can be increased with the integration of more data.

2. REGIONAL GEOLOGICAL SETTING

The area of investigation is located in South Hungary near the Serbian border and totally covered by 3D seismic data *(Figure 1)*. More than 85 wells have been used with their wireline logs and core data for the lithological evaluation and model calibration. The wells were drilled from the late 1960s to the 2010s, so the available dataset is strongly heterogeneous.

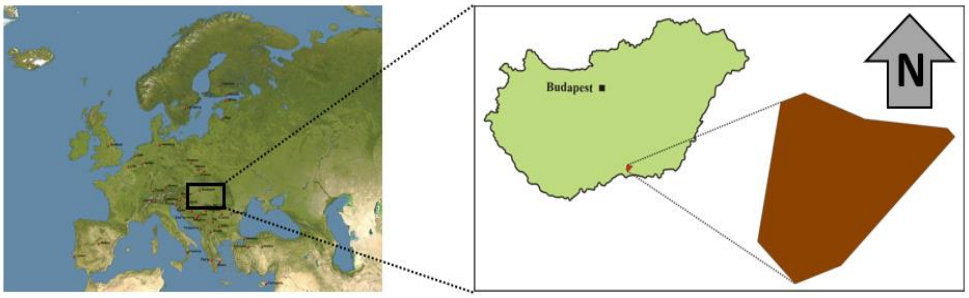

Figure 1
Study area located in South Hungary

According to the exploration and field development wells, the basement of the study area consists of Mesozoic carbonates (mainly dolomite) and Paleozoic metamorphic rocks. The most relevant part of the stratigraphic column from the pore pressure prediction point of view is the Neogene sedimentation. The penetrated Middle Miocene sediment cycle was formed due to transgression, which starts with abrasional conglomerates and breccias. The Middle Miocene subbasins were filled with marine siltstones, marls and carbonates. The distribution of different lithofacies was controlled by the maximal water depths of the subbasins. The thickest sediment package was deposited during the Late Miocene and Pliocene and its maximal thickness can exceed 3,500 m in the study area. The sedimentation cycle was controlled by a prograding delta system, which filled the accommodation space

from NW to SE *(Figure 2)*. The marls and calcareous marls of the Endrőd Formation were deposited in pelagic pro-delta environment. The overlaying turbidite system, called the Szolnok Formation, represents a basin center and a slope-toe environment, which is covered by shale and siltstone, called the Algyő Formation. Delta front sandstones (Újfalu Formation) were deposited to the slope sediments. Finally, the silt- and sandstones with interfingered lignite layers (Zagyva Formation) close the sedimentation cycle that represents the sediments of an alluvial depositional environment [6, 7, 14].

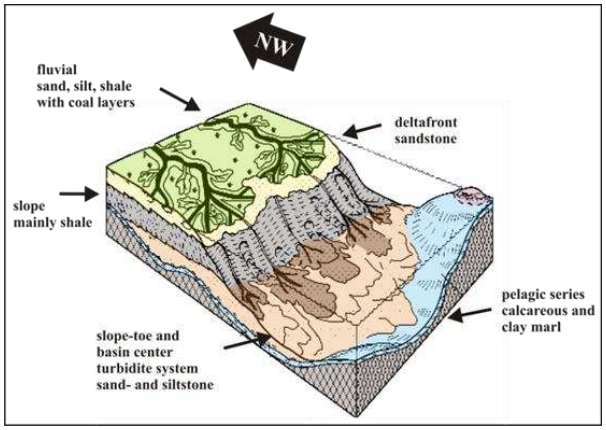

Figure 2
Prograding delta system and depositional environments in the Late Miocene, Pliocene
(modified after Juhász, 1992)

3. MATERIAL AND METHODS

The workflow applied here was built up from two stages: well log based evaluation and basin model building *(Figure 3)*. Petrophysical data were used for gaining background information for basin modeling that could deliver the top of overpressure zone. These tops were used as calibration parameters for modeling and delineating the strata which could have taken an active part in overpressure formation [4]. And on the top of that, well log based porosity data delivered the values for creating porosity-depth trends.

The model building phase started with the creation of a basic background geomechanical model, based on porosity-depth and porosity-permeability relationships. The interpreted and depth converted seismic sections have been applied to build up the subsurface region during the main modeling phase [5]. Distribution of Pannonian and pre-Pannonian

Middle Miocene lithostratigraphic units were mapped based on well logs and well completion reports [6]. The geological timeframe of sedimentation was estimated with the correlation of magnetostratigraphic horizons [7].

Drill stem test and mud density equivalent pressure data were used to calibrate the pressure models. Porosity and permeability data derived from well logs and from measurements delivered the proper calibration points in case of porosity and permeability.

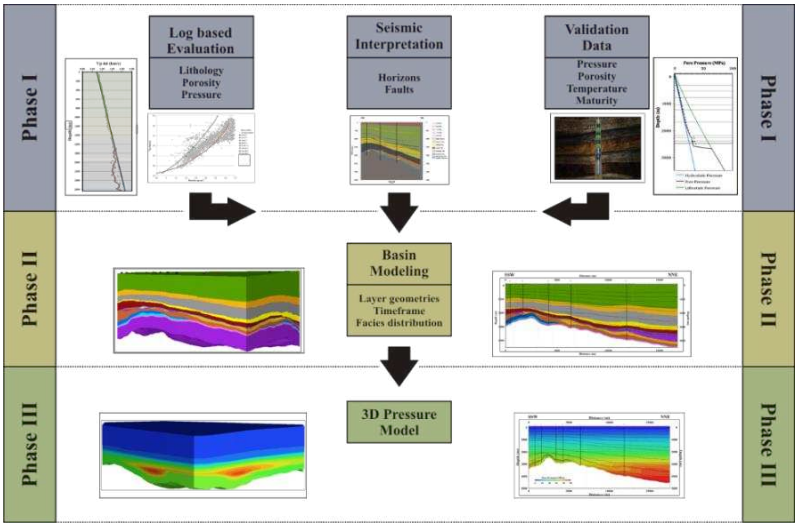

Figure 3
Schematic flowchart of the modeling workflow

3.1. Wireline Log based evaluation

Two different well-log analysis methods were used to identify the top of overpressure zone, based on the resistivity and acoustic travel time logs. In both cases only the shale-rich layers were considered since higher permeability zones could be affected by lateral transfer [2]. The first step was identifying the shale baselines, which reflected the compactional behavior of shales when abnormal pressure could not develop [4], [8], [9].

If overpressure can be formed in a shale-rich layer, the measured well logging data will fall behind the normal compactional trend, so the top of the overpressure zone could be marked [2]. Moreover, the higher the deviation between the measured and the determined normal compaction trends, the higher the overpressure, so the increment in overpressure in those layers could be assumed.

When the overpressure build-up is identified, the next step is to understand the processes which formed the abnormal pressure regime. P-wave acoustic travel time log and a cross plot technique are the most appropriate methods to do this. The behavior of acoustic-depth profile is different in the case of non-equilibrium compaction and in aquathermal fluid expansion [10]. The density-sonic cross-plot is an appropriate tool to prove the presence of chemical compaction (diagenetic smectite-to-illite transition) driven overpressure [11–12].

3.2. Basin Modeling

Interpreted and depth converted seismic sections were used to create horizons for basin modeling. The ages of these horizons were known from the magnetostratigraphic analysis of core data [7]. Layers were generated from these horizons, and thus different sedimentation rates could be assigned to the model *(Figure 4)*. The tops of Pannonian (s.l.) lithostratigraphic units were picked in exploration wells based on the natural gamma-ray and resistivity logs and based on these the interpolated facies maps were generated [6] to describe the horizontal and vertical facies variation within a layer. The facies distribution and mechanical properties of rocks were not uniform within the layers.

The compaction rates for different facies were simulated through geological time, and the calibration of the basin model was achieved in two steps. In the first step the simulated porosity and pore pressure were fitted to measured data points, and in the second step the simulated temperature and maturity values were fitted [5].

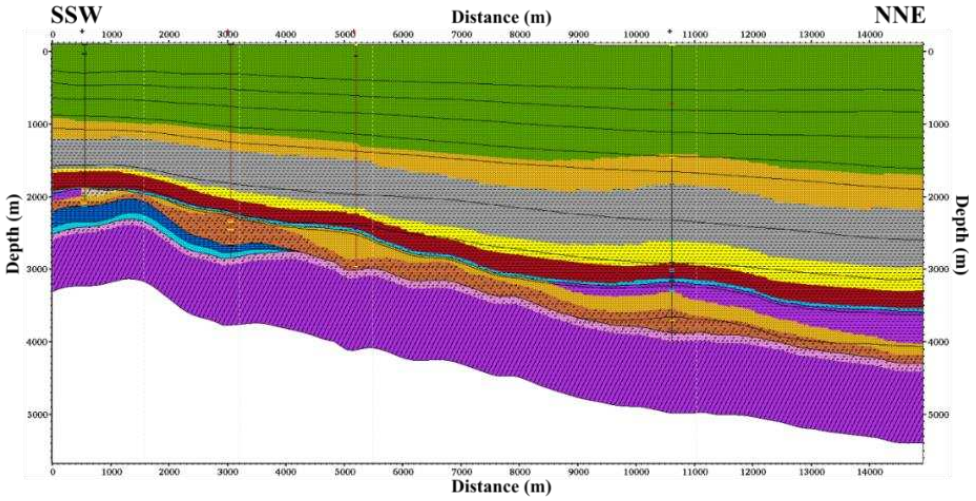

Figure 4

NNE-SSW directional depth section along the modeled area. Continuous lines are the mapped and depth converted chronostratigraphic horizons and the different colors represent the unique lithostratigraphic units

4. RESULTS

Acoustic and resistivity-depth profiles measured along wells suggested that at least three different pressure regimes are present in the study area *(Figure 5)*. Overpressure could be formed in the upper or middle part of the Algyő Formation (shale-rich slope sediments) in the deepest part of evaluated area. However, abnormal pressure is identified only in the pre-Pannonian Middle Miocene strata above the

structural highs. There is a transition zone between the two different areas, where the overpressure begins to from in the lower part of the Algyő Formation and could rise in the Endrőd (clay and calcareous marl) Formation.

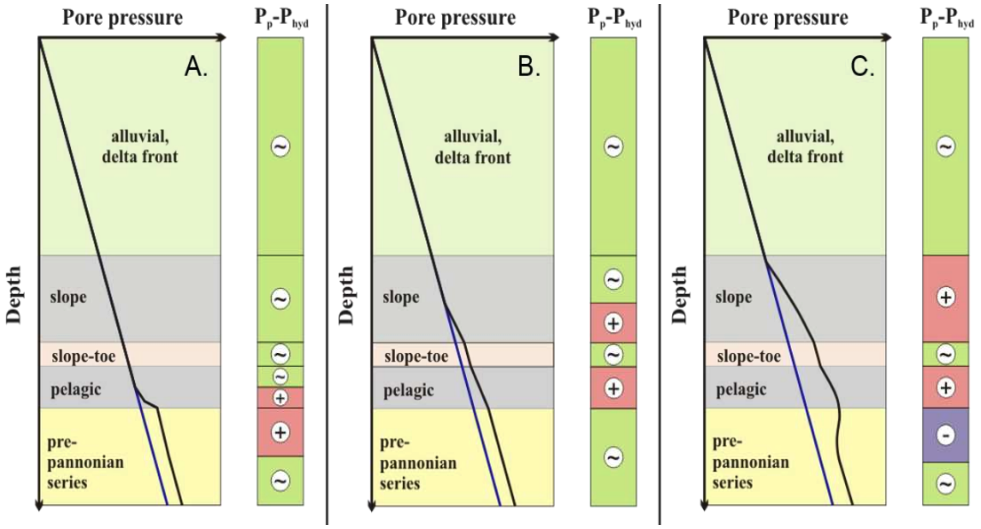

Figure 5

Identified pore pressure-depth trends within Pannonian (s.l.) depositional environments (A = areas above structural highs; B = transition zones; C = deepest basin parts)

Well log signatures suggest that the main overpressure generation mechanism could be non-equilibrium compaction in the deepest parts of the basin and in transition zones. However, above the pre-Neogene anticlines a part of the excess hydraulic pressure could be transferred from deeper areas to the pre-Pannonian Middle Miocene strata. Moreover, in several wells a sharp density increase could be observed on density-velocity cross-plots. These shifts relate to a temperature interval around 100–110 °C, which could be generated by clay mineral transformation [13] *(Figure 6)*. The main chemical compaction equations were tested during the modeling, but their application resulted in extremely high pore pressure values. Moreover, the core descriptions mentioned calcite cement in case of shales. The main cement should have been quartz if high rate smectite-to-illite diagenetic transformation took place.

Modeling results suggest that overpressure started to form in deeper parts of the basin approximately 5 Ma ago, and it continuously increased during the burial *(Figures 7–9)*. Modeling also suggested the importance of the sedimentation rate in overpressure formation. The scenario when the sedimentation rate was 10 times lower suggested that overpressure could not form because the pore fluid could escape from the pore space during the slower burial.

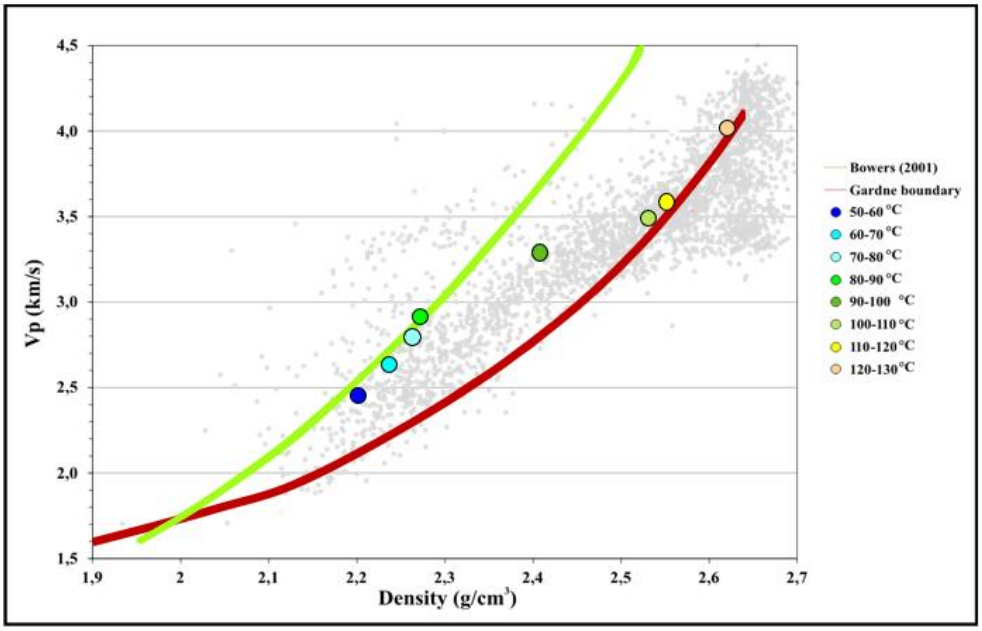

Figure 6

Density-Compressional wave velocity cross-plot, where data points are colored based on temperature zones. Density increase was identified at the 100–110 °C interval that could be interpreted as the effect of smectite-to-illite transformation

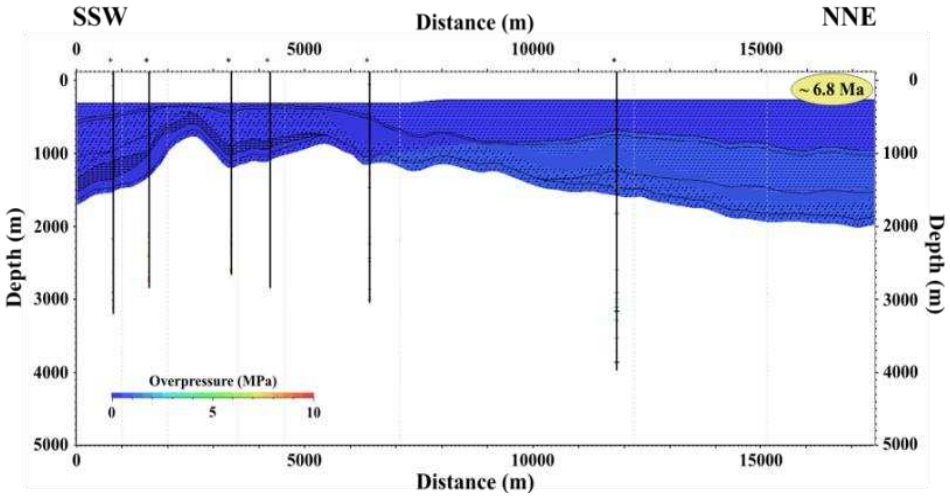

Figure 7

Simulated overpressure values along a SSW-NNE section 6.8 Ma ago. Overpressure has not developed yet

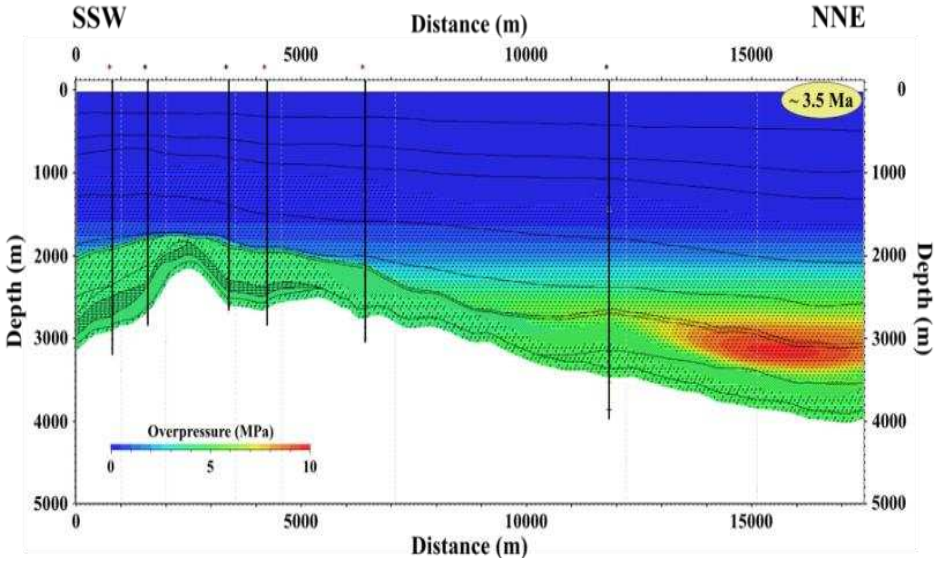

Figure 8

Simulated overpressure values along a SSW-NNE section 3.5 Ma ago. Overpressure started to develop in the deeper part of the basin, and with lateral transfer it could be released in the more permeable facies of the pre-Pannonian Middle Miocene layer

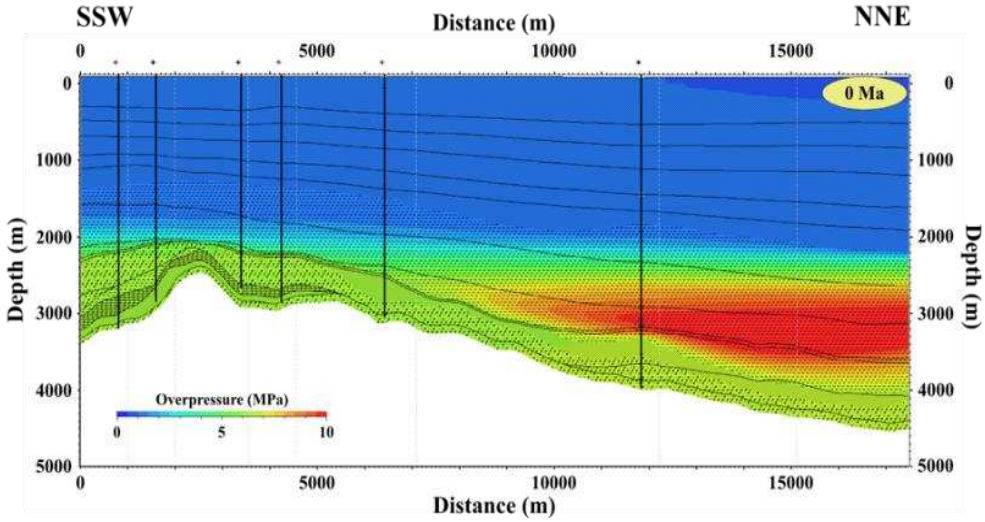

Figure 9

Simulated overpressure values along a SSW-NNE section 0 Ma ago (present day). The amount of overpressure has increased since 3.5 Ma due to continuous burial and restricted compaction

5. DISCUSSION

Comparisons between measured and calculated pressure data were carried out at the end of the model building and calibration phase. A wide range of measured pore pressure data was available, which covers the range from 12 to 45 MPa, but the 30–40 MPa values are overrepresented because these data belongs to the main reservoirs. Generally, the calculated deviation between simulated and measured data is less than ±2 MPa *(Figure 10)*.

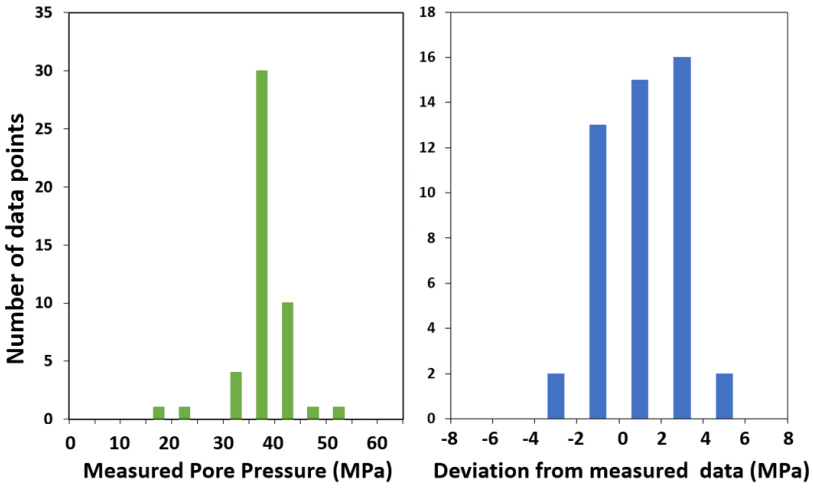

Figure 10

Statistical distribution of measured pore pressure data used as calibration point (left). Histogram of the absolute deviation values in MPa (right)

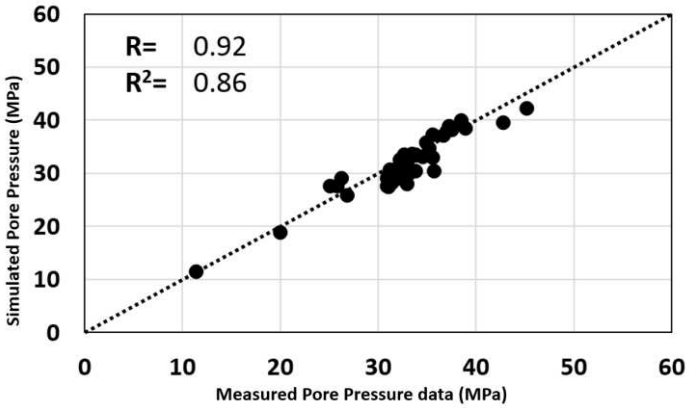

Figure 11

Linear regression relationship between the measured and calculated pressure in MPa

Linear regression modeling was performed to calculate the Pearson's correlation and determination coefficients between the measured and calculated data points, respectively *(Figure 11)*. According to both quality check parameters, the calculated values of pressure have a strong correlation with measured values ($R = 0.92$, $R^2 = 0.86$). Slight underestimation was identified in the 25–30 MPa interval, which could be explained by the short closing time during the well tests, that could have led to the overestimation of static pore pressure during the well test evaluation.

6. CONCLUSIONS

The applied workflow presented in the paper reveals a 3D development history of pore pressure. The suggested basin modeling approach did not reject the application of previously accepted various methods; rather, it integrated the results of different approaches into one model.

Wireline log-based evaluation provided the top of the overpressure zone in wells and identified the lithostratigraphic units that played an active role in pore pressure development. Based on the well-logging data, at least three different overpressure generation zones were identified that are hydrodynamically connected to each other. Simulation of basin development delivered the history of subsurface pressure regime on the geological time-scale.

According to the gained experience, the quality of simulation strongly depends on the mechanical characteristics of identified lithologies and on the mechanical models associated with them. Further work will focus on developing basin-scale porosity vs. effective stress and porosity vs. permeability relationships that will potentially improve pore-pressure prediction.

ACKNOWLEDGEMENTS

The research was carried out in the framework of the GINOP-2.3.2-15-2016- 00010 *Development of enhanced engineering methods with the aim at utilization of subterranean energy resources* project of the Research Institute of Applied Earth Sciences of the University of Miskolc part of the Széchenyi 2020 Plan, funded by the European Union and co-financed by the European Structural and Investment Funds. The first author expresses his sincerest gratitude to the Sámuel Mikoviny Doctoral School of Geoscience of the University of Miskolc and to MOL Group for their technical support.

REFERENCES

[1] Huffman, A. R. (2002): The future of pressure prediction using geophysical methods. *AAPG Memoir*, 76, pp. 217–233.

[2] Swarbrick, R. E. (2002): Challenges of porosity-based pressure prediction. *CSEG Records*, Vol. 27, No. 7, pp. 95–103.

[3] Shatti, I. A., Ghosh, D., Yusoff, W. I. W. (2005): 3D predrill pore pressure prediction using basin modeling approach in a field of Malay Basin. *Asian Journal of Earth Sciences*, 8 (1), pp. 24–31.

[4] Zhang, J. (2011): Pore pressure prediction from well logs: methods, modifications and new approaches. *Earth-Science Reviews*, Vol. 108, pp. 50–63.

[5] Hantschel, T., Kaueraf, A. I.: *Fundamentals of Basin and Petroleum Systems Modeling*. Springer-Verlag, Heidelberg, 2009.

[6] Juhász G. (1992): A pannóniai (s.l.) formációk térképezése az alföldön: elterjedés, fácies és üledékes környezet. *Földtani Közlöny*, 122/2–4., pp. 133–165.

[7] Pogácsás G., Szabó A., Szalay J. (1992): Az alföldi progradációs delta sorozatok kronosztratigráfiai viszonyai. *Magyar Geofizika*, 33/1., pp. 1–13.

[8] Bowers, G. L. (1995): Pore pressure estimation from velocity data: accounting for overpressure mechanisms besides undercompaction. *SPE Drilling and Completions*, June, pp. 89–95.

[9] Eaton, B. A. (1975): The equation for geopressure prediction from well logs. *Proceedings, SPE Society of Petroleum Engineers of AIME,* paper No. 5544.

[10] Sarker, R., Batzle, M. (2008): Effective stress coefficient in shales and its applicability to Eaton's equation. *The Leading Edge*, Vol. 27, No. 6, pp. 798–804.

[11] Hoesni, M. J.: *Origins of overpressure in the Malay Basin and its influence on petroleum systems*. PhD thesis, Durham University. Available at: http:// ethe ses.dur.ac.uk/1755/.

[12] Lahann, R. (2002): Impact of smectite diagenesis on compaction modeling and compaction equilibrium. *AAPG Memoir*, Vol. 76, pp. 61–72.

[13] O'connor, S., Swarbrick, R., Hoesni, J., Lahann, R. (2001): Deep pore pressure prediction in challenging areas, Malay basin, SE Asia. *Indonesia petroleum association 35th annual convention & exhibition*. 18–20 May, 2011, Jakarta, Indonesia.

[14] Sztanó, O., Szafián, P., Magyar, I., Horányi, A., Bada, G., Hughes, D. W., Hoyer, D. L., Wallies, R. J. (2013): Aggradation and progradation controlled clinothems and deep-water sand delivery model in the Neogene Lake Pannon, Makó Trough, Pannonian Basin, SE Hungary. *Global and Planetary Change*, 103, pp. 149–167.

[15] Petmecky, R. S., Albertin, M. L., Burke N. (2009): Improving sub-salt imaging using 3D basin model derived velocities. *Marine and Petroleum Geology*, 26, 4, pp. 457–463.

Geosciences and Engineering, Vol. 7, No. 10 (2019), pp. 116–135.

COMBINED ANALYSIS SYSTEM FOR PROPPANT SELECTION IN ASPECT OF FRACTURE CONDUCTIVITY

TAMÁS LENGYEL – ANITA JOBBIK

Research Institute of Applied Earth Sciences

Abstract: The purpose of hydraulic fracturing is well stimulation by which the well performance can be significantly improved. To achieve this, a highly conductive fracture is created which is propped with a propping agent. The success of the treatment is highly influenced by the fracture conductivity, which is the product of the apparent proppant pack permeability and the fracture width. The well productivity after hydraulic fracturing is affected by the interaction between proppants and fracture surface under closure pressures, the proppants embed into the formations and deform due to the closure stress, which can result in a significant reduction in fracture conductivity. Proppant size, Young's modulus and Poisson's ratio of the proppant as well as the formation and, closure pressure are factors which influence proppant embedment and the change of fracture aperture which can actually reduce the fracture conductivity by 20–300% with a subsequent reduction in oil, gas or even in water production (in geothermal wells). This effect is more significant in weakly consolidated formations. Therefore, it is of importance to investigate and understand the theoretical background of proppant embedment.

Keywords: *hydraulic fracturing, proppant, deformation, embedment*

1. INTRODUCTION

To examine the proppant embedment and its influence on fracture conductivity, a static force balance condition is considered to be the best way to investigate this phenomenon. The main benefit of an analytical analysis compared to empirical experiments is that it can be fitted to of all the cases occurring in practice. Empirical models may simulate the reality more accurately but these formulas can be used only in the narrow range in which the equations were derived. These equations may contain fitting coefficients which can be determined only in experimental way, ergo it means parametric equations. An experimental approach means mainly measurements which can be made on core samples for example, and it often requires an accurate measurement system with special apparatus. An analysis system based on an analytical model can be widely used; not to mention that when experimental data is available, the equations which were derived on the basis of analytical consideration can be also fitted with results gained by experiments.

1.1. Purpose of Research

Companies and experts in the field, especially project managers, are interested in the return of the projects. The pay-off of the hydraulic fracturing treatment is significantly affected by the productivity index (PI) of the well. In this paper, several models and considerations were integrated to develop a new analysis system by which different sensitivity tests and a kind of technical optimization of proppant selection can be executed. Ignoring any cost or revenue calculations (CAPEX, OPEX, NPV, etc.), the outcome of this paper provides a method for proppant selection considering not only the factors that influence fracture conductivity but also another optimization method, the so-called Unified Fracture Design (UFD) model.
In a practical point of view, the analysis system provides the opportunity to select the proper type of proppant (proppant size, elastic modulus, specific volume) and to determine the amount of proppant (according to areal proppant concentration) which is needed to achieve the predetermined productivity index of the well (which could be based on net cash flow calculations and reservoir engineering considerations). In addition, is possible to compare the fracture conductivity properties of the proppant pack provided by the manufacturers to the results (computed conductivity values) obtained by performing the calculations studied in this paper. This allows us to evaluate the manufacturer's data in an alternative way.

2. THEORETICAL BACKGROUND

The analytical model, which was derived by Li et al. (2015), approaches proppant embedment from a theoretical aspect. In the followings, one can obtain the theoretical background of the analytical model since the whole detailed derivation process is described below. It is important to note that the model has some limitations. During the stress/strain analysis it was assumed that the proppant would deform and embed into the formation under closure stress, without considering the case of proppant crush. This means that linear elastic behavior was assumed in deriving the analytical model, which entails that one can use the equations only below the stress range which would cause proppant crush.

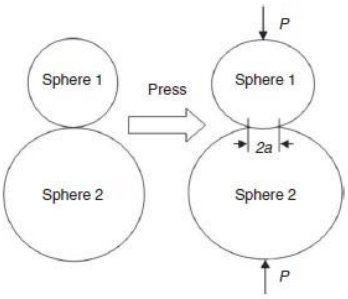

Figure 1
Two mutually squeezed elastic spheres
(Li et al. 2015)

The derivation begins with a stress/strain formula of two mutually squeezing elastic spheres developed by Wu et al. (2001) and which is illustrated in *Figure 1*. Spheres 1 and 2 deform under a balanced load. The boundary of the contact area of the spheres is a circle, and its radius (α) can be expressed as follows:

$$\alpha = \left(\frac{3}{4} P C_E \frac{R_1 R_2}{R_1 + R_2}\right)^{\frac{1}{3}} \tag{1}$$

where α is the radius of the boundary of contact area, in mm; P is the external force on Spheres 1 and 2, in N; R_1 is the radius of Sphere 1, in mm; and R_2 is the radius of Sphere 2, in mm. C_E (in MPa^{-1}) is defined as:

$$C_E = \frac{1-\nu_1{}^2}{E_1} + \frac{1-\nu_2{}^2}{E_2} \tag{2}$$

where ν_1 is the Poisson's ratio of Sphere 1, dimensionless; ν_2 is the Poisson's ratio of Sphere 2, dimensionless; E_1 is the elastic modulus of Sphere 1, in MPa; E_2 is the Poisson's ratio of Sphere 2, in MPa.

Wu et al. (2001) proved that the change in distance between the centers of Spheres 1 and 2 can be described by the following relationship:

$$\alpha' = \frac{\frac{3}{4} P C_E}{\left(\frac{3}{4} P C_E \frac{R_1 R_2}{R_1 + R_2}\right)^{\frac{1}{3}}} \tag{3}$$

where α' is the change in distance between the centers of Spheres, in mm.

When $R_2 \to \infty$, the surface of Sphere 2 tends to become a plane, and the two objects become a mutually squeezed sphere and plane. *Figure 2* demonstrates the interaction between the sphere and the plane. One can observe that α' is affected by two factors: change in radius of Sphere 1 (which is called *deformation*) and embedment. For the situation in *Figure 2*, a modified formula can be derived on the basis of *Equation (3)*:

$$\alpha' = \frac{2\left(\frac{3}{8} P C_E D_1\right)^{\frac{2}{3}}}{D_1} \tag{4}$$

where D_1 is the diameter of Sphere 1, in mm

At this step, *Equation 4* contains the two factors, the change in radius of Sphere 1 (deformation) and the embedment. To derive the deformation of Sphere 1 (β) from *Equation (4)*, the other influencing factor (which is the embedment) must be separated. Therefore, assume that the elastic modulus of the plate (E_2) is infinite, so Sphere 1 does not

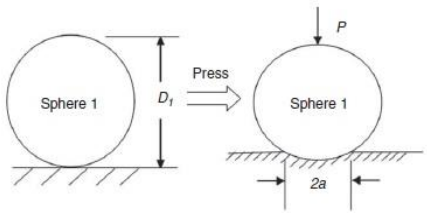

Figure 2
Mutually squeezed plate and sphere
(Li et al. 2015)

embed into the plate. In this case α' is affected only by deformation. Thus, the formula of deformation of Sphere 1 (β) can be expressed as a following relationship:

$$\beta = \frac{2(\frac{3}{8}PD_1\frac{1-\nu_1^2}{E_1})^{\frac{2}{3}}}{D_1} \tag{5}$$

From *Equation (5)*, it can be stated that deformation is influenced only by the values of external force, the diameter, elastic modulus, and Poisson's ratio of Sphere 1, but is not affected by any parameters of the plate.

Since α' was interpreted as the sum of the embedment and the deformation, combining *Equations (4)* and *(5)*, the formula of the embedment of Sphere 1 can be expressed as:

$$h = \alpha' - \beta = \frac{2(\frac{3}{8}PD_1)^{\frac{2}{3}}}{D_1}\left[(\frac{1-\nu_1{}^2}{E_1} + \frac{1-\nu_2{}^2}{E_2},)^{\frac{2}{3}} - (\frac{1-\nu_1{}^2}{E_1})^{\frac{2}{3}}\right], \tag{6}$$

where ***h*** is the value of embedment, in mm.

2.1. Real Situation

To approximate the real situation of the fracture, the situation of spheres being squeezed by two horizontal plates must be described. The analytical model (Li et al. 2015) assumes that the weight of spheres can be ignored, and the stress on spheres and contact areas of the upper and lower plate are the same. To create a more realistic model, Sphere 1 is equivalent to the proppant and the formation is equivalent to the upper and lower plates. It is also assumed that the proppants are evenly paved on the formation (monolayer pattern). Li et al. (2015) introduced a so-called distance coefficient K which helps to represent the distance between the centers of two adjacent proppants as: KD_1. K is equal to unity when proppants are touched by each other, and greater than unity if not. *Figure 3* represents the placement of proppants (single layer) in the fracture. In this paper, the distance coefficient K is disregarded because of simplification and since it does not represent the partial monolayer properties in connection with fracture conductivity.

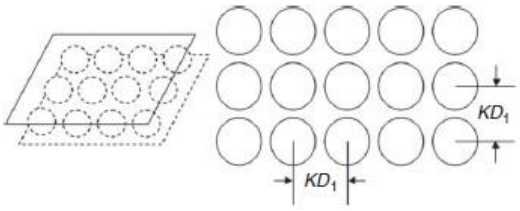

Figure 3
Proppant placement between plates
(Li et al. 2015)

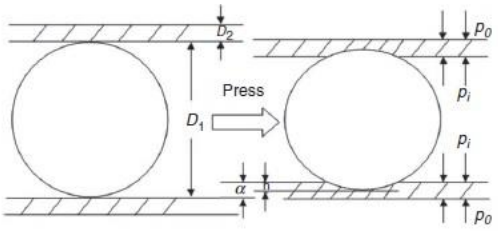

Figure 4
Stress analysis for a single proppant
(Li et al. 2015)

Figure 4 shows the stress analysis for a single proppant. Comparing *Figures 4* and *2*, one can see that the unit of stress is MPa in *Figure 4*, but the unit of load is N in *Figure 2*. The forces between the plates and proppants are acting on the contact areas and the following relationship between the load and stress can be derived:

$$P = p(KD_1)^2 \quad (7)$$

where P is the load acting on the contact areas, in N; p is closure pressure, in MPa, K is distance coefficient, dimensionless; and D_1 is the diameter of proppant, in mm. Furthermore, a relationship can be derived for closure pressure which is the difference of overburden pressure and fracturing fluid pressure:

$$p = p_0 - p_i \quad (8)$$

where p_0 is overburden pressure, in MPa; and p_i is fluid pressure of fracturing fluid, in MPa. It should be noted when $p_0 < p_i$, which happens during the fracturing process (the pressure of fracturing fluid overcomes the in-situ stress of the given rock, fracture aperture is initiated and the fracture starts to propagate), the proppants neither deform nor embed into the formation. When $p_0 > p_i$, which always happens at the end of the fracturing treatment (pumps are switched off and due to this, there is no more extra pressure energy which would exceed the formation's breakdown pressure, so the fracking fluid leaks off and the pressure drops), the proppants deform and embed. Equations obtained in the following can be used only when $p_0 > p_i$, otherwise the equations have no sense.

The thicknesses of the formation in upper and lower case are the same and denoted as D_2. The formation deforms under closure pressure and the deformation can be calculated according to Hooke's law:

$$\Delta D_2 = D_2 \frac{p}{E_2} \quad (9)$$

where D_2 is the thickness of the formation, in mm; and ΔD_2 is the deformation of the formation, in mm. The deformation of the formation is reflected in the form of proppant embedment, because the thickness of the formation that does not contact

with proppants is returned to the initial value. Substituting *Equations (7)* and *(9)* into *Equation (4)*, one can obtain the following equation:

$$\alpha = 1.04D_1(K^2pC_E)^{\frac{2}{3}} + D_2\frac{p}{E_2} \tag{10}$$

where $\boldsymbol{\alpha}$ is the change in fracture aperture, in mm. Li et al. (2015) noted that actually the value of $\boldsymbol{\alpha}$ is half of the change in fracture aperture, but for convenience it is referred to as change in fracture aperture. Later, in fracture conductivity calculations, α is considered to be half of the change in fracture aperture of course.

Continuing the substitution *[Equation (7)* into *Equation (5)* and *Equations (7)* and *(9)* into *Equation (6)]*, one can obtain the following equations:

$$\beta = 1.04D_1(K^2p\frac{1-\nu_1^2}{E_1})^{\frac{2}{3}} \tag{11}$$

$$h = 1.04D_1(K^2p)^{\frac{2}{3}}\left[(\frac{1-\nu_1^2}{E_1} + \frac{1-\nu_2^2}{E_2})^{\frac{2}{3}} - (\frac{1-\nu_1^2}{E_1})^{\frac{2}{3}}\right] + D_2\frac{p}{E_2} \tag{12}$$

where $\boldsymbol{\beta}$ is the proppant deformation, in mm; $\boldsymbol{h}$ is the proppant embedment, in mm; $\boldsymbol{E_1}$ is the elastic modulus of proppant, in MPa; and $\boldsymbol{E_2}$ is the elastic modulus of the formation, in MPa.

3. MULTILAYER PATTERN

3.1. Interaction of Proppants

In the previous sections, a single-layer pattern was assumed to calculate proppant embedment, deformation and the change in fracture aperture. In practice, instead of a monolayer pattern, a multilayer pattern is created more often (Economides and Martin, 2007). During general fracturing treatments the proppants squeeze mutually in addition to the interaction between proppant and formation, therefore it is necessary to analyze the deformation and embedment between proppants as well.

By derivation of equations which can be used to calculate proppant embedment and deformation, Li et al. (2015) assumed that the radius of Sphere 1 and 2 is equal to eachother which is a good approximation because proppants produced by manufacturers have almost the same diameter. As was mentioned before, the radii of Sphere 1 and 2 are the same, so $R_1 = R_2 = R$. In this case, *Equation (3)* can be reduced to:

$$\alpha' = \frac{2(\frac{3}{8}PC_ER)^{\frac{2}{3}}}{R}, \tag{13}$$

where $\boldsymbol{\alpha'}$ is the change in distance between the centers of Sphere 1 and 2, in mm; and $\boldsymbol{R}$ is the radius of Sphere 1 and 2, in mm. The deformation of Sphere 1 and 2 is expressed as:

$$\beta_1 = \frac{(\frac{3}{8}PR)^{\frac{2}{3}}(2\frac{1-\nu_1^2}{E_1})^{\frac{2}{3}}}{R} \quad (14)$$

$$\beta_2 = \frac{(\frac{3}{8}PR)^{\frac{2}{3}}(2\frac{1-\nu_2^2}{E_2})^{\frac{2}{3}}}{R} \quad (15)$$

,

where β_1 and β_2 are the deformations of Sphere 1 and 2, in mm. As deriving the embedment in case of a sphere and plate (deformation was separated from the change in fracture aperture), the embedment of the spheres is calculated by combining *Equations (13)*, *(14)*, and *(15)*.

$$h = \alpha' - \beta_1 - \beta_2 = \frac{(\frac{3}{8}PR)^{\frac{2}{3}}}{R}\left[2(\frac{1-\nu_1^2}{E_1} + \frac{1-\nu_2^2}{E_2},)^{\frac{2}{3}} - \left(2\frac{1-\nu_1^2}{E_1}\right)^{\frac{2}{3}} - (2\frac{1-\nu_2^2}{E_2})^{\frac{2}{3}}\right] \quad (16)$$

where h is the embedment between Sphere 1 and 2, in mm.

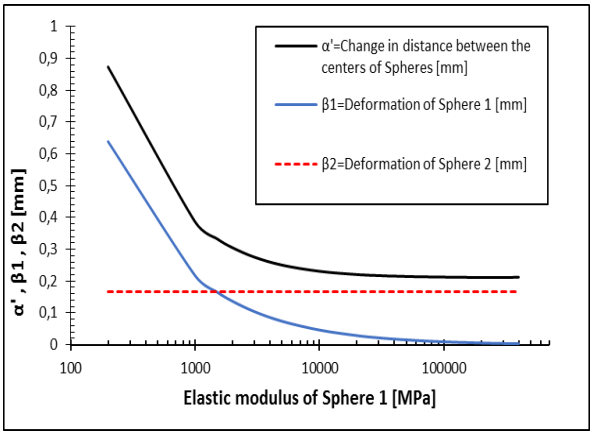

Figure 5
Relationship between the three variables and elastic modulus of Sphere 1

Figures 5 and *6* represent the results gained by using *Equations (13)*, *(14)*, *(15)*, and *(16)*. The known conditions were taken to be $\nu_1 = \nu_2 = 0.2$, $E_2 =$ 1,500 MPa, $R_1 = R_2 = R =$ 0.5 mm, $P =$ 60 N. *Figure 5* shows how the change between the centers of the spheres decreases as the elastic moduli of Sphere 1 increases, and how the deformation of Sphere 1 and 2 changes as a function of E_1. One can observe that the change in distance between the centers of spheres and deformation of Sphere 1 decreases with increasing elastic modulus of Sphere 1. However, defor-

mation of Sphere 2 is constant because it is not dependent on the elastic modulus of Sphere 1.

Figure 6 demonstrates that the embedment (Sphere 2 embedding into Sphere 1) decreases as the elastic modulus of Sphere 1 increases until the elastic modulus of Sphere 2 is greater than elastic modulus of Sphere 1. When $E_1 = E_2$ the embedment is equal to zero and the contact area of the mutually squeezed spheres is a plane. When E_1 becomes greater than E_2 the embedment (Sphere 1 embedding into Sphere 2) increases but not to as high value as before (since one of the elastic modulus is greater than earlier). *Figures 5* and *6* definitely demonstrates that the main cause of the change in distance between the centers of the spheres is the deformation and not the embedment.

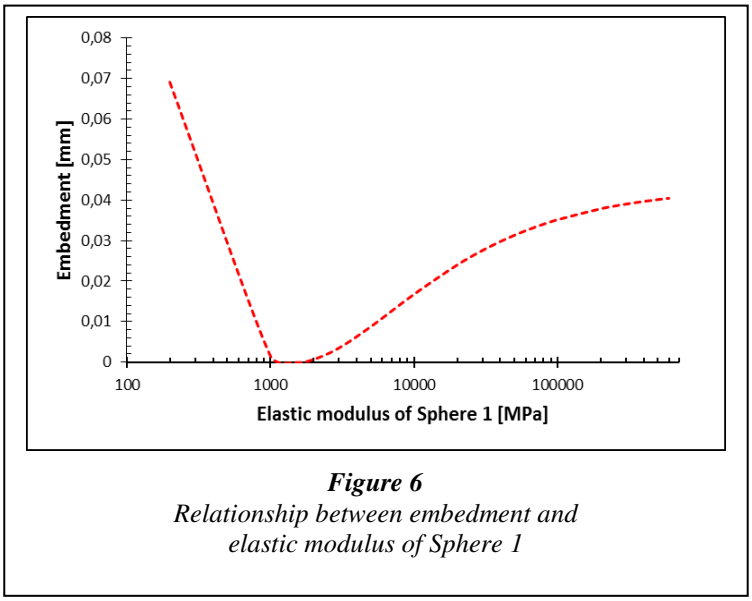

Figure 6
Relationship between embedment and elastic modulus of Sphere 1

3.2. Embedment of Multilayer Pattern

Up to now, we examined the interaction between proppant and formation which was the single-layer situation, and the interaction between proppants as well. As was already emphasized, the proppants are mostly paved in multiple layers in practice; therefore it is necessary to analyze the proppant embedment in the case of multilayer pattern.

As was shown in *Figure 6*, there is no proppant embedment between proppants when the elastic modulus and the size of proppants are the same. Therefore, only proppant deformation and embedment into the formation must be considered. In the case of multilayer pattern, the deformation can be approximated as the value of superposition of each layer's proppant deformation. At the same time, the proppant

embedment (into the formation and not into each other) is the same as in the case of a single-layer pattern because only the top and bottom layers are in direct contact with the formation. Based on the previous assumptions and the single layer pattern model, the corresponding equations can be expressed as follows:

$$\alpha = 1.04D(K^2p)^{\frac{2}{3}}\left\{\left(\frac{1-\nu_1^2}{E_1}\right)^{\frac{2}{3}} + \frac{D_1}{D}\left[\left(\frac{1-\nu_1^2}{E_1} + \frac{1-\nu_2^2}{E_2}\right)^{\frac{2}{3}} - \left(\frac{1-\nu_1^2}{E_1}\right)^{\frac{2}{3}}\right]\right\} + D_2\frac{p}{E_2} \quad (17)$$

$$\beta = 1.04\mathrm{D}\left(K^2p\frac{1-\nu_1^2}{E_1}\right)^{\frac{2}{3}} \quad (18)$$

$$h = 1.04D_1(K^2p)^{\frac{2}{3}}\left[\left(\frac{1-\nu_1^2}{E_1} + \frac{1-\nu_2^2}{E_2}\right)^{\frac{2}{3}} - \left(\frac{1-\nu_1^2}{E_1}\right)^{\frac{2}{3}}\right] + D_2\frac{p}{E_2} \quad (19)$$

where ***D*** is the initial fracture aperture (as shown in *Figure 7*), in mm; ***α*** is the change in fracture aperture of multilayer pattern, in mm; ***β*** is the proppant deformation of multilayer pattern, in mm; and ***h*** is the proppant embedment of multilayer pattern, in mm.

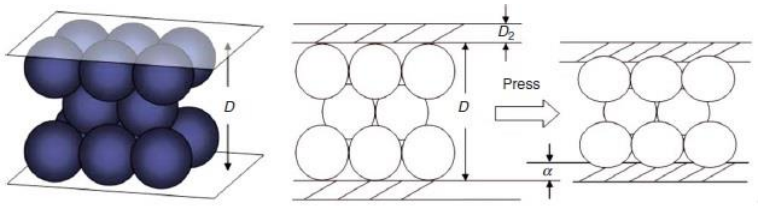

Figure 7
Proppant paving in multiple layers
(Li et al. 2015)

Li et al. (2015) applied *Equations (17)*, *(18)* and *(19)* to calculate proppant embedment in the conditions under Lacy et al. (1998) conducted experiments in connection with proppant embedment. The results were compared and they found that the results obtained by using the analytical model were close to the experimental results. However, the analytical model resulted in smaller embedment values, and with increasing closure pressure the difference between the results gained in the two ways becomes greater. Reasons for the smaller values may be that the analytical model was derived from a single-layer pattern with ideal assumptions: for instance even paving, uniform size distribution, perfect sphericity of the proppant, and homogeneous fracture surface were assumed. Inhomogeneous fracture surface and uneven paving might result in unequal stresses on each proppant which could mean uneven embedment. In addition, the analytical model was derived essentially

on the basis of the linear elastic model. Therefore, conditions should be in the material linear elastic region in connection with stress, strain and deformation. This means that the model does not consider proppant crush at all, explaining why the model is more accurate in low closure stress region. Li et al. (2015) pointed out these values, and suggested closure pressure under 100 MPa and elastic modulus of proppant above 10,000 MPa to use this model. Considering this inaccuracy, fitting parameters were introduced into *Equation (19)*:

$$h = b_0 + b_1 \left\{ 1.04 D_1 (K^2 p)^{\frac{2}{3}} \left[\left(\frac{1-\nu_1^2}{E_1} + \frac{1-\nu_2^2}{E_2} \right)^{\frac{2}{3}} - \left(\frac{1-\nu_1^2}{E_1} \right)^{\frac{2}{3}} \right] + D_2 \frac{p}{E_2} \right\} \quad (20)$$

The fitting coefficients b_0 and b_1 can be determined by fitting with experimental data. This new equation was referred to as a revised new model (Li et al., 2015). By introducing the fitting coefficient, experimental measurement is required to be able to use it, so the revised new model is a semi-empirical one. It was emphasized in the section of introduction that the benefit of the analytical model is that one can use it on a wide range (actually for all cases), therefore the semi-empirical interest is out of this paper.

3.3. Multilayer Pattern Results

In the followings, two examples are introduced to demonstrate the results of the earlier derived equations *[Equations (17), (18), (19)]* resulted.

Figure 8 demonstrates how the proppant embedment, deformation, and the change in fracture aperture changes with increasing proppant size. The known parameters were taken to be $\nu_1 = \nu_2 = 0.2$, $E_1 = 10{,}000$ MPa, $E_2 = 1{,}100$ MPa, $p = 20$ MPa, $D = 5$ mm, and $D_2 = 20$ mm and the proppant diameter ranging from 0.2 to 1.6 mm.

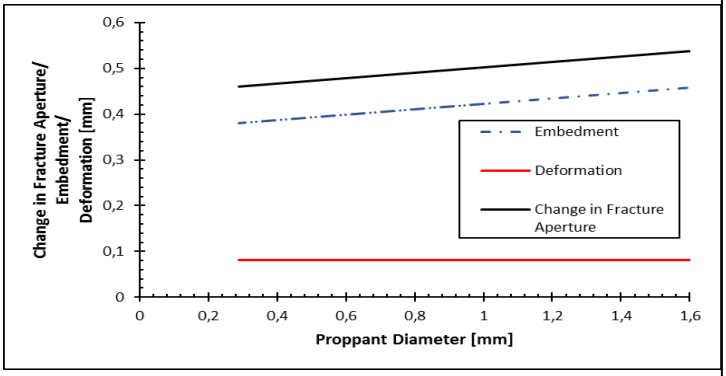

Figure 8
Relationship between the three variables and proppant diameter

Substituting these values into *Equations (17)*, *(18)*, and *(19)*, one can observe that deformation is a constant line while proppant embedment and the change in fracture aperture increases as the proppant diameter increases. Thus, the deformation is not affected by the proppant diameter, and as was expected from the equations, the change in fracture aperture is the sum of proppant embedment and deformation.

Figure 9 demonstrates how the proppant embedment, deformation, and the change in fracture aperture changes with closure pressure. The known parameters were taken to be $\nu_1 = \nu_2 = 0.2$, $E_1 =$ 10,000 MPa, $E_2 = 2{,}000$ MPa, $D = 5$ mm, $D_1 = 1.328$ mm (12/18 mesh size), and $D_2 = 20$ mm, and the closure pressure ranging from 0 to 20,000 psi. Substituting these values into *Equations (17) (19)*, one can observe that each of the three variable increases as the closure pressure increases, as was expected. In addition, since the elastic modulus of the proppant is relatively high compared to the elastic modulus of the formation (which is relatively low), the main cause of the change in fracture aperture is proppant embedment rather than proppant deformation.

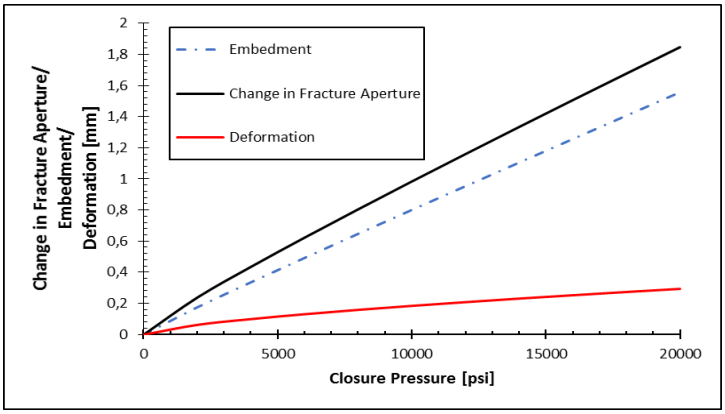

Figure 9
Relationship between the three variables and closure pressure

4. FRACTURE CONDUCTIVITY

4.1. Derivation

The main focus of this research is the influence of several factors on fracture conductivity which is the essence of hydraulic fracturing. Fracture conductivity is the product of the permeability and the fracture width. The permeability of a propped fracture is related to its porosity, the radius of the pore throat, and pore tortuosity. These parameters are influenced by the factors (proppant embedment, proppant deformation, and the sum of these: the change in fracture aperture) presented in the previous sections.

Yang and Wei (2004) derived a commonly used formula for permeability calculation expressed as:

$$k = \frac{\Phi r^2}{8\tau^2} \tag{21}$$

where k is permeability, in μm^2 (equal to 1 Darcy); Φ is the porosity, dimensionless; r is the radius of the pore throat, in μm; and τ is the pore tortuosity, dimensionless.

For the proppant pack shown in *Figure 7*, ignoring the pore-distribution differences in the layers, the equations of porosity, radius of the pore throat, and pore tortuosity can be easily derived using only mathematical considerations for the case when closure pressure is equal to zero. The equations are:

$$\phi_0 = \frac{4\sqrt{2}R_1^3 - \frac{4}{3}\pi R_1^3}{4\sqrt{2}R_1^3} = 0{,}25951 \tag{22}$$

$$r_0 = 1000\,\frac{2\sqrt{3}-3}{3}R_1 \tag{23}$$

$$\tau_0 = \frac{\sqrt{(\frac{2}{3}R_1)^2 + (\frac{\sqrt{2}}{3}R_1)^2}}{\frac{2}{3}R_1} = \frac{\sqrt{6}}{2} \tag{24}$$

where Φ_0 is the porosity of the proppant pack when closure pressure is equal to zero, dimensionless; r_0 is the radius of pore throat when closure pressure is equal to zero, in μm; τ_0 is the pore tortuosity when closure pressure is equal to zero, dimensionless; and R_1 is the radius of proppant, in mm.

When closure pressure is greater than zero, the porosity, radius of the pore throat, and pore tortuosity approximately satisfy the following relationships (Li et al., 2015):

$$\phi = \frac{D\phi_0 - 2\beta}{D - 2\beta} \tag{25}$$

$$r = \left(\frac{D-2\beta}{D}\right) r_0 \tag{26}$$

$$\tau = \sqrt{\left(\frac{D-2\beta}{D}\right)^2 (\tau_0^2 - 1) + 1} \tag{27}$$

where β is the proppant deformation calculated by *Equation (18)*, in mm, and D is the initial fracture aperture, in mm.

According to the concept of fracture conductivity and combining *Equations (21)*, *(25)*, *(26)*, and *(27)* the following equation can be obtained:

$$F_{CD} = kw = \frac{(D\phi_0 - 2\beta)(D-2\beta)r_0^2}{80\left[\left(\frac{D-2\beta}{D}\right)^2(\tau_0^2-1)+1\right]D^2}(D - 2\alpha) \tag{28}$$

where F_{CD} is the fracture conductivity, in μm*cm; w is the fracture aperture under closure pressure, in cm; and α is the half of the change in fracture aperture calculated by *Equation (17)*, in mm.

5. SENSITIVITY TEST

In this section, the most important sensitivity tests are presented in connection with fracture conductivity by analyzing these tests relevant consequences can be drawn. The main influencing factors which have impact on fracture conductivity are the closure pressure, proppant size, elastic modulus of proppant and formation, Poisson's ratio of proppant and formation, and initial fracture aperture. As mentioned before, the analytical model does not consider proppant crush and formation compatibility, and some additional assumptions were also introduced by derivation of the mathematical equations.

In addition, one should note that the conditions taken to conduct sensitivity tests are theoretical ones (generated by the author), but at the same time these can be fitted into a real situation as well.

5.1. Effect of Proppant Size

Figure 10 shows the results according to the parameters: $\nu_1 = \nu_2 = 0.2$, $E_2 = 2{,}000$ MPa, D = 5 mm, $D_2 = 20$ mm, p = 20 MPa, E_1 ranging from 2,000 to 100,000 MPa, and the proppant diameter ranging from 0.3 to 1.6 mm.

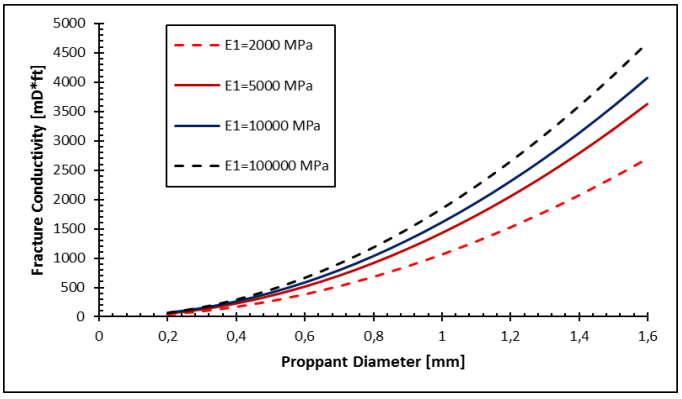

Figure 10
Fracture conductivity as a function of proppant diameter and elastic modulus of proppant

In *Figure 14*, one can observe that greater proppant diameter results in greater fracture conductivity. However, in the previous examples it was shown that increasing proppant size resulted in greater embedment, deformation, and change in fracture aperture. This is the result of proppant permeability, since greater proppant size means higher permeability. In *Equation (28)* one can see that the fracture conduc-

tivity depends on the square of the pore throat calculated at zero closure pressure, and the value of pore throat depends directly on the proppant diameter, so the proppant size modifies the permeability to a much greater extent than proppant embedment and deformation. The dependence of the fracture conductivity on the elastic modulus of the proppant can be also observed. The greater the elastic modulus of the proppant the higher the value of fracture conductivity, since proppant deformation is less effective in this case.

5.2. Effect of Closure Pressure

The conditions demonstrated in *Figure 11* were taken to be $\nu_1 = \nu_2 = 0.2$, E1 = 10,000 MPa, E2 = 2,000 MPa, D = 5 mm, $D_2 = 20$ mm, proppant size ranging from 12/18 mesh to 40/70 mesh and p ranging from 0 to 20,000 MPa. Fracture conductivity decreases when closure pressure increases and it can be also observed that with greater proppant size much higher fracture conductivity values can be achieved. However, when closure pressure increases the differences between fracture conductivity values related to different proppant sizes are much smaller.

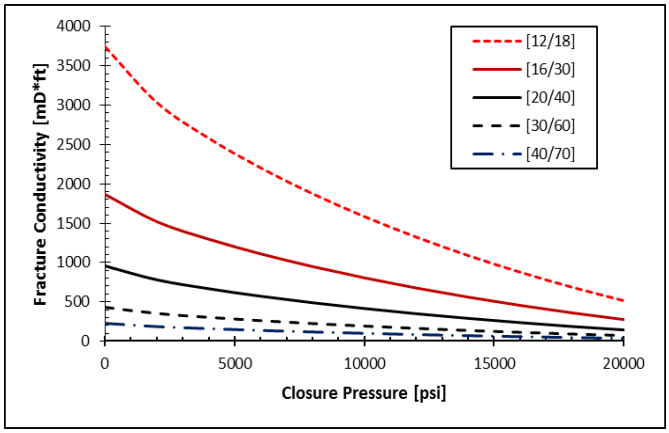

Figure 11
Fracture conductivity in function of closure pressure and proppant size

5.3. Initial Fracture Aperture

For *Figure 12* the same conditions were used as in the previous example. This test resulted in a very important conclusion; the fracture conductivity is highly dependent on the initial fracture aperture which is actually the initial fracture width. This conclusion is a key parameter in proppant selection.

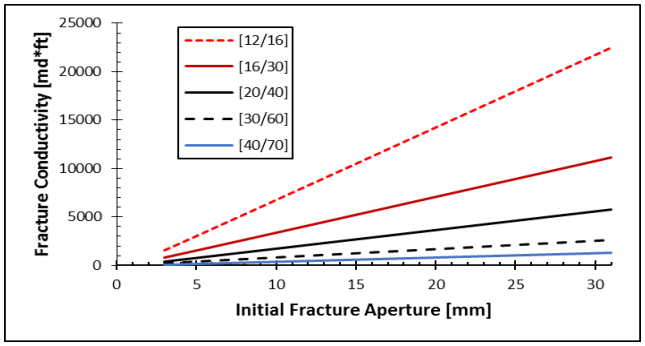

Figure 12
Fracture conductivity in function of initial fracture aperture

6. PROPPANT SELECTION

The purpose of this research was to develop an analysis system by which an in-depth investigation of proppant embedment can be performed, and based on this analysis system, a technical optimization of proppant selection can be established. The analytical model (Li et al., 2015) that was described and examined in the previous sections provides a deep understanding of proppant embedment. Combining the model with some other mathematical consideration and the Unified Fracture Design (Economides et al., 2002), a new method was developed for proppant selection.

6.1. Determining Initial Fracture Width

The analytical model introduced above requires several input parameters to calculate the actual proppant embedment, deformation, change in fracture aperture and finally fracture conductivity which is one of the most important parameters in connection with hydraulic fracturing.

Most of the parameters can be easily determined or approximated by some assumptions, but the initial fracture aperture is a critical value as shown in *Figure 20*, and it must be calculated precisely. To solve this problem, the relationship between the porosity and proppant concentration was used, which can be expressed as (Rivers et al., 2012):

$$\Phi = 1 - \frac{C_p}{w\rho_p} \tag{29}$$

where $\boldsymbol{\Phi}$ is the porosity, dimensionless; $\boldsymbol{C_p}$ is the proppant areal concentration, in lb/ft^2, $\boldsymbol{w}$ is the fracture width at zero closure pressure, in ft; and $\boldsymbol{\rho_p}$ is the proppant

density, in lb/ft^3. Rearranging *Equation (29)* one can obtain the following expression for initial fracture width calculation:

$$w = \frac{C_p}{(1-\phi)\rho_p} \tag{30}$$

Proppant pack porosity at zero closure pressure can be easily calculated by *Equation (22)* (or can be measured as well), proppant density is always given by the manufacturers, and the proppant concentration is an input parameter which can be determined by the Unified Fracture Design (UFD) model.

6.2. Unified Fracture Design

Economides et al. (2002) introduced a physical optimization method to maximize the productivity index of a hydraulically fractured well. It was referred to Unified Fracture Design (Economides et al. 2002). They introduced the concept of the dimensionless Proppant Number, N_{prop}, given by:

$$N_{prop} = \frac{2k_f V_p}{kV_r} \tag{31}$$

where k_f is the proppant pack permeability, in mD; V_p is the volume of proppant in the pay (the total volume injected times the ratio of the net height to the fracture height), in m^3; k is the reservoir permeability, in mD; and V_r is the reservoir drainage volume, in m^3. The concept of the dimensionless Proppant Number is an appropriate way to express the relative size of a given treatment, and it can be defined as the ratio of the propped volume of the fracture in the pay to the reservoir drainage volume, weighted by twice the related permeability ratio. It was established that for a given value of N_{prop} there is an optimal dimensionless fracture conductivity at which the productivity index is maximized.

The dimensionless fracture conductivity (C_{fD}) can be interpreted as the ratio of proppant pack permeability times the fracture width to the reservoir permeability times the fracture length, and it can be expressed as:

$$C_{fD} = \frac{k_f w}{kX_f} \tag{32}$$

Economides et al. (2002) also presented correlations for the maximum achievable dimensionless productivity index as a function of the dimensionless Proppant Number. Similarly, correlations were presented for the optimal dimensionless fracture conductivity for the entire range of Proppant Numbers. These correlations are expressed as follows:

$$C_{fD,opt}(N_{prop}) = \begin{cases} 1.6 & if\ N_{prop} < 0.1 \\ 1.6 + \exp\left(\frac{-0.583 + 1.48 ln(N_{prop})}{1 + 0.142\ ln(N_{prop})}\right) & if\ 0.1 \leq N_{prop} \leq 10 \\ N_{prop} & if\ N_{prop} > 10 \end{cases} \tag{33}$$

$$J_{Dmax}(N_{prop}) = \begin{cases} \dfrac{1}{0.990 - 0.5\ln(N_{prop})}, & N_{prop} \le 0.1 \\ \dfrac{6}{\pi} - exp\left[\dfrac{0.423 - 0.311N_{prop} - 0.089(N_{prop})^2}{1 + 0.667N_{prop} + 0.015(N_{prop})^2}\right], & N_{prop} > 0.1 \end{cases} \quad (34)$$

One should note that the absolute maximum dimensionless productivity index is $J_D = 6/\pi = 1.909$ which is the productivity index for a perfect linear flow in a square reservoir.

6.3. Method for Proppant Selection

Combining the UFD model with the previous mathematical considerations and the analytical model which was chosen to investigate proppant embedment, a simple way was developed to select the proper proppant size to provide sufficient fracture conductivity to achieve the predetermined productivity index.

The input parameters of the analytical model are: Poisson's ratios of proppant and formation (measured or estimated), elastic modulus of proppant and formation (measured or estimated), proppant size (manufacturer data determined by sieve analysis), closure pressure (can be calculated or measured), layer thickness (estimated value), and initial fracture aperture which can be calculated as a function of proppant concentration *[Equation (30)]*.

The input parameters of the UFD model are: injected proppant mass, formation height, reservoir drainage area, and reservoir permeability. These are the main parameters required to compute a simplified productivity index. To optimize the treatment and calculate a more accurate productivity index (considering turbulence effect and other skin factors) more complex models have been published (Economides and Martin, 2007; Lengyel and Pusztai, 2014), however, it is not necessarily required to demonstrate the results of this research.

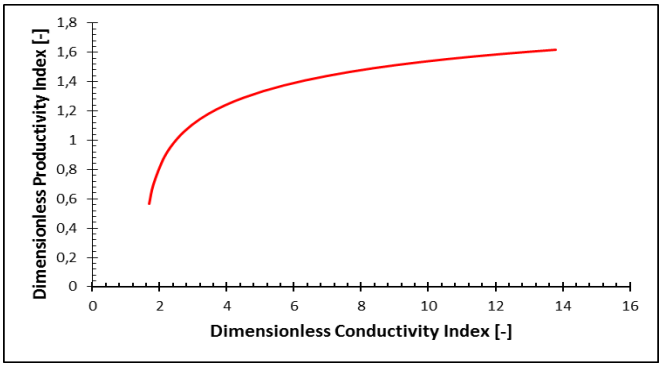

Figure 13
Dimensionless productivity index as a function of dimensionless conductivity index

The main input parameter of the combined method for proppant selection is the dimensionless productivity index which is predetermined by NPV calculations and what is the objective of the stimulation treatment. The operation of this proppant selection algorithm is the following: several treatment sizes are generated which means different dimensionless Proppant Numbers ($N_{prop)}$ are gained by generating injected proppant masses. In this process, dimensionless productivity index – dimensionless fracture conductivity curve is produced, as shown in *Figure 13*. From this curve, the dimensionless conductivity index can be determined from which the required fracture conductivity can be calculated *[Equation (32)]* using the optimal fracture length determined by the UFD model. This conductivity value can be compared to the value computed by the analytical model, and the decision can be made whether the selected proppant (which was the input parameter of the proppant embedment – fracture conductivity analysis) is sufficient or not.

7. FIELD EXAMPLE

7.1. Fracture Design Example

Service companies perform hydraulic fracturing designs with fracturing software. These kinds of programs are very sophisticated, and provide high accuracy, since a lot of experience has been integrated to develop them. A comparison was made between data from a fracturing design report and calculated values provided by the analytical model.

A fracturing treatment was designed with 16/30 sintered bauxite proppant with a mean diameter of 1,035 microns. The formation was considered to be a well consolidated Eocen sandstone and conglomerate with an elastic modulus of 10,000 MPa. The Young's modulus of proppant was equal to 7,270,000 psi which is approximately 49,500 MPa. The specific gravity of the proppant was 3.1. Poisson's ratios were not given, but 0.24 could be a good approximation for that (Lengyel, 2016).

This kind of software simulates the whole process step by step; for the given pumping rates and proppant concentrations, it computes the actual fracture width, conductivity etc. An average proppant concentration value of 10.8 kg/m^2 was calculated by the software, and the average propped fracture width was found to be 5.9 mm [the same fracture width value was obtained from *Equation (30)*]. The simulation result was 1,312 mD*m fracture conductivity.

Substituting the input parameters into the analysis system, the fracture conductivity was found to be 1,252 mD*m. The difference is only 60 mD*m which is more than sufficient to validate the model.

8. SUMMARY

In using well stimulations, the task of petroleum engineers is improving well productivity. In case of hydraulic fracturing, one of the most important parameters is the fracture conductivity which determines directly the productivity of the well.

The fracture conductivity is highly influenced by factors such as the elastic modulus of the proppant, elastic modulus of formation, proppant diameter, closure pressure, etc. An analytical model was chosen to gain a deeper understanding in this topic. Using the model, the proppant embedment, proppant deformation, change in fracture aperture, and fracture conductivity can be calculated.

Several sensitivity tests were carried out in this paper to investigate influencing parameters in connection with fracture conductivity. A number of conclusions could be drawn from the tests, which made it possible to create an analysis system for proppant selection.

The analytical model was combined with other considerations and with the optimization method referred to Unified Fracture Design. The combination enables us to optimize the proppant selection technically as a function of the productivity index.

ACKNOWLEDGEMENT

The described article was carried out as part of the EFOP3.6.116201600011 *Younger and Renewing University – Innovative Knowledge City – institutional development of the University of Miskolc aiming at intelligent specialisation* project implemented in the framework of the Szechenyi 2020 program. The realization of this project is supported by the European Union, cofinanced by the European Social Fund.

REFERENCES

[1] Economides, M. J., Martin, T. (2007): *Modern Fracturing. Enhancing Natural Gas Production*. E.T. Press, Houston, USA, pp. 93–169.

[2] Economides, M. J., Oligney, R. E., Valko, P. P. (2002): *Unified Fracture Design*. Orsa Press, Houston, USA, 2002a.

[3] Lacy, L. L., Rickards, A. R., Bilden, D. M. (1998, March 1): Fracture Width and Embedment Testing in Soft Reservoir Sandstone. *Society of Petroleum Engineers*, Volume 13, Issue 01, doi:10.2118/36421-PA.

[4] Lengyel, T., Pusztai, P. (2014): Hydraulic Fracturing Optimization. *Scientific Students' Associations Conference*, Faculty of Earth Science and Engineering, University of Miskolc, Miskolc.

[5] Lengyel, T. (2016): Investigation of Parameters Influencing Fracture Conductivity Including Proppant Pack Properties and Rock Mechanical Characteristics. *Scientific Students' Associations Conference*, Faculty of Earth Science and Engineering, University of Miskolc, Miskolc.

[6] Li, K., Gao, Y., Lyu, Y., Wang M. (2015): New Mathematical Models for Calculating Proppant Embedment and Fracture Conductivity. *Society of Petroleum Engineers*, Volume 20, Issue 03, doi:10.2118/155954-PA.

[7] Rivers, M., Zhu, D., and Hill, A. D. (2012): Proppant Fracture Conductivity with High Proppant Loading and High Closure Stress. *Society of Petroleum Engineers*, doi:10.2118/151972-MS.

[8] Wu, J. K., Wang, M. Z., and Wang, W. (2001): *Elastic Mechanics Introduction*. Recension of First edition, Beijing, Peking University Press, Chinese, pp. 200–203.

[9] Yang, S. L., Wei, J. Z. (2004): *Reservoir Physics*. First edition, Beijing, Petroleum Industry Press, Chinese, pp. 136–159.

Geosciences and Engineering, Vol. 7, No. 10 (2019), pp. 136–143.

SIZE DEPENDENCE OF THE COMPOSITION OF CEMENT KILN DUST

C. LANZERSTORFER

University of Applied Sciences Upper Austria

Abstract: In cement mills large amounts of dust are separated from the kiln off-gas by the de-dusting filters. The specific generation of cement kiln dust (CKD) is said to be in the range of 50–200 kg per tonne of cement clinker produced. In some mills this dust can be mixed into the product, while in other mills it has to be utilized elsewhere or is sent to landfill, depending on the chemical composition of the dust. In this study, the CKDs from three different cement mills were investigated with the focus on the size dependence of the composition. Prior to chemical analysis the CKDs were split into four size fractions by air classification. After digestion, the concentration of various metals (Ca, Cd, Co, Fe, K, Mg, Mn, Pb and Zn), of total carbon (TC) and anions (Cl^- and SO_4^{2-}) was determined. For the heavy metals Cd, Pb and Zn pronounced size dependence was found with considerably higher concentrations in the fine size fractions. Similar but less pronounced size dependence was found also for the anions and for K. The concentration of Ca, Fe and TC showed no distinct size dependence. Thus, air classification might be applied for CKD pre-processing in CKD-utilization, for example to produce heavy-metal-reduced or chloride-and-sulfate reduced fractions.

Keywords: *Cement kiln dust, CKD, heavy metals, chloride, sulfate*

1. INTRODUCTION

In the burning of clinker in rotary kilns for cement production large amounts of dust are generated. The dust is separated from the kiln off-gas by means of electrostatic precipitators (ESPs) or fabric filters before it is released into the atmosphere. The specific generation of cement kiln dust (CKD) is in the range of 50–200 kg per tonne of cement clinker produced [1]. In several cement plants the CKD can be re-incorporated in the clinker production cycle. However, this is possible only when the limits for the alkali and chloride concentration in cement are not exceeded. If not, alternative ways of CKD utilization have to be found or the CKD has to be deposed off in landfill sites [2]. Such alternative applications include agriculture (potash/lime source), civil engineering (soil stabilization), building materials (lightweight aggregates, low-strength concrete), sewage and water treatment (coagulation aid, sludge stabilization) and pollution control (sulfur absorbent, waste treatment) [3–6]. There is even the standard ASTM D 5050-08 available guiding the use of CKD.

CKDs from cement kilns with a cyclone preheater system are quite fine-grained powders. The reported mass median diameters are in the range from 10 μm to

18 µm [4, 5]. The chemical composition of CKD is described in several studies [3–6]. *Table 1* shows data from various studies. However, there is no information available on the size dependence of the dust composition.

Table 1

Chemical composition of CKD

	[7]	[3]	[4]	[5]	[8]	US EPA, cited in [9]	[6]	[10]
Samples	4	4	6	4	1	17 (Median)	1	1
Main components in %								
Al_2O_3	2.7–5.1	3.4–5.5	2.5–50	2.2–4.7	5.6		4.5	
Fe_2O_3	2.0–3.5	1.9–2.3	1.4–3.1	1.7–2.3	2.2		2.9	
SiO_2	9.0–15.7	10–18.6	9–20	11.9–16.4	15		11.6	
CaO	45.5–57.0	51–60	35–57	37.4–55	43.6		42	
MgO	1.0–3.1	1.6–3.3	1.0–4.1	1.2–2.7	0.8		1.3	
K_2O	5.3–6.1	2.8–14.3	2–11	1.4–7.0	3.0		0.6	2.5
SO_3	5.7–16.7	4.0–11.1	4–20	4.2–14.6			0.5	
Cl		2.4–6.4						
LOI	9.6–25.5	3.1–13.5	5–22	3.9–29.6	27.3		35.5	
Heavy metals in mg/kg								
Cd						4.6		4.7
Co					25			
Cr					81	18.1	75	
Mn				350–3100	155			
Ni					59	15.9	94	8.8
Pb					573	287		52.7
Zn					525		53	24.7

Air classification is a cost-effective pre-treatment method which can be applied to separate fine-grained material into different size fractions [11]. This can be beneficial when the composition of the material is size dependent. Therefore, in this study the composition of the CKDs from three cement mills was investigated by particle size.

2. MATERIALS AND METHODS

The CKD samples investigated were collected from the dry de-dusting system of three industrial cement plants. The samples were collected at the dust discharge of the de-dusting systems of the cyclone preheater kiln systems. Sample A was collected when the kiln system was in direct operation mode where the kiln off-gas is de-dusted directly after the cyclone preheater outlet. Samples B and C were collected when the off-gas from the cyclone preheaters was utilized in a combined raw meal grinding and drying unit. The sample volumes of approximately 2 dm^3 were reduced to an amount suitable for the various laboratory tests using sample dividers, which were applied repeatedly (Haver RT 12.5, Quantachrome Micro Riffler).

A laboratory air classifier 100 MZR from Hosokawa Alpine was used for dry classification of the CKD samples. In the first classification step, the finest size fraction was separated from the bulk of the dust. The remaining coarse fraction was used as feed material in the next classification step, where the classifier was operated at reduced speed. A detailed description of such a sequential classification procedure can be found elsewhere [12]. The speed of the classifier in the three classification runs was 21,000, 11,000 or 6,000 rpm and the air flow through the classifier was 50 m³/h.

The dust particle size distribution was measured using a Sympatec HELOS/ RODOS laser diffraction instrument with dry sample dispersion. The instrument was calibrated using a SiC-P600'06 standard from Sympatec.

The total carbon content (TC) was determined using a vario TOC select system in solid mode from Elementar Analysensysteme. For calibration of the system an Elementar Analysensysteme soil standard with 4.1% TOC/TC was used. The loss on ignition (LOI) was determined at 850 °C using a muffle furnace.

For analysis of metals and sulfate the samples were digested using aqua regia, while for the determination of the Cl^- content the samples were leached with deionized water. The concentration of Cl^- in the samples was measured by ion chromatography (IC) using an ICS-100 from Dionex. The concentration of various metals (Cd, Co, Cr, Fe, Mn, Ni, Pb and Zn) was determined by inductively coupled plasma optical emission spectroscopy using a Horiba Jobin Yvon Ultima 2 system. The concentration of K, Mg, Ca, Cl^- and SO_4^{2-} was measured by ion chromatography. Details of the analytical method can be found elsewhere [13]. The measured concentrations of Cr and Ni cannot be used because the dust becomes contaminated with these elements during the classification procedure due to some erosion of the classifier wheel [14].

3. RESULTS AND DISCUSSION

3.1. CKD Size fractions

The mass median diameter of the size fractions produced was quite similar because the operation parameters in the classification procedure were the same for all three CKDs. The mass median diameters of SF1, SF2, SF3 and SFG4 were 1.3 ± 0.1 μm, 3.0 ± 0.5 μm 6.5 ± 1.3 μm 17.4 ± 3.0 μm, respectively. The slightly different size distributions of the CKDs resulted in somewhat different mass fractions of the size fractions *(Table 2)*. The particles size distributions of the CKD A size fractions are shown in *Figure 1* as an example.

Table 2

Mass fractions of the various size fractions

CKD	SF1	SF2	SF3	SF4
A	0.196	0.284	0.390	0.130
B	0.183	0.299	0.397	0.121
C	0.233	0.428	0.252	0.087

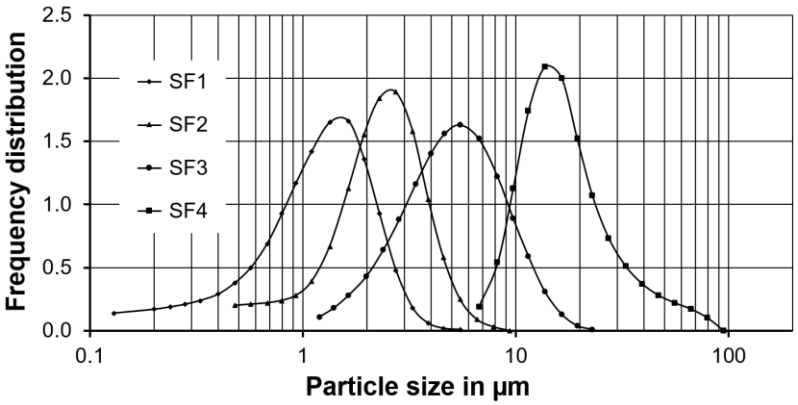

Figure 1
Particle size distribution of the size fractions produced from CKD (Sample A)

3.2. Composition of the CKD size fractions

The results of the chemical analysis are summarized in *Table 3* (main components) and *Table 4* (heavy metals).

Table 3
Composition of CKD size fractions: Main components in g/kg dry dust

	Ca	Mg	TC	K	Cl	SO_4^{2-}	Fe	LOI
CKD A	284	2.0	95	11.50	9.6	11.0	8.3	353
SF1	264	1.5	86	15.5	11.8	20.0	10.0	330
SF2	296	1.5	93	11.0	8.5	12.0	8.0	350
SF3	318	2.0	100	9.1	8.1	6.0	8.0	369
SF4	315	2.0	95	13.1	12.4	4.5	10.3	363
Recovery	106%	93%	100%	104%	100%	90%	104%	101%
CKD B	280	2.0	97	4.0	3.1	8.90	9.7	350
SF1	313	2.0	90	3.5	4.0	15.00	10.8	340
SF2	329	2.0	95	4.1	3.0	9.00	10.0	344
SF3	256	2.0	94	3.9	3.2	8.00	10.2	344
SF4	326	3.0	91	3.5	1.7	9.00	13.4	338
Recovery	106%	106%	96%	96%	100%	109%	109%	98%
CKD C	334	2.2	105	4.9	4.8	4.0	6.5	381
SF1	320	2.0	107	5.1	5.9	6.0	8.2	384
SF2	355	2.0	106	4.5	5.3	4.0	7.1	387
SF3	331	3.0	104	4.0	4.2	3.0	5.5	378
SF4	311	4.0	98	3.8	3.7	2.5	5.7	355
Recovery	101%	110%	100%	91%	104%	102%	106%	100%

The recovery of the components in the size fractions was in the range of 90% to 110%. An exception from this is evident for the recovery of Cr and Ni, where the recovery was significantly higher. This is a result of some erosion of the classifier wheel, which is made of stainless steel (Lanzerstorfer, 2015b).

The main component in the CKDs was Ca. The carbon (TC) contained in the dust can be assumed to be present as carbonate. Thus, the amount of CO_2 calculated from the TC fits well with the measured value of the LOI. The molar ratio of Ca+Mg to the calculated CO_2 was close to 1.0.

The results show little dependence of the concentration on the particle size for the main components Ca and TC *(Figure 2)*. This is quite reasonable because $CaCO_3$ is usually the main component in CKDs [3–6]. For the anions Cl^- and SO_4^{2-} some size dependence of the concentrations was found. This dependence is more expressed for SO_4^{2-} than for Cl^- *(Figure 2)*. In the coarsest size fraction of CKD A the concentration of Cl^- was increased. No explanation has been found for this deviation from the general trend for the moment. The concentration of K showed a similar trend.

Table 4

Composition of CKD size fractions: Heavy metals in mg/kg dry dust

	Mn	Cd	Co	Cr	Ni	Pb	Zn
	472	0.48	1.9	26.0	7.5	14.8	n.a.
SF1	379	0.90	2.4	29.4	14.4	24.6	n.a.
SF2	408	0.61	2.0	26.9	11.3	18.7	n.a.
SF3	500	0.32	1.7	30.9	10.5	11.6	n.a.
SF4	973	0.13	1.6	55.8	12.0	3.6	n.a.
Recovery	108%	102%	103%	126%	156%	102%	n.a.
CKD B	662	0.48	2.6	27.6	13.0	41.8	n.a.
SF1	591	0.94	3.9	33.1	26.6	82.0	n.a.
SF2	585	0.52	2.2	30.9	16.6	44.5	n.a.
SF3	768	0.45	2.4	36.7	16.8	35.0	n.a.
SF4	1083	0.16	2.2	54.1	19.3	17.2	n.a.
Recovery	109%	109%	100%	132%	145%	106%	n.a.
CKD C	192	0.68	2.1	12.6	15.1	57.1	47.8
SF1	211	0.94	2.4	21.8	25.1	78.8	77.9
SF2	197	0.81	2.5	17.9	18.7	53.3	49.3
SF3	184	0.32	1.1	15.1	14.9	34.3	29.6
SF4	184	0.13	0.5	16.4	14.6	29.8	15.0
Recovery	102%	97%	93%	142%	125%	92%	101%

n.a. not analyzed

The concentration of the heavy metals Pb and Cd shows distinct size dependence with increased concentrations in the finest size fractions *(Figure 2)*. For Pb this dependence is similar to that reported for a cement kiln by-pass dust [15]. The same was observed for Zn *(Table 3)*. These metals are volatile at cement kiln conditions, which means that they can leave the kiln as gaseous components. When the kiln off-gas cools down in the cyclone preheater system, the heavy metals recondense on the surface of the dust, which pass partly through the preheater system with kiln off-gas. Since the finer particles have a larger specific surface area, higher concentrations of these heavy metals result in the finer size fractions.

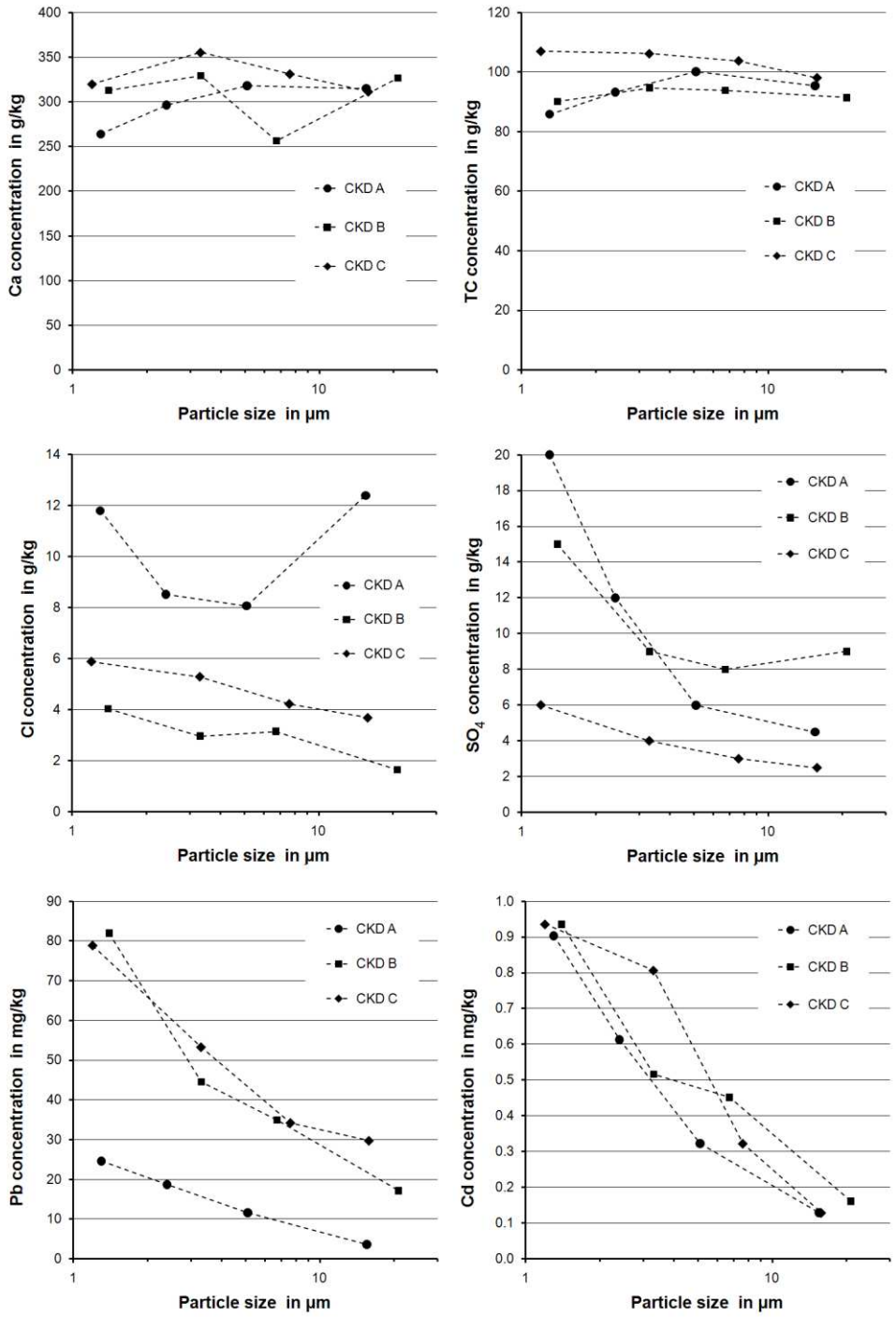

Figure 2

Size dependence of the concentration of Ca, TC, Cl^- and SO_4^{2-}, Pb and Cd

4. CONCLUSIONS

The classification experiments with CKD from three different cement mills showed that the size dependence of the concentration of various elements is quite similar for the different CKDs. For the heavy metals Cd, Pb and Zn pronounced size dependence was found with considerably higher concentrations in the finest size fractions. For the anions Cl^- and SO_4^{2-} as well as for K the size dependence was less. The concentrations of Ca, Fe and TC showed no distinct size dependence at all. Thus, air classification is a potential method for CKD pre-processing in CKD utilization, for example to produce heavy-metal-reduced or chloride-and- sulfate reduced fractions for recycling to the raw meal.

ACKNOWLEDGEMENT

Laboratory work by D. Lampl is gratefully acknowledged.

REFERENCES

[1] Institute for Prospective Technological Studies (2013): *Best Available Techniques (BAT) Reference Document for Production of Cement, Lime and Magnesium Oxide: Industrial Emissions Directive 2010/75/EU (integrated pollution prevention and control)*. Study, Sevillia (Spain), European Commission.

[2] Maslehuddin, M., Al-Amoudi, O. S. B., Shameem, M., Rahman, M. K., Ibrahim, M. (2008): Usage of cement kiln dust in cement products – Research review and preliminary investigations. *Construction and Building Materials*, Vol. 22, pp. 2369–2375.

[3] Lachemi, M., Hossain, K. M. A., Shehata, M., Thaha, W. (2008): Controlled low strength materials incorporating cement kiln dust from various sources. *Cement and Concrete Composites*, Vol. 30, pp. 381–392.

[4] Mackie, A., Boilard, S., Walsh, M. E., Lake, C. B. (2010): Physicochemical characterization of cement kiln dust for potential reuse in acidic wastewater treatment. *Journal of Hazardous Materials*, Vol. 173, pp. 283–291.

[5] Peethamparan, S., Olek, J. Lovell, J. (2008): Influence of chemical and physical characteristics of cement kiln dusts (CKDs) on their hydration behaviour and potential suitability for soil stabilization. *Cement and Concrete Research*, Vol. 38, pp. 803–815.

[6] Pavia, S., Regan, D. (2010): Influence of cement kiln dust on the physical properties of calcium lime mortars. *Materials and Structures*, Vol. 43, pp. 381–391.

[7] Konsta-Gdoutos, M. S., Shah, S. P. (2003): Hydration and properties of novel blended cements based on cement kiln dust and blast furnace slag. *Cement and Concrete Research*, Vol. 33, pp. 1269–1276.

[8] Eckert Jr, J. O., Guo, Q. (1998): Heavy metals in cement and cement kiln dust from kilns co-fired with hazardous waste-derived fuel: application of EPA leaching and acid-digestion procedures. *Journal of Hazardous Materials*, Vol. 59, pp. 55–93.

[9] Kunal, Siddique, R., Rajor, A. (2012): Use of cement kiln dust in cement concrete and its leachate characteristics. *Resources, Conservation and Recycling*, Vol. 61, pp. 59–68.

[10] Zhou, W., Beck, B. F., Wang, J., Pettit. A. J. (2007): Groundwater monitoring for cement kiln dust disposal units in karst aquifers. *Environmental Geology*, Vol. 52, pp. 761–777.

[11] Lanzerstorfer, C. Angerbauer, A., Gaßlbauer, M. (2018): Feasibility of Air Classification in Dust Recycling in the Iron and Steel Industry. *Steel Research International*, 89 (7), 1800017, pp. 1–6.

[12] Lanzerstorfer, C., Kröppl, M. (2014): Air classification of blast furnace dust collected in a fabric filter for recycling to the sinter process. *Resources, Conservation and Recycling*, Vol. 86, pp. 132–137.

[13] Lanzerstorfer, C. (2015): Chemical composition and physical properties of filter fly ashes from eight grate-fired biomass combustion plants. *Journal of Environmental Sciences*, Vol. 30, pp. 191–197.

[14] Lanzerstorfer, C. (2015): Investigation of the contamination of a fly ash sample during sample preparation by classification. *International Journal of Environmental Science and Technology*, Vol. 12, pp. 1437–1442.

[15] Lanzerstorfer, C. (2016): Residue from the chloride bypass de-dusting of cement kilns: Reduction of the chloride content by air classification for improved utilization. *Process Safety and Environmental Protection*, Vol. 104, pp. 444–450.

Geosciences and Engineering, Vol. 7, No. 10 (2019), pp. 144–157.

DIFFERENCES BETWEEN STEADY-STATE AND TRANSIENT SIMULATIONS OF MASS TRANSPORT IN A RIVER-INFLUENCED SHALLOW AQUIFER

ANDREA KOLENCSIK TÓTH

Institute of Environmental Management, University of Miskolc

Abstract: This paper presents the results of numerical groundwater flow and contaminant transport simulations assuming different flow conditions of a river influenced aquifer. The purpose of the study was to compare the simulated dissolved plume movement in steady-state and in transient flow fields showing the effects of the river for transport phenomenon. The differences in advective and dispersive transport were examined by computing the flow velocity fields, flow path lengths and dispersion in space and time. In transient simulation the flow velocities and flow directions change through time periods, and the effects of river floods can be incorporated. While in the steady-state model a constant, average flow field is assumed. Significant differences were detected in the flow paths between the two modelling approach. The flow path lengths across perpendicular sections showed that water particles – including dissolved contaminants – take longer paths approaching the river in steady-state simulation. The calculated dispersion was also different for the steady-state and for the transient simulations. During flood periods the steady-state model underestimates the dispersion of contaminants. The overall impacts of these differences, that the dissolved plume moves slower toward the river in the transient case compared to the steady-state simulation.

Keywords: *numerical simulation, transient flow field, plume movement, river influenced transport*

1. INTRODUCTION

Rivers can drain or feed aquifers and depending on the strength of connection they can influence the groundwater flow conditions. Due to changes in river stages, the groundwater level can be constantly changing in a dynamic way. The hydraulic impact of a river is complex, and not only the narrow riparian zone is influenced. The river affects the groundwater flow velocity, the flow gradient and flow direction even over long distances and even by a short flood period. As a result, transport phenomena in the aquifer can also be influenced by the connected surface water and can be dependent on the actual state and time variability of the groundwater flow system.
Generally, in the relationship between surface and groundwater there may be two conditions: the surface water body either drains or recharges the groundwater. The difference in hydraulic potential between the two elements determines the flow condition. If the groundwater level is higher than the river stage, groundwater flows into the river. If the groundwater table is lower than the river stage, the river supplies the

groundwater [1]. River-groundwater relations can change over time due to changes in its water levels. In case of gaining rivers, for short periods water can move from the river into the adjacent aquifer (bank storage) as a consequence of increasing river stage because of storm rainfall or rapid snowmelt. The effects of bank storage are temporary, but it may take some hours or weeks for the stored water to be released back into the river, and thus it can have a significant impact on the groundwater flow conditions [2] [3]. Depending on the frequency and magnitude of increases in river stage, some rivers and adjacent shallow aquifers may be in a continuous state of readjustment from interactions related to bank storage [1]. This time-variable interaction plays an important role in the study of exchanging water and solutes.

In Hungary the river beds partially penetrate the shallow aquifers; full penetration is rare [4], but a hydraulic connection generally exists between the river and groundwater. In their natural state Hungarian rivers are gaining rivers in most of the year, but during wet periods they can support the groundwater through bank storage. The daily water demand of 40% of Hungarian population is satisfied by bank-filtered water resources [5]. 75% of the potential water resources are also bank-filtered, so they play a big role in future water resource management. At the same time several industrial sites are located near surface water bodies, where potential or existing pollution of groundwater can contact the surface water. In some areas groundwater can be a major and potentially long-term contributor to contamination of surface water.

Most of the current research on the relationship between rivers and groundwater in Hungary is closely related to bank-filtered water resources. The studies focus on the ratio of river water in the produced water based on tracers [6] [7], or the suitability of perspective bank-filtered water resources for production [8]. There is also research related to the estimation of recharge based on isotope measurements [9] and to more accurately clarify the spatial variability of hydrogeological structures [10]. Results of field investigations are typically valid only for a limited time period and do not reflect changes in the flow system over time [4] [11].

In numerical modeling practice a steady-state approach is generally accepted and used, which does not consider the temporal changes in groundwater flow velocities because of river stage fluctuation. With a steady-state flow model, specific flow conditions can determined grabbed related to different states of the river (low, average, high river stage), assuming the long-term existence of such flow conditions. In most cases it is a sufficiently accurate approximation of the underground flow processes, and at the same time the most easily feasible modeling task with the lowest data demand. However, solute transport simulations based on a steady-state flow model may only be a simplified estimation of the dissolved plume migration and cannot be used for future forecasts.

There are only a few studies aiming at the evaluation of the river-groundwater relationship based on high-resolution, transient numerical modeling [12] [13], and they focus on the hydrodynamic processes. Transport simulations with high temporal resolution are also applied for the better understanding of surface water-groundwater interaction. Simulation of tracers (temperature, tritium) based on field experiments are the latest research approach [14] [15]. At the same time, there is a need for

research to highlight the limitations of numerical calculations for contamination movement in the special case when a river strongly influences the groundwater flow conditions.

The objective of the research is to examine the difference in simulated contaminant plume movement when using a steady-state and a transient flow model. The aim is to determine how flood periods and temporal changes in the river stage, and as a result, changes in groundwater flow velocities can influence advective and dispersive mass transport processes. The question is which approach is capable of more accurately forecasting the movement of a contaminant plume when using numerical simulation, a steady-state flow model or a transient flow model.

2. METHODS

2.1. Background study

A calibrated steady-state and transient flow model of a river-influenced aquifer was used for the analysis. The previous study contains a detailed description of the investigated site and the flow modeling processes [16], here just a brief summary is given.

The site of interest is located in central Hungary at the riverside of the Tisza River. From a geological point of view the shallow aquifer (20 m thick) is part of an alluvial plain, and consists of gravelly formations with high permeability. During the site investigation a large monitoring system was established and pumping tests and long-term hydraulic head measurements were carried out [16]. The system provided enough information to accurately describe the regime of groundwater-surface water (GW–SW) interaction at a distance from the river up to 3,000 m.

Based on the groundwater monitoring data, it was possible to track a strong effect of the fluctuating river level on the hydraulic head field. In flood periods in addition to surface water entering the aquifer, the groundwater flow direction and gradient of the flow field change. Up to a certain distance (a maximum of 1,200–1,400 m) from the river the flow direction can turn in the opposite direction [16].

In the first step, based on the accurate geological structure and hydraulic head field from the detailed site investigation, a steady state flow model was created, assuming a long-term average of river stages and average state of the flow system. The model was built using Processing MODFLOW software [17], which applies the MODFLOW code for numerical calculation of groundwater flow [18] and MODPATH [19] for particle tracking.

The direction of average groundwater flow (*Figure 1*, dashed line) is from NW-W to SE-E due to the dominantly discharging Tisza River, which was included in the model as permanent boundary condition. The steady-state model was calibrated to average groundwater levels of the monitoring wells.

For further investigation the use of a very detailed transient flow model of the site was necessary to accurately describe the dynamic changes of groundwater flow. The transient model has a very high time resolution with periods of 5–10 days, and a total simulation time of 30 years. The river stage fluctuations were simplified and were

built into the model using time-variant head boundary package to continuously change the river heads during the simulation. The transient model was calibrated with a multistep calibration process [16] using the groundwater head time series, the river-groundwater level correlation, and time delays of river floods.

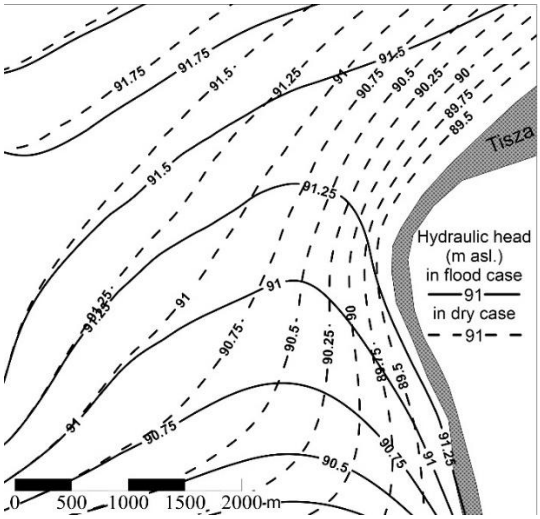

Figure 1
The investigated site with two calculated hydraulic potential fields

2.2. Contaminant sources

After the flow modeling process hypothetical contaminant sources were positioned at different distances from the river. The sources of groundwater contamination were identified as point sources. The sources were assumed to be constant concentration cells in the model grid over the simulated time. Assuming constant concentrations in the source area of a plume in time is a representative and commonly used solution for contaminant sources, including landfills, storage facilities, which continuously release the pollutant to groundwater. Another example is when the contaminated soil itself behaves as a constant source through the phenomena of dissolution and diffusion.

The value of initial concentration (c_i) was arbitrarily chosen as it was a theoretical examination. One consideration was that initial value of contaminant should be high enough to ensure a high concentration-gradient (c_i/c_b = 10,000) for easy identification of the delineation of the calculated plume from the background. *Figure 2* shows the locations and parameters of the contaminant sources.

Among the possible transport processes, advection and mechanical dispersion were simulated, as the main purpose was determining the impact of flow conditions on the plume movement. The advective velocity is equal to groundwater flow velocity, and mechanical dipsersion is dependent on advective velocity. It was assumed that the changing groundwater flow velocities influence the dissolved plume migration through advection and dispersion, varying over time.

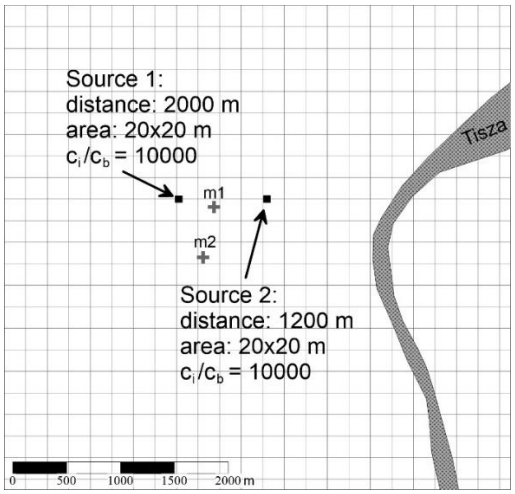

Figure 2
The theoretical contaminant sources

2.3. Mass transport by advection and dispersion

The term advection refers to the transport of a solute by the bulk movement of groundwater and the movement of particles within flowing water. The one-dimensional flux of a solute through a porous medium can be expressed by the equation below, assuming that the transport of mass does not affect the pattern of flow [20]:

$$J = v_x \cdot c \cdot n_e \tag{1}$$

where:
J = mass flux per unit area per unit time
v_x = average linear groundwater velocity in the direction of flow
c = concentration in mass per unit volume of solution
n_e = effective porosity of the geological medium.

For most practical problems it can be assumed that dissolved mass and groundwater will move at the same advective rate [20]. This assumption, however, is not true if, for example, the solute and the groundwater have a significantly different density, causing the flow of mass and water to diverge.

In this study the simulation is not complicated by density differences so the advective mass flux between the model cells is calculated based on the groundwater flow velocities (1). In the steady state model, the flow velocity of each model cell is constant in time, but spatial variability can occur because of an inhomogenous hydraulic conductivity field and changing hydraulic gradient. In the transient simulation the velocity also can change in time with changing river stage through the time periods.

Mechanical dispersion is caused by the different flow paths water particles take in a geological medium. Some of the flow paths are faster because they follow a more direct path, or because they are going through larger pores. This is the case through the center of pores, in which water flows faster because less friction is involved. Other flow paths may be slower because they are closer to the grain boundaries, thus being exposed to more friction in the pore throat, slowing down the water particles. The phenomenon of mechanical dispersion causes mechanical mixing and dilution of the solute within the bulk movement of groundwater [21].

The numerical value of mechanical dispersion [L^2/T] is the product of advective groundwater velocity [L/T] and dispersivity [L]. Dispersivity is a characteristic property of the geological medium, and differs in value for each of the spatial components. In this study the value of the dispersion coefficient was assumed to be 10 m in each simulation. This input parameter was constant in space and time. At the same time, the calculated dispersion can change because of varying flow velocities. Flow velocities increase approaching the river, because of the increasing hydraulic gradient. In the transient simulations the calculated groundwater flow velocities of each model cell are also varied through the periods.

3. RESULTS OF THE SIMULATIONS

3.1. Steady-state and transient flow paths

A steady-state model calibrated to an average flow condition was compared to a calibrated transient flow model. First 60 particles were placed distributed randomly in the model domain. The particles were tracked for 10 years forward in the flow field. The needed flow velocity fields for particle tracking were computed by MODPATH [19].

In *Figures 3* and *4* the difference in water particle movement between steady-state and transient flow fields is illustrated. The particles were placed at the same initial points of the model area for the two types of simulation. At first sight several differences are visible: the total length of the flow paths, the movement of water particles and the resultant direction of the flow paths may differ. The effect of changing flow directions can be detected in the movement of each water particle in case of the transient flow field. The dissolved contaminants move together with the water particles in the same way, which can cause a difference in its advective and dispersive transport between the steady-state and transient cases.

For numerical characterization of the difference, the components of the velocity vectors for each model cell were computed. Vector components which point in the main flow direction toward the river were separated. Then the total flow lengths cumulated for a 1-year simulation time for each model cell were calculated along sections perpendicular to the river. The calculated flow path lengths are presented for 3 sections in the case of both steady-state and transient simulations in *Figure 5*.

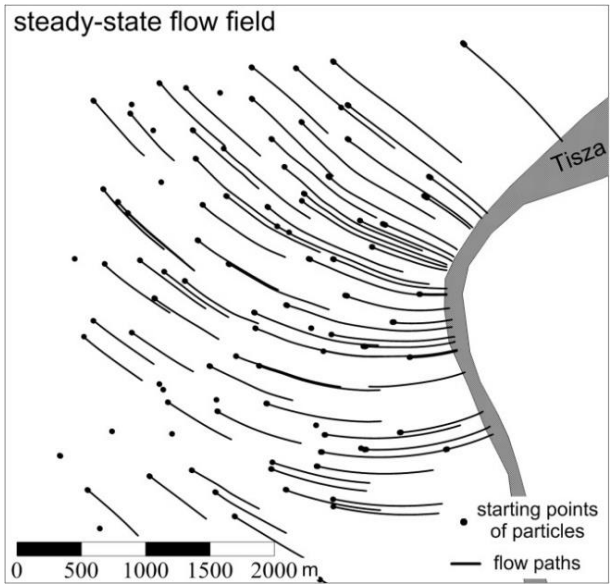

Figure 3
Results of particle tracking for 10 years in case of steady state simulation

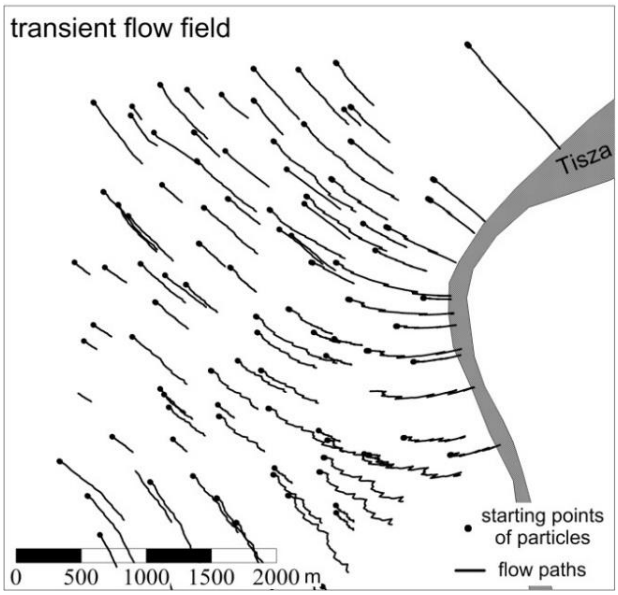

Figure 4
Results of particle tracking for 10 years in case of transient simulation

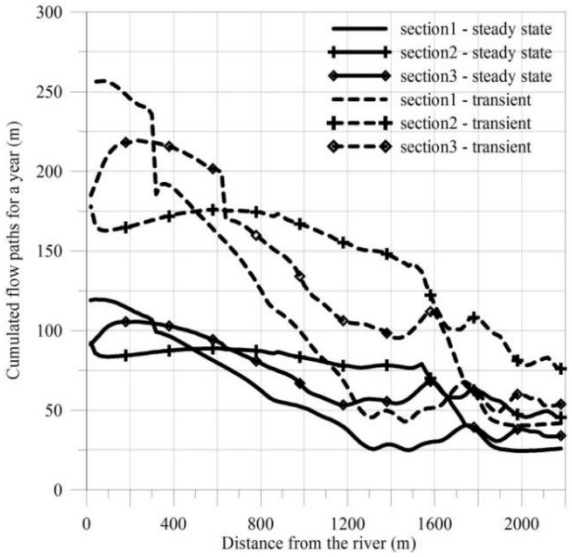

Figure 5
Cumulated flow path lengths with distance from the river

The three curves of each simulation do not match because of the inhomogenous model domain. The flow paths generally increase approaching the river in the steady-state and in the transient case, too, as the flow velocities themselves are higher along the riverbank.

At the same time the flow paths are different for the transient and steady-state model, and the difference increases as the river is approached. In transient flow field there are longer total flow paths. Because of the continuously changing flow directions, the water particles move not only in the main flow direction but they also "step back" several times, depending on the distance from the river. This can cause slower overall plume movement toward the river. It can also have consequences for the transport processes since more intensive dilution and dispersion can happen in the transient flow field along the riverbank, which causes smaller concentrations at the plume edges.

3.2. Steady-state and transient dispersion fields

Not only the advective transport is responsible for the dynamic movement of a dissolved plume. The process of dispersion near the river is of great importance in the movement of pollution, since the increasing velocities and changing flow direction lead to increasing dispersion approaching the river. The dispersion reduces the concentrations of dissolved pollutants and can result in greater dilution.

Dispersions were calculated along sections based on the flow velocity fields as the product of dispersivities and the cell's flow velocities. *Figure 6* shows the dispersion distribution (continuous line) obtained with a permanent model calibrated

for average water flow conditions. In contrast, the results presented with dotted lines were obtained by calculating the hydrodynamic dispersion for two states of a transient simulation, a low water level and a high water level state.

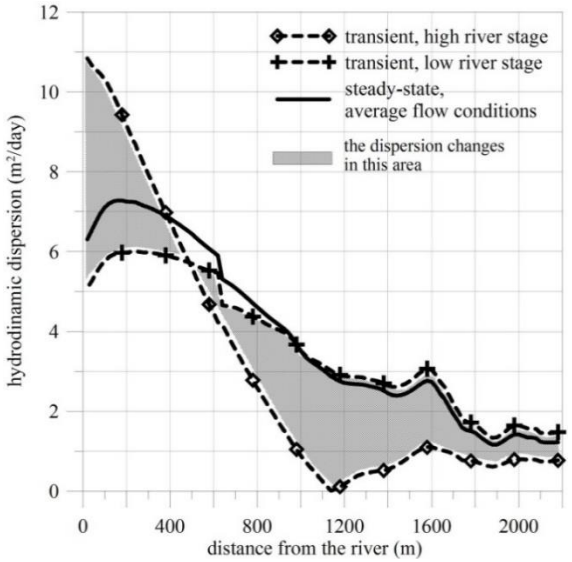

Figure 6

Calculated hydrodynamic dispersion along a section for the steady state flow and for two states of transient flow

The results show that dispersion calculated by the steady-state average groundwater flow simulation is underestimated approaching the river, and moving away it is overestimated during flood (or high river stages) periods. The reason can be found in the nature of the velocity vector space. During a losing river situation (when river stages are higher than the groundwater level) there is a distance where the flow velocity is theoretically reduced to zero. This is the distance of turning flow direction. At this point there is no groundwater moving to cause dispersion. At the same time, the flow velocities near the river can be extremely high because of the high hydraulic gradients during floods.

Thus, the difference in the dispersion spaces between steady-state and transient model may even be multiplied in the riparian zone. It can cause also significant differences in the calculated concentrations, because of the more intensive dispersion and dilution approaching the river. At the same time, for low-river stage periods of transient simulation (crossed line), the dispersion values are almost the same as for steady-state model, while a smaller difference here is detected near the river.

We can conclude that in transient simulations not only the flow velocities but also the dispersion are continuously changing between two limits, which are related to the highest and lowest river stages of the total simulation time.

3.3. Results of contaminant plume movement

To prove our assumptions related to the impacts of flow paths, flow velocities, and dispersion on plume movement, point contaminant sources were identified in the model domain at two different distances from the river. Advective and dispersive transport were assumed, and the plume evolution was recorded in the steady-state and transient flow field.

The direction of plume spreading is roughly the same (SE) in the steady-state and transient cases, but the plume moves much faster toward the river in the transient method *(Figure 7)*. For the slightly more distant source from the river, the differences in the spreading directions are also dominant *(*see *Figure 8)*. The differences in spreading velocity, direction and plume extent increase with time and proximity to the river.

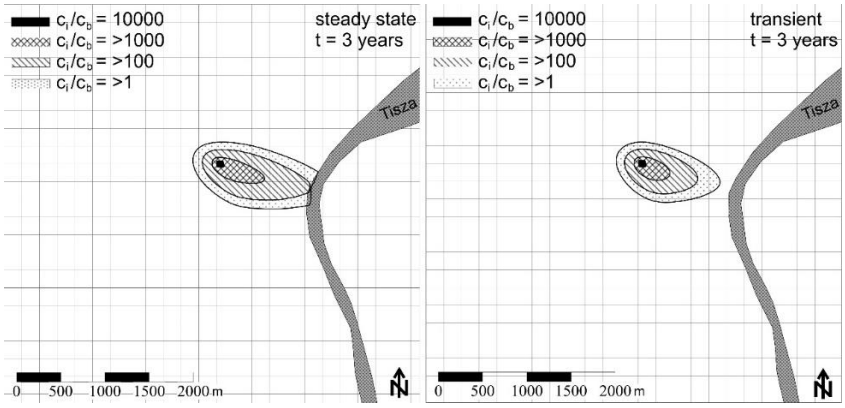

Figure 7
Calculated dissolved concentration distributions in simulation times of 3 years (source 1)

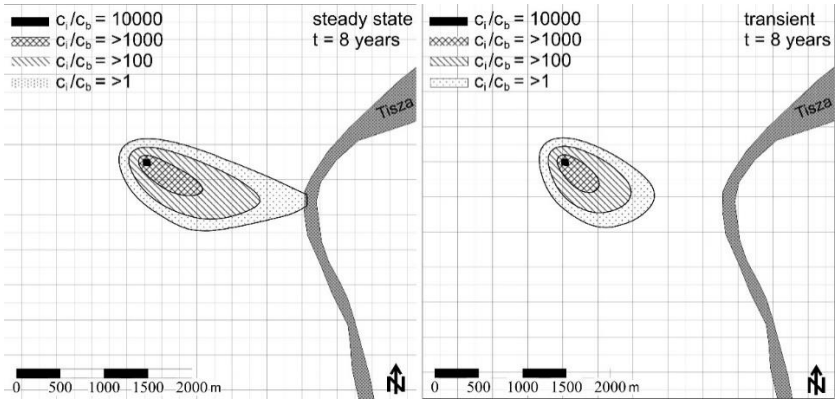

Figure 8
Calculated dissolved concentration distributions in simulation times of 8 years (source 2)

In the steady-state simulations we assume groundwater flow with constant direction and gradient toward the river, but in reality these parameters change with time. Although the assumed flow field reflects the average flow situation, which is confirmed by a high precision calibration of the model, we still do not get the same spreading characteristics as in the transient case. These differences can also be detected in the concentration time series of monitoring points (m1, m2 in *Figure 2*). In the average flow direction the steady-state concentrations increase more rapidly (*Figure 9*, point m1). At the same time in south direction the transient simulation shows higher concentrations (*Figure 9*, m2 point), which is caused by the much wider spreading of the transient plume.

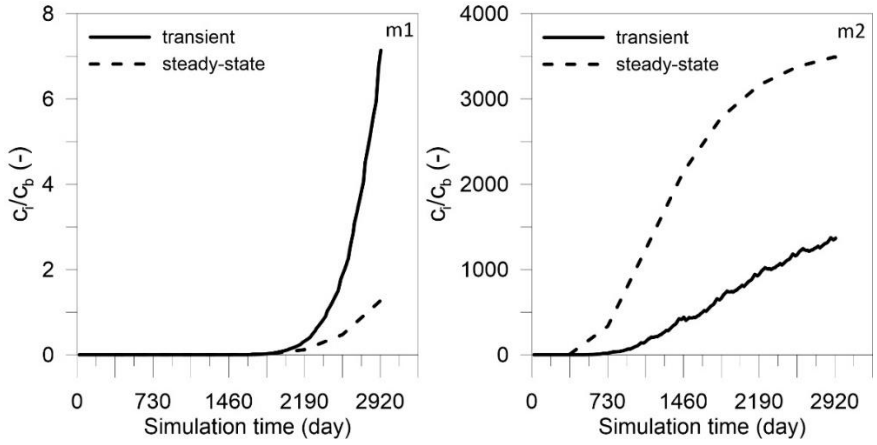

Figure 9

Calculated concentration time series at observation points

4. CONCLUSIONS

There can be significant differences in the simulated dissolved plume movement when assuming either steady-state or transient groundwater flow field of the studied river-influenced aquifer. The basic reason is the different flow velocity fields for the two kinds of simulation. The direction and length of flow velocity vectors are constant in the steady-state simulation, while these are changing throughout the time periods in the transient case. This causes continuous forward-backward steps of the particles and longer flow paths. The dispersion also changes in time between the two limiting conditions of the river stages. Steady-state simulation can underestimate the dispersion approaching the river, because it cannot handle the losing river's conditions, when the flow velocities and the calculated dispersions can be multiplied.

Advective transport with variable flow directions and the changing dispersion in space and time can result in the phenomenon of plume dynamics in the river-influenced aquifer. Plume dynamics can cause slower plume movement toward the river and fluctuating concentrations in monitoring points around the plume.

Based on the results, it can be concluded that transport simulations built on the steady-state flow model have limitations to accurately describing certain transport phenomena, even in case of accurately calibrated flow model. In the presented case, when a river with highly fluctuating water level is connected to a shallow aquifer, a transport simulation based on the transient flow field can be more reliable for future forecasts related to dissolved plume movement.

ACKNOWLEDGEMENTS

The described study (transport simulations) was carried out as part of the EFOP-3.6.1-16-2016-00011 *Younger and Renewing University – Innovative Knowledge City – institutional development of the University of Miskolc aiming at intelligent specialisation* project implemented in the framework of the Szechenyi 2020 program. The realization of this project is supported by the European Union, co-financed by the European Social Fund.

The background research (gw flow computations) was carried out within the GINOP-2.3.2-15-2016-00031 *Innovative solutions for sustainable groundwater resource management* project of the Faculty of Earth Science and Engineering of the University of Miskolc in the framework of the Széchenyi 2020 Plan, funded by the European Union, co-financed by the European Structural and Investment Funds.

REFERENCES

[1] Winter, T. C., Harvey, J. W., Franke, O. L., Alley, W. M. (1998): *Ground water and surface water, a single resource*. US Geological Survey Circular, 1139., p. 79., ISBN 0–607–89339–7.

[2] Chen, X., Chen, X. (2003): Stream water infiltration, bank storage, and storage zone changes due to stream-stage fluctuations. *Journal of Hydrology*, 280, pp. 246–264.

[3] Singh, K.P. (1968): Some factors affecting baseflow. *Water Resources Research*, 4, No. 5, pp. 985–999.

[4] Rózsa A. (2000): Beszivárgási vizsgálatok a Szentendrei-Duna medrében. *Hidrológiai Közlöny*, 2000. évf., 2. szám, pp. 119–131.

[5] Léczfalvy, S. (2004): *Felszín alatti vizeink 1–2*. ELTE Eötvös Kiadó, Budapest.

[6] Deák J., Hertelendi E., Süveges M., Barkóczi Zs. (1992): Partiszűrésű kutak vizének eredete trícium koncentrációjuk és oxigén izotóparányaik felhasználásával. *Hidrológiai Közlöny*, 72. évf., 4. szám, pp. 204–210.

[7] Kármán, K., Maloszewski, P., Deák, J., Fórizs, I., Szabó, Cs. (2013): Transit Time Determination in Riverbank Filtrated System by Oxygen Isotopic Data

Using the Lumped Parameter Model. *Hydrological Sciences Journal*, 59 (6), pp. 1109–1116.

[8] Völgyesi I. (2005): Mennyit termelhetünk a felszín alatti vízkészletekből? *Hidrológiai Közlöny*, 5. szám, pp. 20–24.

[9] Palcsu, L., Kompár, L., Deák, J., Szűcs, P., Papp, L. (2017): Estimation of the natural groundwater recharge using tritium-peak and tritium/helium-3 dating techniques in Hungary. *Geochemical Journal*, 51, pp. 439–448.

[10] Szabó, N. P., Dobróka, M., Turai, E., Szűcs, P. (2014): Factor analysis of borehole logs for evaluating formation shaliness: a hydrogeophysical application for groundwater studies. *Hydrogeology Journal*, 22 (3), pp. 511–526.

[11] Csoma R., Emszt Gy., Gálos M. (2012): *A Duna árhullámainak hatása a talajvízszint-változásra egy folyóra merőleges szelvényben*. Mérnökgeológia – Kőzetmechanika Kiskönyvtár 7, Műegyetemi Kiadó, Budapest.

[12] Derx, J., Blaschke, A. P., Blöschl, G. (2010): Three dimensional flow patterns at the river-aquifer interface – a case study at the Danube. *Advances in Water Resources*, 33, pp. 13., doi:10.1016/j.advwatres.2010.04.013.

[13] Huber, E., Huggenberger, P., Epting, J., Schindler, W. Y. (2013): Zeitliche und räumliche Skalen der Fluss-Grundwasser-Interaktion: Ein multidimensionaler hydrogeologischer Untersuchungsansatz. *Grundwasser, Zeitschrift der Fachsektion Hydrogeologie*, Springer-Verlag Berlin Heidelberg.

[14] Schmidt, C., Musolff, A., Trauth, N., Vieweg, M., Fleckenstein, J. H. (2012): Transient analysis of fluctuations of electrical conductivity as tracer in the stream bed. *Hydrology and Earth System Sciences*, 16, pp. 3689–3697.

[15] Schornberg, C., Schmidt, C., Kalbus, E., Fleckenstein, J. H. (2010): Simulating the effects of geologic heterogeneity and transient boundary conditions on streambed temperatures—implications for temperature-based waterflux calculations. *Advances in Water Resources*, 33, pp. 1309–1319.

[16] K. Tóth, A., Kovács, B. (2015): Calibration process for groundwater flow model of a river influenced shallow aquifer. *Central European Geology*, Vol. 58/1–2., pp. 186–198.

[17] Chiang, W-Hs. (2010): *Processing MODFLOW, An Integrated Modeling Environment for the Simulation of Groundwater Flow, Transport and Reactive Processes*. Users manual, Simcore Software.

[18] Harbaugh, A. W., Banta, E. R., Hill, M. C., McDonald, M. G. (2000): *MODFLOW-2000, the U.S. Geological Survey modular ground-water model – User guide to modularization concepts and the ground-water flow process*. U.S. Geological Survey Open-File Report 00-92.

[19] Pollock, D. W. (2012): *User guide for MODPATH Version 6 – a particle tracking model for MODFLOW*. U.S. Geological Survey Techniques and Methods 6-A41.

[20] Fetter, C. W. (1999): *Contaminant Hydrogeology*. Upper Saddle River, NJ: Prentice-Hall.

[21] Freeze, R. A., Cherry, J. A. (1979): *Groundwater*. Englewood Cliffs, NJ: Prentice-Hall.

Geosciences and Engineering, Vol. 7, No. 10 (2019), pp. 158–168.

BEHAVIOUR OF REGULAR-SHAPE SINGLE PARTICLES WHILE FALLING IN NORMAL AIR CONDITIONS

ROLAND RÓBERT ROMENDA[1] – ZSÓFIA BURINDA[2]

[1]PhD student, [2]BSc student
Institute of Raw Materials Preparation
and Environmental Processing, University of Miskolc,
Hungary, 3515 Miskolc-Egyetemváros, ejtrom@uni-miskolc.hu

Abstract: The first Hungarian plant for residual municipal solid waste preparation has been installed in Zalaegerszeg. The plant is equipped almost wholly with domestically produced machinery, including a new KLME (Combined Airflow, Magnetic and Electric) separator. For the development of the KLME separator fundamental particle motion testing was carried out. During the experiments, the movement of regular-shape polystyrene and PVC particles was tested and their terminal settling velocities and relaxation times were measured. The particles were dropped from the height of 16 meters, which allowed the particles to reach stationary particle settling. The falling particles were recorded by a video camera and the terminal settling velocity and relaxation time were determined by image analysis of serial frames. The effects of particle size, shape, density and orientation on settling were examined.

Keywords: *residual fraction of municipal solid waste (RMSW), airflow separator, terminal settling velocity, relaxation time*

1. INTRODUCTION

3B Hungária Ltd. in Zalaegerszeg and the Institute of Raw Materials Preparation and Environmental Processing, University of Miskolc, as a scientific partner are co-working on the construction of a new plant that will process the residual fraction of municipal solid waste of the region. The most important result of the consortium cooperation is the newly developed equipment, the KLME separator (the name KLME is the Hungarian abbreviation of combined air flow, magnetic and electric). The machine consists of four units, two different air flow separators, one magnet drum and one eddy current separator. The advantage of the combined machine is that there are no conveyor belts between each unit, which saves space and electricity compared to four single separators. The operation of air flow separators are primarily determined by the motion of waste particles in air, therefore, it is important to examine how the size, shape and density of particles affect particle settling.

Laminar flow, also called layered flow, is when the molecules of the medium pass along side by side without cross directional mixing; therefore, streamlines are also pathways of molecules. However, if the fluid is in turbulent flow, the degree of turbulence also affects the viscous resistance on objects. In turbulent flow *(Figure 1)* there is no molecular stratification, but the paths of adjacent molecules influence

each other due to the fluctuations in the direction and magnitude of their velocity, and the flow is mixed [8].

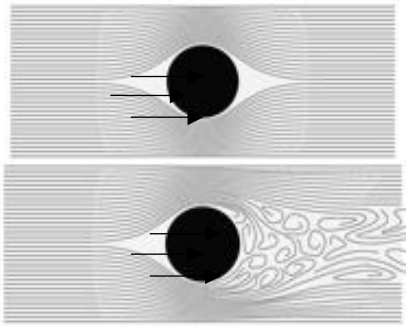

Figure 1
The nature of laminar and turbulent flow around a sphere

The particle Reynolds number is a dimensionless quantity that is the ratio between the inertia force and the viscous friction force, i.e. the internal friction of the medium:

$$Re_x = \frac{x \cdot \rho_k \cdot v_o}{\mu} \tag{1}$$

where: Re_x – Reynolds number
x – particle size
ρ_k – density of the fluid
v_0 – velocity of the particle in the fluid
μ – dynamic viscosity of the fluid.

Depending on the size of the particle and the characteristics of the medium, different flows (laminar or turbulent) may form around the particle, and on the other hand, in the case of ultra-fine particle sizes, the medium can no longer be considered as a continuum; therefore, it is necessary to distinguish settling regimes. The particle size of about 0.1 μm is treated as the limit. In cases of finer particles the motion of an ultra-fine particle is affected by collision with fluid molecules (Brownian motion), whereas the motion of a bigger particle does not depend on a single collision with a molecule but the fluid can drag the bigger particle. Therefore, the particle size of 0.1 μm is the boundary between the colloid and disperse systems [5, 6].

At low Reynolds numbers (<0.1), the behaviour of Newtonian liquids depends primarily on the absolute viscosity and the flow around the particle is stable laminar (Stokes settling regime). In the case of greater Reynolds numbers (0.1–1,000), there is still laminar sub-layer around the particle, but further the flow is transitional laminar–turbulent (the transitional settling regime); clearly turbulent flow forms around the particle at higher Reynolds numbers (1,000–$2 \cdot 10^5$, Newton settling regime), and the laminar sub-layer breaks for really high Reynolds numbers (>$2 \cdot 10^5$, full turbulent settling regime) [4]. The basis of separation in air flow separators is the different settling of the

particles in the medium. Airflow devices can be designed both for the start of the particle settling (relaxation time) and the steady-state (terminal settling velocity) periods. The resulting particle movement depends on the particle size and shape and the air and particle densities. Separation occurs in air flow equipment when the medium moves ahead or at an angle compared to the particle settling. Accordingly, we are talking about counter-flow and cross-flow air flow separators. Depending on the terminal settling velocity of a given particle, separation in a counter-flow apparatus is determined by the terminal settling velocity versus the upward air velocity. If the terminal settling velocity is lower than the upward air velocity, then this particle will be dragged by the media into the light product; particles with higher terminal settling velocity than the fluid stream velocity will settle into the heavy product.

The separation of particles of the same size and shape in the fluid stream is carried out according to the density of the particles, because the density determines the terminal settling velocity of the particles in this case. In a gravity air flow separator the drive of a particle settling is the force of gravity minus the buoyancy force. In a centrifugal air flow separator the drive of a particle settling is the centrifugal force minus the buoyancy force. When the particle starts to settle and there is a relative velocity difference between the fluid and the particle, the drag force arises because of surface viscous friction and surface pressure distribution. When the resultant force becomes zero, because the drag force fully competes with the drive force, the particle moves in a straight line, constant velocity movement, namely it does not change its motional state according to the second law of Newton. The velocity at this special settling state is called "terminal settling velocity". The vertical (gravity) and radial (centrifugal) terminal settling velocities of particles depend on the particle size (d), the ratio between the particle (ρ_p) and medium (ρ_m) densities, and the drag coefficient (C_D). C_D depends on the particle shape and the acceleration of the medium [1, 2, 3].

The KLME separator in the waste processing plant currently under construction will process waste particles of sizes from 70 to 200 mm. These particles typically settle in the Newton settling regime, namely their particle Reynolds number in air is typically in the 1,000–$2 \cdot 10^5$ range. In air flow separators the air is generally not quiescent, therefore two more forces have to be taken into account: the settling of a particle is affected by the gravity (G), the buoyancy force (F_B), the drag force (F_D), the inertia force (F_I) of the displaced air mass and the inertia force (F_T) of the particle mass. The change in the motion state of the particle is the consequence of these forces. The literature provides a theoretical solution for the Stokes and the Newton turbulent settling regimes [9, 7]. In the Newton turbulent settling regime the velocity-settling time function is a tangent hyperbolic function *(Equation 2)*:

$$v(t) = v_o \cdot \mathrm{th}\left(\frac{t}{t_R}\right) \tag{2}$$

where: $v(t)$ – actual velocity of the particle
v_0 – terminal settling velocity of the particle
t – time
t_R – relaxation time.

There are two parameters in the derived motion function. The tangent hyperbolic function theoretically reaches the steady speed, the terminal settling velocity (v_0), only after infinite time. In engineering practice, we are talking about steady-state particle movement at the time of reaching 99% of the speed. The physical meaning of the relaxation time (t_R) parameter is the time until the settling particle reaches 76% of the settling speed, therefore t_R characterises the unsteady-state particle settling section. The shape factor (SF) of a settling non-spherical particle can be determined by the theoretical terminal settling velocity (v_{0x}) calculated for the equivalent-volume sphere (x).

$$x = \sqrt[3]{\frac{6 \cdot V}{\pi}} \qquad SF = \frac{v_o}{v_{ox}} \tag{3a, 3b}$$

where: x – volume-equivalent diameter
V – volume of sample
SF – shape factor
v_0 – measured terminal settling velocity
v_{0x} – calculated terminal settling velocity of volume-equivalent sphere.

2. MATERIALS AND METHODS

To carry out the described tests, 35 regular model particles f different types and dimensions were prepared, made from PVC tubes and sheets. Because these model particles were regular shaped, their geometric dimensions could be measured with a calliper, therefore their surface and volume were calculated. Their weights were measured by a four-decimal-points scale. Photographs of the 35 particles are shown in *Figure 2*.

The aim of the drop tests was to measure the settling velocity – time (height) function of the waste particles in the air. We created a video record of the falling bodies using a hand held camera, which was cut into frames by digital image processing to determine the path-time graph of the frame number and pixel position (pixel coordinates). The video was shot with a Canon SX150 IS camera, the video was cut with the free shareware version of Video to Picture 5, which was later processed with the PhotoFiltre 6 image editing software. We used central open space of a 5-storey building at the University of Miskolc because it is sufficiently high and only minimal air movement is present in its interior. During the experiments, the model particles were dropped from the top floor at a well-defined point of 15.8 meters height. The distortion of the camera lens and the perspective effect were calibrated by using a 20 m tape as reference, and we also analysed the vertical motion. During the measurements, we observed how the different particles behaved in the acceleration phase when they were released in different starting orientations. At launch, we released the particles each time in the same way, so that they would not gain a starting torque to eliminate the Magnus effect.

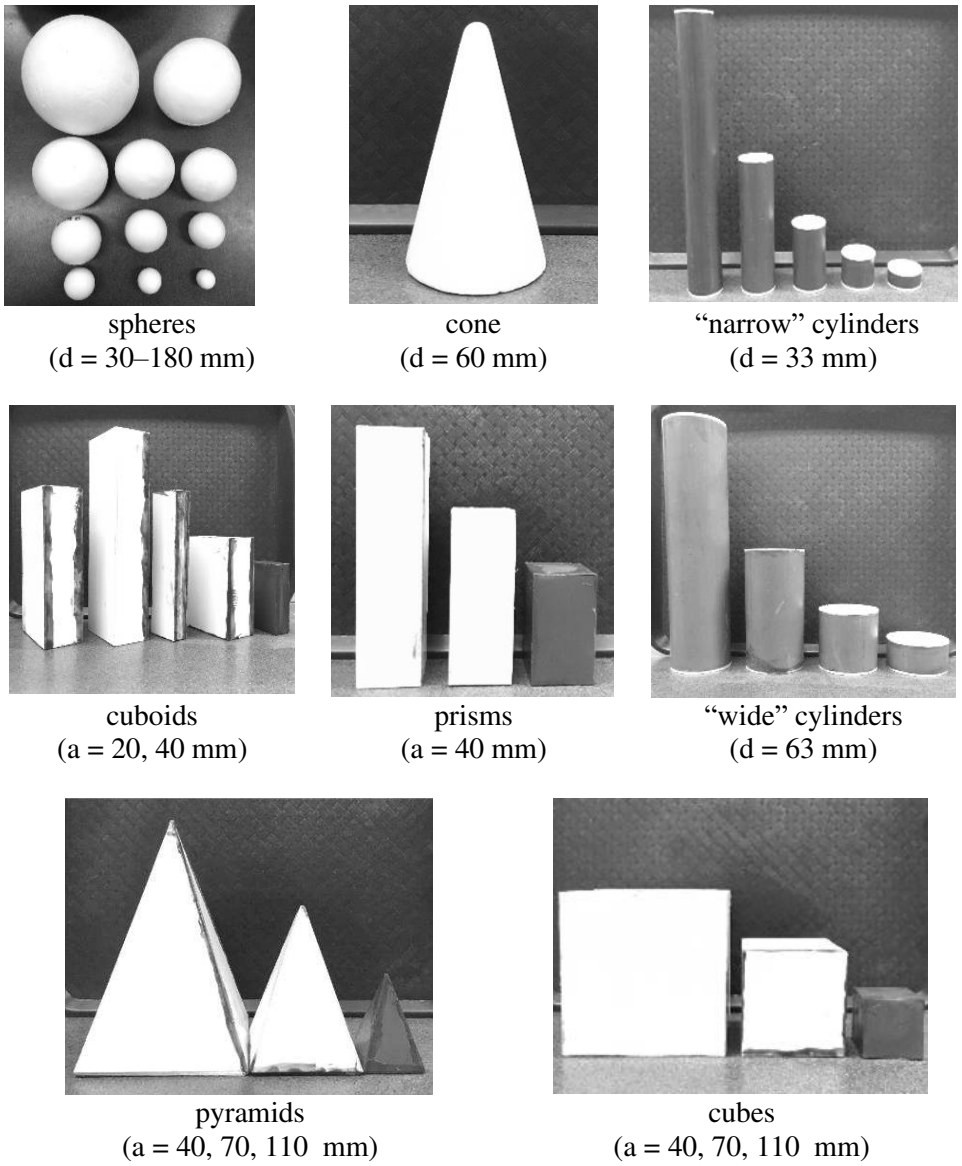

Figure 2
The model particles

After dropping the particles, statistical measurements were performed with 5 different spheres (40, 60, 80, 120 and 180 mm diameter), which were dropped 7 times each. The aim of the measurement was to verify the accuracy of the measurement method by determining the sample mean, the corrected empirical standard deviation and the margin of error.

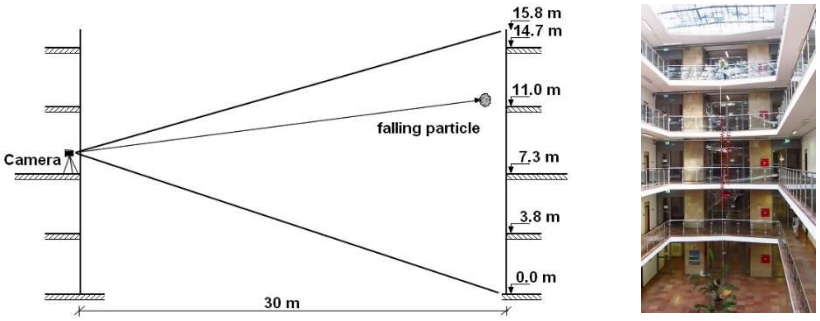

Figure 3

The geometric arrangement of the capture and the view of the camera

3. RESULTS

3.1. Results of particle settling experiments

After the measurements, the video recordings were split into frames, and the coordinates of the geometric centre of the sample on the images were written with pixel coordinates. With the help of these coordinates, we were able to determine the location of the sample particle at that time, from which we could calculate its instantaneous velocity. The resulting values are depicted in graphs and *Equation 2* was curve fitted to the measured time-settling velocity points. Using the best fit curves, the terminal settling velocity and the relaxation time parameters were determined. Since the tested particles were regular shaped, the diameters of the volume equivalent spheres and their theoretical terminal settling velocities could be calculated; hence, the particle shape factors could be also determined. Results of the evaluation are shown in *Table 1*.

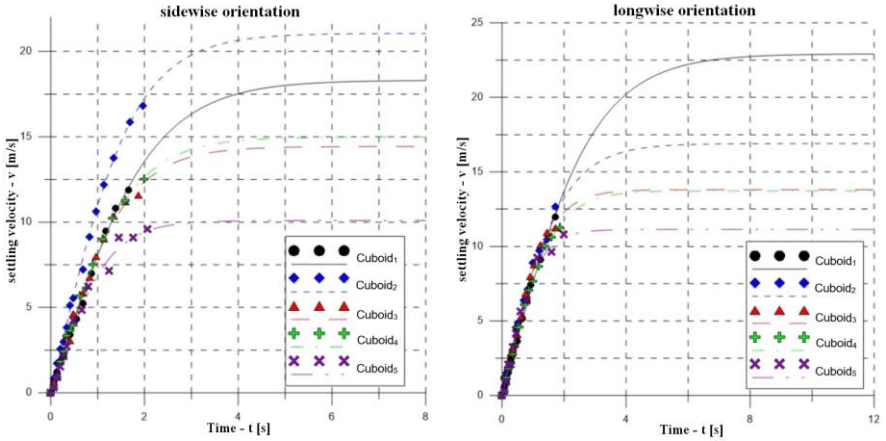

Figure 4

Velocity-time diagrams of the cuboid samples in different orientations

Table 1

The measured and calculated parameters of some samples

#	Sample	Orientation a – sidewise b - longwise	Eq. vol. sphere diameter [mm]	Calc. terminal settling velocity [m/s]	Meas. terminal settling velocity [m/s]	t_R [s]	R^2 [-]	Shape factor [-]	Reynolds number [-]
101	$Sphere_{30}$	–	30.0	6.10	6.09	0.76	0.9922	1.00	11,658
102	$Sphere_{40}$	–	40.0	6.79	6.65	0.72	0.9742	0.98	16,960
103	$Sphere_{50}$	–	50.0	7.29	7.33	0.76	0.8521	1.01	23,373
104	$Sphere_{60}$	–	60.0	6.46	6.62	0.73	0.9622	1.02	25,310
106	$Sphere_{80}$	–	80.0	7.09	6.53	0.73	0.8124	0.92	33,326
107	$Sphere_{90}$	–	90.0	7.80	7.79	0.96	0.9968	1.00	44,712
108	$Sphere_{100}$	–	100.0	7.90	7.36	0.83	0.9722	0.93	46,905
109	$Sphere_{120}$	–	120.0	8.92	8.73	1.06	0.9967	0.98	66,809
110	$Sphere_{140}$	–	140.0	7.91	7.93	1.04	0.9966	1.00	70,748
111	$Sphere_{180}$	–	180.0	8.44	8.33	1.01	0.9932	0.99	95,642
112	$Cone_1$	a	65.9	9.96	6.49	0.78	0.9954	0.65	49,361
112	$Cone_2$	b	65.9	9.96	6.33	0.71	0.9795	0.64	48,109
113	$Pyramid_1$	–	110.1	24.95	13.72	1.63	0.9983	0.55	144,312
114	$Pyramid_2$	–	71.8	24.56	13.10	1.47	0.9983	0.53	90,009
115	$Pyramid_3$	–	40.4	18.22	10.13	1.25	0.9924	0.56	39,568
116	$Cube_1$	–	136.7	23.31	16.56	1.92	0.9965	0.71	116,156
117	$Cube_2$	–	88.7	23.19	16.34	1.88	0.9951	0.70	74,349
118	$Cube_3$	–	50.3	16.82	11.08	1.26	0.9887	0.66	28,795
119	$Prism_1$	–	79.1	25.28	13.24	1.51	0.9983	0.52	34,192
120	$Prism_2$	–	70.2	23.88	13.91	1.60	0.9980	0.58	36,046
121	$Prism_3$	–	60.0	16.89	10.61	1.17	0.9790	0.63	27,369
122	$Cuboid_1$	a	99.4	25.18	18.31	2.09	0.9972	0.73	93,385
123	$Cuboid_2$	a	106.2	25.87	21.05	1.73	0.9982	0.81	93,953
124	$Cuboid_3$	a	62.7	26.89	14.43	1.55	0.9954	0.54	37,118
125	$Cuboid_4$	a	84.6	24.31	14.98	1.61	0.9962	0.62	67,959
126	$Cuboid_5$	a	49.7	18.48	10.09	1.18	0.9902	0.55	25,828
122	$Cuboid_1$	b	99.4	25.18	22.92	2.89	0.9951	0.91	116,930
123	$Cuboid_2$	b	106.2	25.87	16.90	1.93	0.9919	0.65	75,414
124	$Cuboid_3$	b	62.7	26.89	13.81	1.40	0.9939	0.51	35,522
125	$Cuboid_4$	b	84.6	24.31	13.73	1.55	0.9971	0.56	62,296
126	$Cuboid_5$	b	49.7	18.48	11.14	1.08	0.9899	0.60	28,517
127	N. $cylinder_1$	a	75.7	28.41	13.93	1.49	0.9848	0.49	29,301
128	N. $cylinder_2$	a	60.0	25.78	15.95	1.74	0.9870	0.62	33,549
129	N. $cylinder_3$	a	47.6	23.89	22.11	2.77	0.9885	0.93	46,526
130	N. $cylinder_4$	a	37.9	22.69	16.75	1.86	0.9916	0.74	35,241
131	N. $cylinder_5$	a	30.4	23.19	16.57	1.71	0.9858	0.71	34,870

127	N. cylinder$_1$	b	75.7	28.41	19.08	2.07	0.9736	0.67	40,153
128	N. cylinder$_2$	b	60.0	25.78	15.48	1.48	0.9869	0.60	32,576
129	N. cylinder$_3$	b	47.6	23.89	15.91	1.72	0.9924	0.67	33,480
130	N. cylinder$_4$	b	37.9	22.69	16.29	1.84	0.9917	0.72	34,269
131	N. cylinder$_5$	b	30.4	23.19	12.64	1.31	0.9840	0.54	26,587
132	W. cylinder$_1$	a	114.5	26.03	16.84	1.98	0.9959	0.65	67,650
133	W. cylinder$_2$	a	90.9	24.04	17.63	1.97	0.9947	0.73	70,829
134	W. cylinder$_3$	a	72.3	23.15	16.24	1.78	0.9923	0.70	65,244
135	W. cylinder$_4$	a	57.6	23.42	16.31	1.86	0.9957	0.70	65,502
132	W. cylinder$_1$	b	114.5	26.03	15.88	1.64	0.9885	0.61	63,777
133	W. cylinder$_2$	b	90.9	24.04	20.33	2.16	0.9951	0.85	81,660
134	W. cylinder$_3$	b	72.3	23.15	15.97	1.73	0.9937	0.69	64,138
135	W. cylinder$_4$	b	57.6	23.42	12.28	1.34	0.9900	0.52	49,323

3.2. Results of statistical measurement

The true value of the measured parameters was estimated by the sample mean and the deviation was estimated by the corrected empirical standard deviation.

$$\bar{v}_o = \frac{\sum_{i=1}^{n} v_{oi}}{n} \qquad S_n^* = \sqrt{\frac{\sum_{i=1}^{n}(v_{oi}-\bar{v}_o)^2}{n-1}} \tag{4a, 4b}$$

where: $\bar{v}_o$ – mean of the measured velocities
v_{oi} – measured velocities
n – number of measurements
S_n^* – corrected empirical standard deviation.

At a 95% confidence level, a confidence interval was estimated by the Student distribution around the true value. The margin of error was calculated using *Equation 5*. The true value is expected to be in the sample mean ± HM interval with 95% confidence.

$$HM = t_{\frac{\varepsilon}{2}} \cdot \frac{S_n^*}{\sqrt{n}} \tag{5}$$

Table 2
Results of statistical calculations

Sample	$\overline{v_o}\left[\frac{m}{s}\right]$	$S_n{}^*\left[\frac{m}{s}\right]$	$HM_v\left[\frac{m}{s}\right]$	HM_v [%]	$\overline{t_R}$[s]	$S_n{}^*$[s]	HM_t [s]	HM_t [%]
Sphere$_{40}$	6.680	0.136	0.100	1.49	0.740	0.058	0.043	5.81
Sphere$_{60}$	6.461	0.163	0.119	1.84	0.717	0.051	0.038	5.29
Sphere$_{80}$	6.910	0.080	0.080	1.15	0.784	0.047	0.035	4.46
Sphere$_{120}$	8.597	0.236	0.174	2.02	0.990	0.061	0.045	4.54
Sphere$_{180}$	8.219	0.262	0.192	2.33	1.019	0.064	0.047	4.61

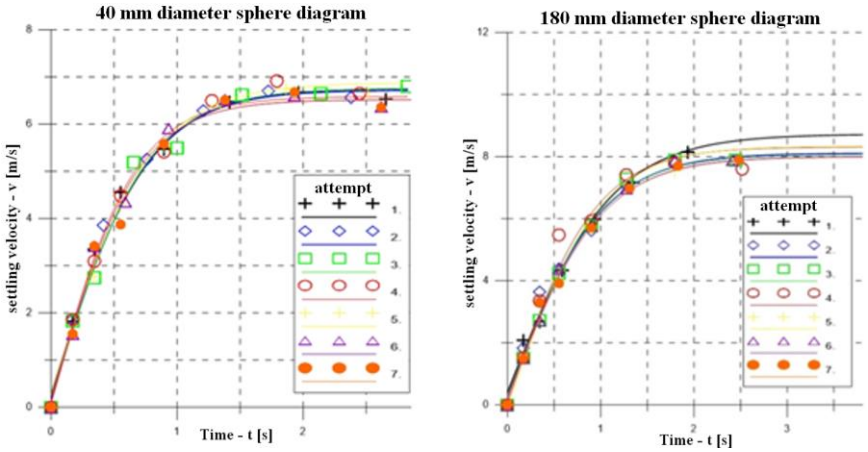

Figure 5

Settling velocity- as a function of time for the 40 and 180 mm spheres

4. CONCLUSIONS

It can be stated that all of the examined particles finally settled in the Newton turbulent settling regime (1,000–$2 \cdot 10^5$ particle Reynolds number range), where the particle shape plays a key role in settling behaviour. The shape of real municipal solid waste particles of this size range (60–200 mm) is fairly diverse; therefore this factor is very important for waste separator developments. The shape of a particle determines the initial (starting) and final settling of the particle and these two parameters are the basis of separation for many different air flow separators. This paper contains measured shape factors for some typical regular shaped particles, and these results can be used for separator designs. However, some more theoretical considerations are still necessary to reveal methods to determine shape factors of different particles on the basis of their known geometrical sizes.

Table 3

Results of the measured shape factor

Type of the body	Measured shape factor
sphere	1
cone	0.64
pyramid	0.54
cube	0.7
prism	0.52–0.63
cuboid	0.51–0.81
cylinder	0.49–0.93

Statistical measurements have demonstrated that the developed measurement method has less than a 2% margin of error at the 95% confidence level. During the

measurements we found that some samples turned in to their largest extent. From this it can be concluded that if a waste particle has a sufficient height to approach its final position, it will orient itself according to its largest projection surface. For cuboids, the largest projection surface is the following if a, b, and c indicate the side length in ascending order.

$$A_{vmax} = \sqrt{a^2 + c^2} \cdot b \tag{6}$$

where: A_{vmax} – largest projection surface
a, b, c – side length in ascending order

ACKNOWLEDGEMENT

The described work was carried out as part of the EFOP-3.6.1-16-2016-00011 *Younger and Renewing University – Innovative Knowledge City – institutional development of the University of Miskolc aiming at intelligent specialisation* project implemented in the framework of the Széchenyi 2020 program. The realization of this project is supported by the European Union, co-financed by the European Social Fund.

REFERENCES

[1] Faitli, J. (2000): Pressure loss calculation model for well-graded solid-liquid pipe flows on the basis of systematic pilot plant investigations. In: Shammazov Airat, M., Besenyei, L. (eds.): *Intellectual Services for Oil and Gas Industry Proceedings: Analysis, Solution and Perspectives*. Vol. 1. Miskolc, University of Miskolc, pp. 212–221.

[2] Faitli J. (2011): Szemcsés anyagok – csővezetékben – folyadékárammal való szállításának méretezése. 1 rész: Kísérleti berendezések és modell. *Építőanyag*, 63. évfolyam, 1. szám, pp. 10–15.

[3] Faitli J. (2012): Szemcsés anyagok – csővezetékben – folyadékárammal való szállításának méretezése. 2. rész: A nyomásveszteség számítása. *Építőanyag*, 64. évfolyam, 1–2. szám, pp. 2–7.

[4] Faitli J. (2015): Szemcsemozgás mérése és számítása nem-newtoni egy- és többfázisú közegekben. *Bányászati és Kohászati Lapok – Bányászat*, 3, pp. 2–9.

[5] Faitli J. (2017): Kontinuitási elmélet diszperz anyagrendszerek különféle berendezésekben való eltérő viselkedésének a jellemzésére. *Műszaki Földtudományi Közlemények*, 86 (1), pp. 11–22.

[6] Faitli, J. (2017): Continuity theory and settling model for spheres falling in non-Newtonian one- and two-phase media. *International Journal of Mineral Processing*, 169 (1), pp. 16–26.

[7] Mann, H. et al. (2015): Analytical description of the unsteady settling of spherical particles in Stokes and Newton regimes. *Granular Matter*, 17 (5), pp. 629–644.

[8] Pokorádi L. (2002): *Áramlástan*. Elektronikus jegyzet, Debrecen, pp. 45–48.

[9] Tarján I. (1997): *A mechanikai eljárástechnika alapjai: Részecskék és folyadék relatív mozgása*. Miskolci Egyetemi Kiadó, Miskolc.